

HF-MIMO Antenna Array Design and Optimization

Thesis submitted for the degree of

Doctor of Philosophy

at the University of Leicester

by

Jiatong Liu

Department of Engineering

University of Leicester

October 2015

HF-MIMO Antenna Array Design and Optimization

Jiatong Liu

Abstract

MIMO as a new antenna array communication technology has been widely applied in modern communications, especially within UHF/VHF band. After several experimental campaigns, E.M. Warrington and S.D. Gunashekar proved that MIMO techniques could also be applicable within HF band. Further experiments showed that traditional widely spaced homogeneous antenna arrays could be replaced by co-located heterogeneous antenna arrays without significant reductions in data transmission rate. In other words, radiation pattern diversity can be used as a new kind of MIMO diversity to replace spatial diversity.

In order to get a better understanding of this phenomenon, antenna modelling using numerical electromagnetics code (NEC) has been carried out in last three years. The study showed that phase difference difference (PDD) between collocated antenna array elements could be the key factor of radiation pattern diversity. The correlation level between array elements can be reduced with increased PDD between these elements. Several transmitting antenna arrays have been developed according to this study and tested via a 202 km radio link between Leicester and Lancaster. The experimental campaigns showed that the newly designed antenna arrays have a significantly increased de-correlation level between array elements compared with traditional antenna arrays. High performance computing (HPC) was used in the antenna modelling in order to investigate the relationship between antenna array geometry and phase difference difference. Several optimized antenna arrays with large phase difference difference were recommended from tens of million of different antenna geometries.

This research gives the new direction of HF-MIMO antenna array design: in theory aspect, it clearly specifies what kind of pattern needs to be targeted in order to get decorrelation using pattern diversity; in antenna modelling aspect, HPC was for the first time applied in HF-MIMO antenna array design, which provided a brand new high level of computing platform for the future modelling work.

Acknowledgement

I would like to thank my supervisors Prof. Mike Warrington and Dr. David Siddle. Without their guidance and helpfulness, my research work would not have been completed due to my youthful impatience and inexperience. I also would like to appreciate the valuable NEC modelling suggestions from Neoklis Kyriazis, Tim Molteno and Kok Chen. This research used the ALICE High Performance Computing Facility at the University of Leicester.

Table of content

Abstract.....	i
Acknowledgement	ii
Chapter 1 Introduction	1
Chapter 2 HF propagation environment	6
2.1 The ionosphere.....	6
2.2 HF propagation fundamentals	8
2.2.1 Ionogram.....	11
2.2.2 The Secant Law and Transmission Curve	12
Chapter 3 HF-MIMO background	16
3.1 Fundamental concepts of MIMO	16
3.2 MIMO channel capacity calculation	20
3.3 MIMO in HF band	22
3.4 Development of HF antenna arrays.....	24
Chapter 4 Numerical electromagnetics code (NEC) modelling	30
4.1 Numerical Electromagnetics Code.....	30
4.1.1 Modelling working region.....	31
4.1.2 Modelling guidelines.....	32
4.1.3 Modelling software CocoaNEC and NEC2C.....	34
4.2 Modelling Methodology	38
4.2.1 The Bivectorial Model.....	38
4.2.2 Radiation pattern diversity effect on correlation coefficients based on 2×2 MIMO simulation	41
4.2.3 Phase difference difference (PDD) diversity	46
4.2.4 Opposite expression in polarization.....	49
Chapter 5 Experimental set up	50
5.1 Transmitting System	50
5.2 Receiving System.....	52
5.2.1 Receiving antenna.....	52
5.2.2 Perseus software defined radio (SDR) receiving system.....	54
5.3 Experimental arrangement	55

Chapter 6 Summary and modelling of previous experiments.....	56
6.1 Experiment 1: Crossed End-Fed Vee array performance at the transmitter	56
6.1.1 Experimental Arrangement	56
6.1.2 Results and Discussion.....	58
6.2 Experiment 2: Crossed end-fed Vee array performance at the receiver	63
6.2.1 Experimental Arrangement	63
6.2.2 Results and Discussion.....	64
6.3 Traditional collocated end-fed Vee antenna array modelling and analysis	66
Chapter 7 Modelling of novel antenna arrays and measurements	72
7.1 Novel antenna arrays modelling.....	73
7.1.1 Antenna Array T1 Modelling.....	73
7.1.2 Antenna Array T2 Modelling.....	76
7.1.3 Antenna array Ex-ORG and Ex-T2 Modelling	79
7.1.4 Antenna Array E2 Modelling.....	85
7.1.5 Antenna Array S2 Modelling.....	88
7.1.6 Non-Planar twisted (NPT) transmitting antenna array modelling	90
7.2 Measurements for modelled novel antenna arrays	92
7.2.1 Comparison of T1 and ORG array in 4×1 MISO measurement.....	93
7.2.1.1 Experimental Arrangement.....	93
7.2.1.2 Results and Discussion.....	94
7.2.2 Comparison of T2 and ORG array in 4×1 MISO measurement.....	100
7.2.2.1 Experimental Arrangement.....	100
7.2.2.2 Results and Discussion.....	100
7.2.3 Comparison of T2 and ExT2 in 4×1 MISO measurement	102
7.2.3.1 Experimental Arrangement (T2 and ExT2)	102
7.2.3.2 Results and Discussion.....	103
7.2.4 Comparison of ORG and ExORG in 4×1 MISO measurement	108
7.2.4.1 Experimental Arrangement (ORG and ExORG).....	108
7.2.4.2 Results and Discussion.....	108
7.2.5 Comparison of E2 and ORG array in 4×1 MISO measurement	112
7.2.5.1 Experimental Arrangement.....	112
7.2.5.2 Results and Discussion.....	112

7.2.6 Comparison of S2 and ORG in 4 × 1 MISO measurement.....	118
7.2.6.1 Experimental Arrangement.....	118
7.2.6.2 Results and Discussion.....	119
7.2.7 Comparison of NPT and ORG in 4 × 1 MISO measurement.....	124
7.2.7.1 Experiment Arrangement	124
7.2.7.2 Results and Discussion.....	124
7.3 Summary	129
Chapter 8 Antenna modelling using High Performance Computing (HPC).....	132
8.1 HPC-Alice.....	132
8.2 Modelling program construction on HPC	133
8.3 Optimized collocated heterogeneous antenna array	134
8.3.1 IV-1E.....	135
8.3.1.1 IV-1E with step 50cm.....	136
8.3.1.2 IV-1E with step 10 cm.....	148
8.3.2 IV-2E.....	158
8.4 HPC antenna array optimization analysis	164
Chapter 9 Conclusions	168
Reference	171
Appendix 1: T1 antenna array 2D and 3D radiation patterns	179
Appendix 2: T2 antenna array 2D and 3D radiation patterns	181
Appendix 3: Radiation patterns of ORG and Ex-ORG array (8.100 MHz).....	183
Appendix 4: Radiation patterns of T2 and Ex-T2 array (9.040 MHz).....	185

Chapter 1 Introduction

In the last decade, multiple input multiple out (MIMO) techniques have been widely applied in wireless communication systems due to its effectiveness in increasing spectral capacity. Many recent communication standards, such as IEEE802.11n, WiMAX and LTE, embed MIMO technology into their core framework. Unlike traditional single input single output systems (SISO), which only use one pair of antennas to transmit and receive signals, MIMO employs multiple antennas at both the transmitter and receiver creating multiple signal propagation paths (see Figure 1.1). When the signal is transmitted using MIMO, the probability that the signals suffer the same fading at the same time is significantly reduced. Hence, the signal can be transmitted more reliably with reduced error rate by using MIMO technique. This benefit of MIMO is due to the propagation diversity. MIMO can also enhance the data throughput capacity by employing spatial multiplexing. The original data can be divided into several different parts and simultaneously transmitted by multiple transmitting antennas. At the receiver, multiple antennas are employed and the original signals recovered by means of signal processing algorithms. Ideally, by using spatial multiplexing, the data throughput capacity can be linearly increased as the minimum of the number of transmitting or receiving antennas without extra bandwidth. As the spectral bandwidth is becoming increasingly valuable, effective spectrum usage makes MIMO an important wireless technique.

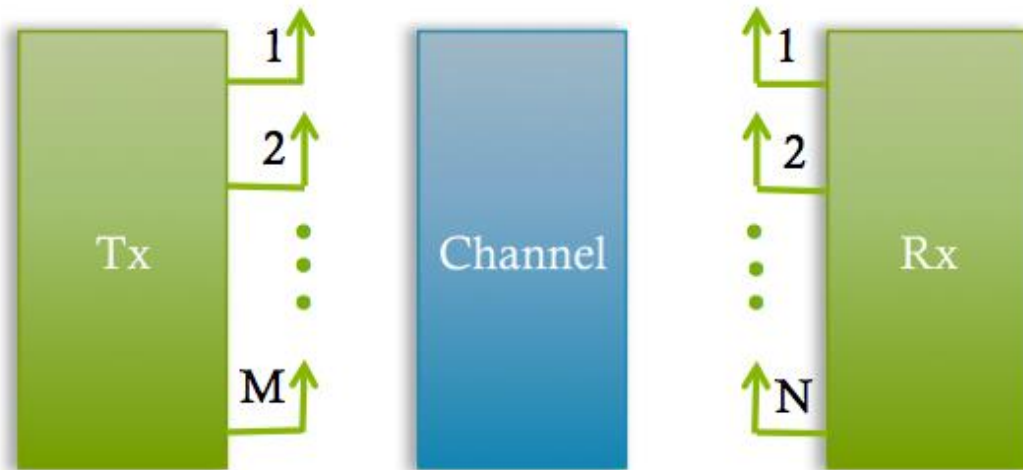


Figure 1.1 MIMO system

The concept of MIMO was firstly presented by Kaye and George [1970], where a frequency selected MIMO system was proposed when they investigated the optimum linear receiver for Pulse-Amplitude Modulation (PAM) signals. In 1974, Brandenburg and Wyner investigated the information capacity limits of MIMO channels and firstly proposed an analytical expression for MIMO channels capacity as a function of the nonzero eigenvalues of $H(f) \cdot H(f)'$, where $H(f)$ is the frequency selective channel matrix [Brandenburg and Wyner, 1974]. In order to remove the co-channel interference, Winters [1987] introduced the Minimum Mean Squared Error (MMSE) linear processing. The following equation was also firstly proposed in that paper.

$$C = \sum_i \log_2(1 + \rho \lambda_i) \text{ [bits/s/Hz]} \quad 1.1$$

where C is the MIMO channel capacity. λ_i represent the i th non-zero eigenvalue of H^*H' , ρ is the ratio between antenna consumed transmitting energy cost of one symbol and the thermal noise power spectral density.

Due to the inherent complexity of MIMO, especially in radio frequency design and signal processing area, the practical MIMO applications were still discouraged although its advantages compared with conventional SISO system had been well-known for decades. Foschini [1996] proposed the concept of Layered Space-Time (LST) architecture that applied in a point-to-point MIMO communication system. In this system, the single data stream was divided into several parallel bit streams and encoded independently and individually. In order to neutralize the effects of bad paths that may exist in some channels, the parallel data packages were sent to transmitting antennas periodically cycled. However, the requirements for efficient short layered coding schemes became the limitation for this architecture. In order to remove these limitations, a new architecture named Vertical Bell Laboratories Layered Space-Time Architecture (V-BLAST) was proposed by Foschini, Valenzuela and Wolniansky [1999]. Although the new architecture had a lower capacity compared to the previous one, the encoded data streams could be transmitted independently and the short coding schemes had been successfully removed. The more interesting result from those papers showed that: under some fading conditions, the transmission rate was proportionally to the $\min\{N_t, N_r\}$, where N_t and N_r were transmitter and receiver antenna numbers,

respectively [Foschini et al., 1998]. In other words, MIMO systems showed large spectral efficiencies with limited complexity according to the results of these papers.

MIMO research has entered a golden period since 1996 with a large number of research papers published every year, motivated by the results of Foschini. In 1998, a new class of channel codes named Space-Time Code was proposed by Tarokh etc [Tarokh et al., 1999]. At the same time, Raleigh and Cioffi introduced a Discrete Multitone technique (DMT) to neutralize the frequency-selective MIMO channel effects. This was considered as prototype of an Orthogonal Frequency Division Multiplexing (OFDM) technique [Raleigh et al., 1999]. In 1999, Telatar first investigated the relation between MIMO channel capacity and the distribution of Wishart matrix eigenvalues in a Rayleigh fading environment. Then the random matrix theory was proposed to analyse MIMO performance [Telatar, 1999]. This relation investigated by Telatar has been widely applied to analyse several aspects of MIMO systems in the following years. In 2002, Kermoal introduced “Kronecker” MIMO channel model which became the basis of many channel model standards in the same period [Kermoal et al., 2002]. The concept of MIMO multiple-access channels was introduced in the paper written by Viswanath, Tse and Anantharam [Viswanath et al., 2001]. Chiani, Win and Zanella deduced the exact expressions for the characteristic function of the MIMO capacity in the semi-correlated Rayleigh flat fading environment [Chiani et al., 2003]. In recent years, MIMO has

been widely discussed due to the rapid development of WiFi and LTE. Some topics like cellular MIMO, MIMO relaying channels etc still attract many talented researchers.

MIMO applications mainly focus on the UHF/VHF band, with little research conducted within HF band (3-30 MHz). The research conducted by Warrington et al [2008], Gunashekar et al [2008], Gunashekar et al [2009] and Gunashekar et al [2010] indicated that MIMO technology could also be applied to HF band. This thesis focuses on MIMO development within HF band, with particular concern on HF-MIMO antenna array design and modelling. A new concept based on pattern diversity is proposed in this thesis, which can be used to measure the correlation level between antenna array elements. Several antenna arrays based on this concept have been designed and tested via a 202 km radio link between Leicester and Lancaster in the last three years. The results of these campaigns showed that the newly designed arrays were more de-correlated than the referenced array. Furthermore, High Performance Computing (HPC) was employed in HF-MIMO antenna array modelling for the first time and a variety of antenna arrays were recommended according to different modelling frequencies and geometries.

Chapter 2 HF propagation environment

2.1 The ionosphere

The ionosphere is the upper region of atmosphere, which is ionized by solar radiations, such as ultraviolet and X-rays. The structure of the ionosphere is showed in Figure 2.1. Radio wave propagation will be affected if the number of free electrons is sufficient. The ionosphere is very variable due to many factors that can affect the electrons density, such as time of day, season, position with the solar cycle (11 years), geographical location etc. Generally, the electrons density reaches a maximum around midday, and is markedly reduced during the night. At and near sunspot maximum years, more ultraviolet radiation is generated by increased sunspot activity. This will lead to more ionization and allow higher radio frequencies to be reflected and refracted via the ionosphere. With more solar flare activity, the absorption effect at the bottom part of ionosphere D layer is also strengthened which may disrupt the global communications via the ionosphere. The ionosphere can be divided into three different regions:

D region

The D region is the innermost region of ionosphere, which is 50 km to 90 km above the surface of the earth. This layer region exists during daytime and reaches maximum density around midday. Due to the light ionization and high

recombination, HF radio waves suffer loss of energy when passing this region, especially for the frequencies in the lower end of the HF band (10 MHz and below). During solar proton events, the absorption effect of D region can reach unusually high levels over high and polar latitudes, which can cause HF radio communications to discontinue up to 48 hours.

E region

The E region exists from 90 km to 120 km above the surface of the Earth. The ionization in this layer is mainly due to solar soft X-rays. For the radio wave lower than about 10 MHz, it can be refracted and reflected by this layer; for higher frequencies signal, it can penetrate the layer. However, there is a special E layer named the sporadic E-layer (Es), which can support radio waves reflection up to 50 MHz or more. The sporadic-E event usually occurs in the summer and lasts from a few minutes to several hours.

F region

The F region is the upper region of ionosphere, which exists from approximately 200 km to more than 500 km above the surface of Earth. The ionization of this region is mainly due to solar extreme ultraviolet light. During the daytime, the F region is divided into the F1 (lower part) and F2 (upper part) regions. These two regions merge together at night. Since HF radio waves are mainly refracted and reflected by this layer, it is the most important layer to support HF communications.

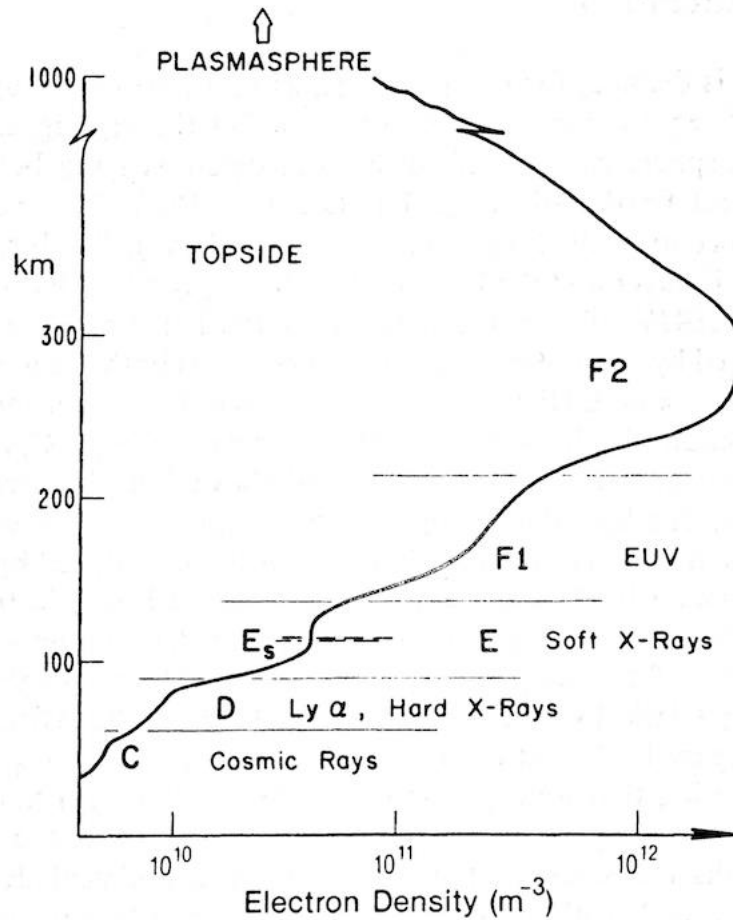


Figure 2.1 Structure of the ionosphere

(Source: Ionospheric Radio by Kenneth Davies [1990])

2.2 HF propagation fundamentals

When HF radio signals are launched from the earth's surface, they can be refracted and reflected back to the receiver via different ionosphere layers and numbers of hops. In order to get better description of electromagnetic wave propagation via a cold magnetized plasma medium, Appleton introduced the mathematical expression for the radio refractive index of the ionosphere [Davies, 1990].

The complex refractive index of the ionosphere n is given by:

$$n^2 = (\mu - i\chi)^2 = 1 - \frac{X}{1 - iZ - \frac{Y_T^2}{2(1-X-iZ)} \pm \left[\frac{Y_T^4}{4(1-X-iZ)^2} + Y_L^2 \right]^{1/2}} \quad 2.1$$

where:

$$X = \frac{N_e^2}{\epsilon_0 m \omega^2}, \quad Y_L = \frac{eB_L}{m\omega}, \quad Y_T = \frac{eB_T}{m\omega}, \quad Z = \frac{\nu}{\omega}$$

N_e is the charge density (electrons per cubic metre), ϵ_0 is permittivity of free space, m represents rest mass of an electron, ω is the angular wave frequency, e is the charge on an electron, B_L and B_T refer to the transverse and longitudinal components of the imposed magnetic field with reference to the direction of the wave normal.

For the E and F region, when the collisions can be negligible ($Z \approx 0$) and the real refractive index μ is deduced as:

$$\mu^2 = 1 - \frac{2X(1-X)}{2(1-X) - Y_T^2 \pm [Y_T^4 + 4(1-X)^2 Y_L^2]^{1/2}} \quad 2.2$$

When the magnetic field is negligible ($Y \ll 1$), the complex refractive index n can be expressed as:

$$n^2 = (\mu - i\chi)^2 = 1 - \frac{X}{1 - iZ} \quad 2.3$$

When both collisions and magnetic field effects are negligible, the real refractive index can be written as:

$$\mu^2 = 1 - X = 1 - \frac{N_e^2}{\epsilon_0 m \omega^2} \quad 2.4$$

Figure 2.2 shows possible simple propagation paths in a radio link. For instance, the term ‘2F’ means the signal which is reflected twice by the F layer.

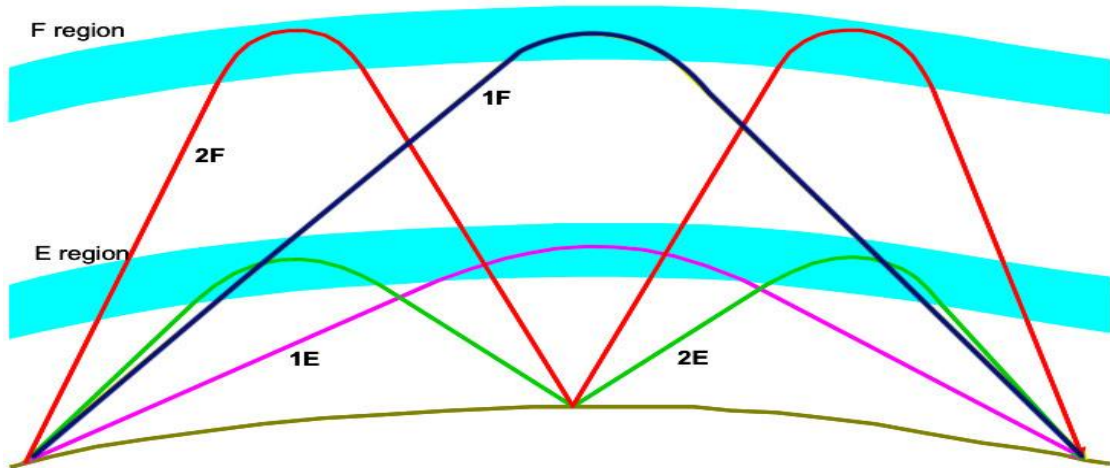


Figure 2.2 Simple HF propagation paths via ionosphere

During their transit through the ionosphere, the signals will be split into ordinary mode wave (O mode) and extraordinary mode wave (X mode) due to ionosphere interaction with the geomagnetic field. Generally, these two waves are elliptical polarized with opposite rotation and produce linear polarization in equatorial region and circular polarization in polar areas.

Unlike mobile communications where received signals tend to be from a variety of azimuth angles with similar elevation angles due to the effect of reflection and scattering from obstacles (e.g. buildings), HF signals generally arrive at the receiver

from the direction of the transmitter in almost the same azimuth angles but with different incident elevation angles.

2.2.1 Ionogram

An ionogram is a graph of the ionospheric virtual height as a function of radio frequency. The virtual height is the apparent height assuming the wave travels always in the straight line at the speed of light in vacuum, reflecting only once. It's produced using the data records generated by an ionosonde. Generally, the ground-based ionosonde transmits the pulsed signals up to the ionosphere with serial frequencies. With the frequency increase, the vertical launched signals will penetrate the ionosphere and not return. The minimum frequency that signals can vertically penetrate the ionosphere is called the critical frequency. The ionosonde records reflected and returned signal information, like time delay between the transmission of the pulse and its reception, to detect the ionosphere virtual height. Figure 2.3 shows an example ionogram obtained from the Chilton ionosonde station in the UK. The X-axis in the graph is the transmitted frequency sent by ionosonde, Y-axis indicates the virtual height for that frequency. O-Mode points and X-mode points are locus of received frequencies and corresponding virtual ranges for ordinary and extraordinary mode respectively. The two marked black curves in the figure indicate digisonde computed plasma frequency with true height and virtual height respectively.

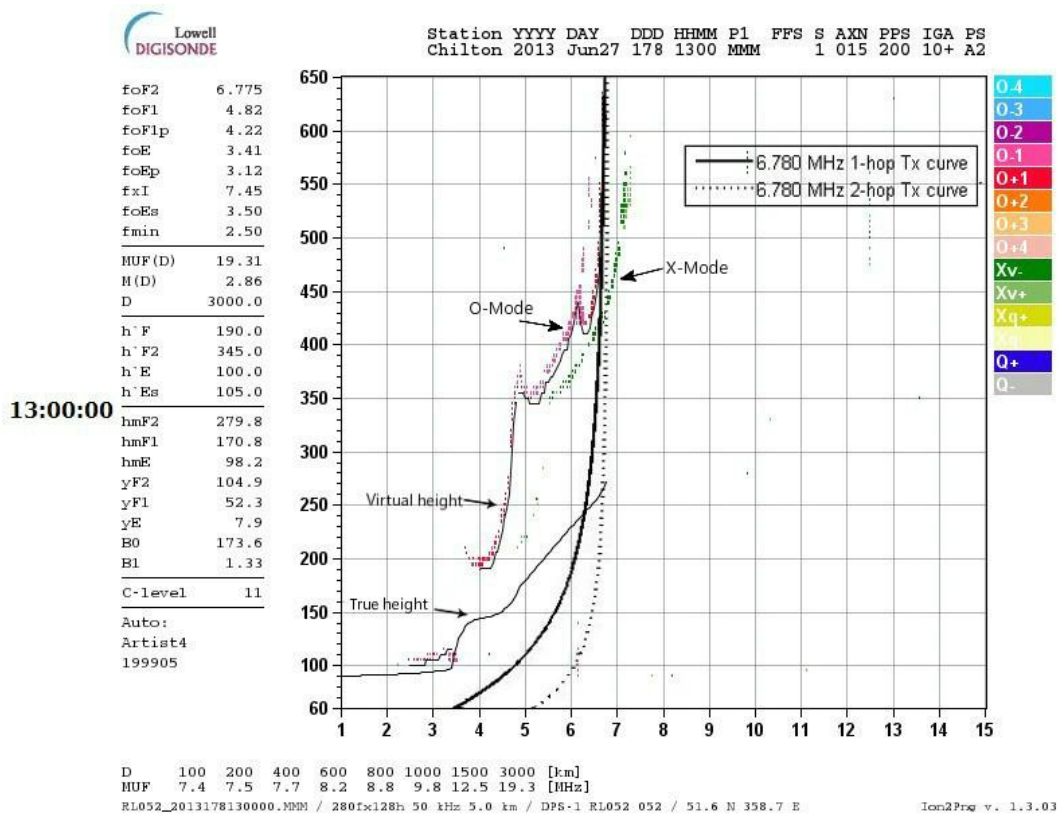


Figure 2.3 Example of Ionogram overlaid with transmission curves

2.2.2 The Secant Law and Transmission Curve

Assume that two simultaneous propagation experiments are carried out at the same time, one is oblique propagation and the other is vertical propagation (see Figure 2.4). If these two propagations paths have same true reflection height, the frequency f_v of the wave incident vertically is called the 'equivalent vertical frequency' corresponding to the frequency f_{ob} of the wave reflected obliquely.

The Secant Law states that the relationship between the frequency f_{ob} and the equivalent vertical frequency f_v is

$$f_{ob} = f_v \sec\theta_I \quad 2.5$$

where f_{ob} is the oblique wave frequency for the zenith angle θ_I and f_v is the frequency for the vertical wave.

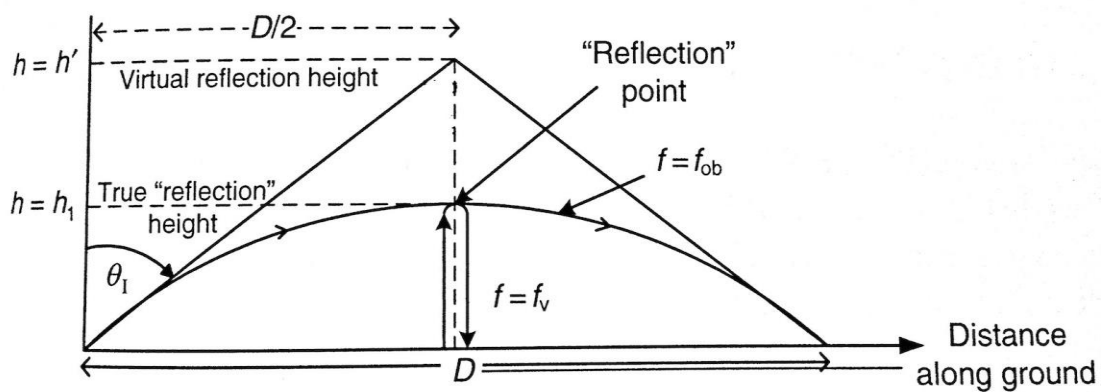


Figure 2.4 Oblique and vertical waves

(Source: Radiowave Propagation Physics and Applications by Curt A. Levis)

Note that $\sec\theta_I$ can also be expressed from the geometry as

$$\sec\theta_I = \sqrt{\left(\frac{D}{2h'}\right)^2 + 1} \quad 2.6$$

where D is the horizontal propagation distance between transmitting and receiving end for the oblique wave. h' represents the virtual height of a ray reflected by the ionosphere.

From the Secant law and the geometry path, it can be deduced that:

$$\frac{f_{ob}}{f_v} = \sec\theta_I = \sqrt{\left(\frac{D}{2h'}\right)^2 + 1} \quad 2.7$$

As a result, for a transmission over a distance D and 1-hop plane reflection occurs at a virtual height h' , the relationship between oblique and equivalent-vertical frequencies can be expressed as:

$$f_{ob} = f_v \sec\theta_I = f_v \left[\left(\frac{D}{2h'}\right)^2 + 1 \right]^{1/2} \quad 2.8$$

Then 1-hop virtual height h' can be deduced as:

$$h' = \frac{D}{2\sqrt{(f_{ob}/f_v)^2 - 1}} \quad 2.9$$

For a transmission over a distance D with a given value of f_{ob} , the virtual height h' is a function of the equivalent vertical frequency f_v . A transmission curve [Smith, 1939] is employed to present this relationship graphically. The 1-hop transmission curves are plotted using Equation 2.9.

Similarly, for the 2-hop transmission curves, the relationship between virtual height h'' and equivalent vertical frequency f_v can be deduced as:

$$h'' = \frac{D}{4\sqrt{(f_{ob}/f_v)^2 - 1}} \quad 2.10$$

Figure 2.3 displays the transmission curves for 1-hop and 2-hop signals with oblique frequency 6.780MHz and the transmission distance (D) 202 km (the distance of the radio link for experimental measurements). The virtual reflection heights can be obtained from the junction between ionosphere curves (O-Mode and

X-Mode curves) and transmission curves. The launched signal zenith angle can be deduced once the reflection virtual height has been obtained.

The virtual heights deduced by Equation 2.9 and 2.10 are based on the simple model assuming that ground is flat. Considering the effect of Earth curvature, the virtual height of ionosphere is increased by the distance H

$$H = a(1 - \cos \frac{\varphi}{2}) \quad 2.11$$

where a is the radius of the Earth, φ represents the angle at the centre of the Earth subtended by the propagation path D.

Since the transmission path (D) is 202 km in this thesis and the Earth radius a is 6378 km. The angle φ can be deduced as 1.8° . The increased distance of the virtual height considering the effect of Earth curvature is 0.79 km. This increased distance H can be neglected due to the reflection virtual height generally occurs from 350 km to 500 km, which produces an error of less than 0.23%.

Chapter 3 HF-MIMO background

3.1 Fundamental concepts of MIMO

MIMO diversity and spatial multiplexing are two fundamental aspects of MIMO technique. By using MIMO diversity, multiple antennas receiving signals via different propagation paths can significantly reduce the probability of the signal suffering the same deep fading. As a result, the transmission can be much more reliable in a multipath fading environment. The signal to noise ratio (SNR) can be enhanced significantly with fewer errors. By employing spatial multiplexing, the transmission data throughput linearly increases with the lower of the number of transmitting or receiving antennas in an independent and identically distributed channel environment. However, the full benefits of diversity and multiplexing cannot be realized simultaneously.

The trade-off between diversity and spatial multiplexing has been investigated by Zheng and Tse [2003], who showed that both diversity and spatial multiplexing could be obtained simultaneously with a trade-off system. Research on MIMO diversity mainly focuses on the aspect of antenna array design and spatial multiplexing focus on algorithm optimization. As the goal in this thesis is antenna array design for HF band, the MIMO diversity is mainly discussed instead of optimizing multiplexing algorithm. MIMO diversity mainly consists of the following three parts:

(1) Spatial diversity

Generally, spatial diversity employs multiple antennas with the same characteristics (homogeneous array) to send or receive signals at different locations. These antennas are usually separated from each other with half a wavelength or more. For instance, as shown in Figure 3.1, the received signal at Rx1 is produced by the combination of two different signals indicated by solid lines via representing 1-hop and 2-hop propagation. At the same time, the received signal at Rx2 is also a combination of two different signals indicated by dotted lines, which travel different paths compared with the solid-line signals. The difference in path lengths between the 1-hop and 2-hop signal mean that the received signals have a different phase relationship between Rx1 and Rx2. The different phase relationship between the received signals mean that the correlation coefficient is reduced. In order to obtain sufficient decorrelation for the received signals, half a wavelength or more is required for antenna separation distance [Jakes, 1994]. However, this means that several tens of metres may be needed to get half wavelength spacing for HF antenna arrays. An example of antenna array using spatial diversity is displayed in Figure 3.2.

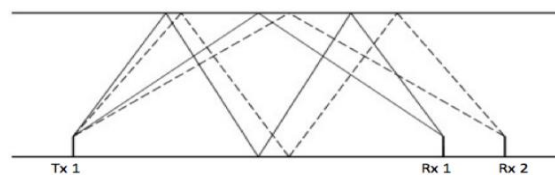


Figure 3.1 Schematic of signal propagation paths with spatial diversity at receiver

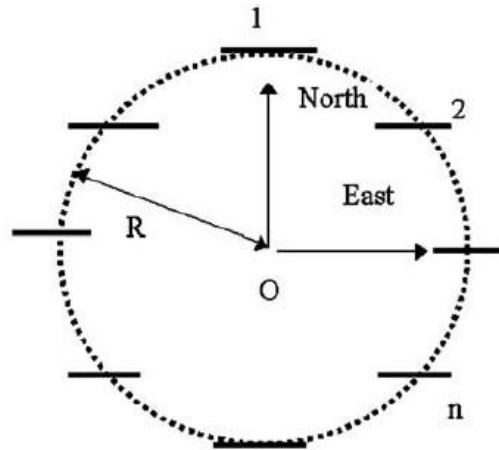


Figure 3.2 Homogeneous circular array composed of 8 identical loop antennas with same orientation (Source: Erhel et al [2004])

(2) Antenna radiation pattern diversity

If homogeneous antennas are employed in the same location, solid-line paths in Figure 3.1 will become the same as dotted-line paths (see Figure 3.3), which means that the phase relationships of received signals are the same between Rx1 and Rx2. However, if co-located heterogeneous antennas are used to send or receive signals instead of homogeneous antennas, due to different antennas responses (radiation pattern diversity), the phase relationships can also be different for the received signals.

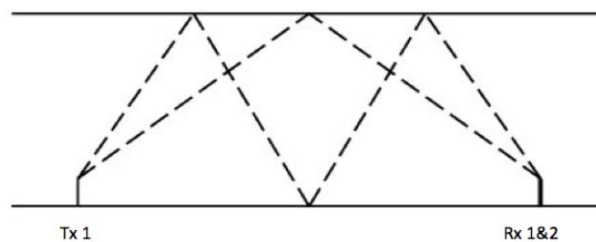


Figure 3.3 Schematic of signal propagation paths with pattern diversity at receiver

Pattern diversity uses heterogeneous antenna arrays to achieve propagation variety. Heterogeneous antenna arrays can consist of different types of antenna [e.g., Marie et al., 2000; Oger et al., 2006], or the same types of antenna elements with different orientations (see Figure 3.4) [e.g., Erhel et al., 2004; Gunashekar et al., 2009a]. Both of these cases allow two antennas in the receive array to have different antenna pattern responses to signals from the same direction. As a result, the received signals can become different due to the different antenna responses even with the same propagation path.

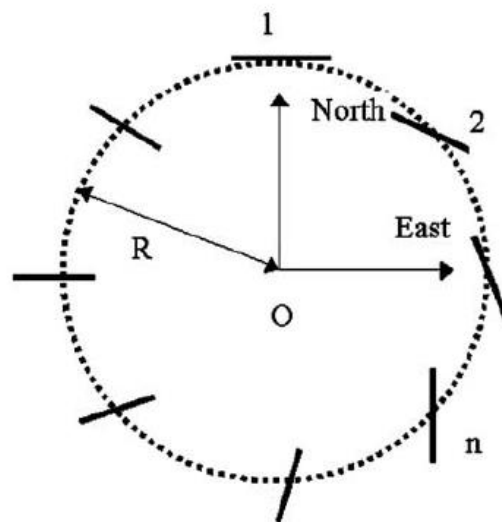


Figure 3.4 Heterogeneous circular array: the array is composed of 8 identical loop antenna with different orientations (Source: Erhel et al [2004])

(3) Polarization diversity

This kind of diversity employs antennas with different polarizations to reduce the effect of polarization mismatch. If a horizontal polarized signal meets a vertical polarized receiving antenna, there will be no signal at the output of the antenna due

to the completely mismatch. In order to avoid such kind of attenuation, multiple antennas with different polarizations can be employed both in transmitting and receiving ends [Andrews et al., 2001].

3.2 MIMO channel capacity calculation

Channel capacity is the maximum data rate that information can be transmitted over a communication channel with arbitrarily small error probability. The concept of channel capacity was proposed by Shannon [1948]. In this paper, mutual information is defined as:

$$I(X; Y) = H(Y) - H(Y|X) \quad 3.1$$

Where $H(Y)$ is the entropy of Y ; $H(Y|X)$ represents the conditional entropy of Y , given the knowledge of variable X .

For a single channel, the channel capacity can be expressed as:

$$C = \max I(X; Y) = \max[H(Y) - H(Y|X)] \quad 3.2$$

MIMO channel capacity is an extension of the mutual information formula for a SISO channel given by the above equation to a channel matrix. Consider the MIMO system employs N_t transmitter antennas and N_r receiver antennas, x denotes the transmitted signals vector and y denotes the received signal vector. The relation between x and y can be expressed as:

$$y = Hx + n \quad 3.3$$

Where H is the MIMO channel matrix and n is the additional channel noise vector.

The MIMO channel matrix H can be expressed as:

$$H = \begin{bmatrix} h_{1,1}(r, t) & \cdots & h_{1,N_t}(r, t) \\ \vdots & \ddots & \vdots \\ h_{N_r,1}(r, t) & \cdots & h_{N_r,N_t}(r, t) \end{bmatrix} \quad 3.4$$

$h_{i,j}(r, t)$ is the impulse response between the j th ($j = 1, 2, \dots, N_t$) transmit antenna and the i th ($i = 1, 2, \dots, N_r$) receive antenna.

The MIMO channel capacity can be estimated using Equation 3.5 [Razavi-Ghods et al., 2004]

$$C = \log_2 \left[\det \left(I_{N_r} + \left(\frac{\rho}{N_t} \right) HH^* \right) \right] \text{ bps/Hz} \quad 3.5$$

where ‘ \det ’ means determinant, I_{N_r} means $N_r \times N_r$ identity matrix, ρ is the signal to noise ratio (SNR), H^* is the conjugate transpose of the complex channel matrix H .

Shiu et al [2000] deduced that the capacity of MIMO channel can be written as Equation 3.6

$$\begin{aligned} C &= \log_2 \left[\det \left(I_{N_r} + \left(\frac{\rho}{N_t} \right) HH^* \right) \right] \text{ bps/Hz} \\ &= \sum_{i=1}^k \log_2 \left(1 + \left(\frac{\rho}{N_t} \right) \lambda_i \right) \text{ bps/Hz} \end{aligned} \quad 3.6$$

where $k = \min\{N_r, N_t\}$, λ_i are the eigenvalues of HH^* .

Equation 3.6 shows that the MIMO channel capacity is the sum of the capacity of k SISO channels, and MIMO capacity depends on the eigenvalues λ_i of the channels. As a result, higher MIMO channel capacity can be achieved by reducing the correlation of sub-channels.

3.3 MIMO in HF band

Since it has the advantage in improving of communication reliability and enhancing the data throughput rate without extra bandwidth, the MIMO technique has been widely applied in wireless communications in the last decade, especially focused on VHF, UHF and SHF bands [Foschini, 1996; Shiu et al., 2000; Wallace and Jensen, 2002; Lim et al., 2007]. The success of MIMO application requires a sufficiently multipath propagation environment. In mobile communications, since signals can be reflected and scattered by variety of buildings, the multipath-propagation can be easily obtained in the urban environment. As shown in Chapter 2, HF waves can be refracted and reflected via different ionosphere layers. For each single ionosphere layer (eg, F layer), the signals may also be reflected more than once. Furthermore, the wave will be split into ordinary and extraordinary waves (O and X mode) once it meets the ionosphere. Both of these two modes are elliptically polarized with opposite rotation. Due to the ionosphere's different responses, the propagation path will also be different for these two waves. As a result, the HF incident wave at the receiver can be obtained from different

layers, hops and modes. It is worth noting that, unlike cellular communications where multiple signals come from different azimuth angles with similar elevation angles (see Figure 3.5), for long distance HF communications via the ionosphere, the multiple signals are generally obtained from different elevation angles with similar azimuth angles (see Figure 3.6).

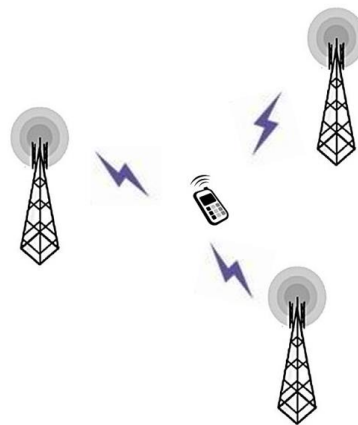


Figure 3.5 Cellular communication: receiver antenna picks up signals from different azimuth angles with similar elevation angles

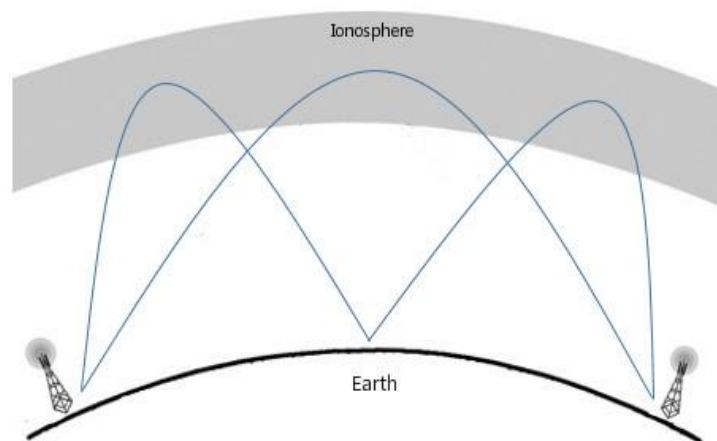


Figure 3.6 HF communication: receiver antenna picks up signals from different elevation angles with similar azimuth angles

3.4 Development of HF antenna arrays

The development of the HF antenna array usually accompanied the evolution of the direction finding (DF) technique, which was a highly prized technology in terms of military applications, especially during World War I and II. Early DF systems employed a rotated loop antenna to achieve directional sensitivity. In order to improve the system, Ettore Bellini and Alessandro Tosi used an antenna array (assembled from 2 antennas) to replace the loop antenna in 1907, which could be the earliest HF antenna array application. In 1919, Adcock [1919] invented an antenna array, which took his name, consisting of four vertical monopole antennas. As there is no horizontal antenna in the array, it cuts out the horizontally polarized distortions due to ionospheric disturbances and reflections, which is the main problem suffered by using loop antenna. Dr. Hans Rindfleisch introduced a large receiving antenna array named Wullenweber used for DF system during the early years of World II. The Wullenweber is more technically known as Circular Disposed Antenna Array (CDAA) or Circular Disposed Dipole Array (CDDA). The first Wullenweber was built during the war at Skibsby, Denmark. The array employed 40 vertical dipole antennas located on the arc of a circle with a radius of 60 metres. In order to get a better receiving signal, another 40 reflecting components were installed on a wooden support construction with a diameter of 112.5 metres. The north and south antennas were placed exactly on the North-South meridian in order to obtain true geographic bearing more conveniently.

Some of Wullenweber arrays are still in service today, but most of them were dismantled due to the development modern DSP technology.

There are several antenna arrays designed for transmitting purpose. Curtain array is one of classic HF transmitting antenna array, developed during the 1920s and 1930s. Generally, the array employs multiple half-wave dipole antennas as radiator elements, suspended in the radiator plane. These antennas are fed in phase and the radiator plane is located in front of the reflector plane (curtain) with a distance $\frac{1}{4}$ wavelength. The “curtain” reflector is consisted by many long parallel wires that suspended on the support construction. The support structure is usually made by two or more steel towers and the support wires between these towers. Griffith [2000] reported that curtain arrays can obtain a gain more than 20 dB compare with a simple dipole antenna. Both horizontally and vertically polarized signals can be generated by the array, depending the orientation of the dipoles in the array.

In 1998, Erhel introduced a heterogeneous circular array (see Figure 3.7) for radio direction finding in the HF band. The array consisted of 8 vertical loop antennas and there was 45° rotation in the vertical axis for each adjacent antenna. The initial radius for the array was 12 m, then gradually down to 1.8 m, the array becoming a circle and the antennas being collocated. The experimental measurement showed that the transmitter could be located clearly by using both of these two configurations [Erhel et al., 1998]. These results indicated that collocated antennas array could be used for direction finding and the idea of employing the array with

collocated elements to achieve higher data rates for HF communications was sparked.

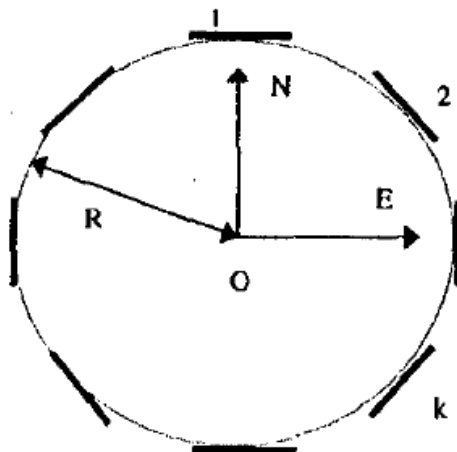


Figure 3.7: Heterogeneous circular array (Source: Erhel et al [1998])

In 2004, in order to improve the reliability and quality of communications within the HF band, Xu proposed a new HF transmission system employing MIMO and OFDM techniques. The simulation results showed that the performance of the MIMO model combined with OFDM could improve the SNR by as much as 20 dB compared with single carrier [Xu et al., 2004]. Strangeways [2006] investigated the signal correlation between spaced antennas using an HF wideband simulator model with different propagation modes. The simulator could support multipath HF signal random channel simulation in the real fluctuating ionosphere. The simulation result indicated that the spatial correlation for the receiving antennas depends on the variance of the electron density irregularities and the correlation level is higher for the received signals reflected via F layer compared with E layer. However,

decreasing the transmitting frequency to use E layer reflection will decrease the channel capacity due to the reduced SNR.

In order to investigate the feasibility of MIMO techniques within HF band, several experimental campaigns has been carried out by Gunashekar et al [2009, 2010], using a 255 km radio link built between Leicester and Durham. Several compact collocated antenna arrays, like ‘X-Y-Z’ loop array (Figure 3.8), ‘Ground Symmetric’ Loop array (Figure 3.9), crossed dipole with single monopole array (Figure 3.10) and dual perpendicular octagonal loop array (Figure 3.11), were utilized during the measurements. The details of these compact antenna arrays have been reported by Feeney et al [2009]. The campaigns results showed that:

- 1 By using homogeneous antenna arrays, more than half a wavelength was required in order to obtain a significant decorrelation between received signals. For the HF band, this could be several tens of metres for the elements spacing.

- 2 Collocated compact heterogeneous antenna arrays showed a similar or even better level of decorrelation compared with large spaced antenna arrays, which means that antenna pattern diversity could be used to replace spatial diversity to achieve an increased MIMO channel capacity.

- 3 The number of ionospheric modes has a significant effect on the correlation level of antenna array elements. More ionospheric modes results in a lower level of signal correlation and higher MIMO channel capacity.



Figure 3.8 'X-Y-Z' Loop receiver antenna array

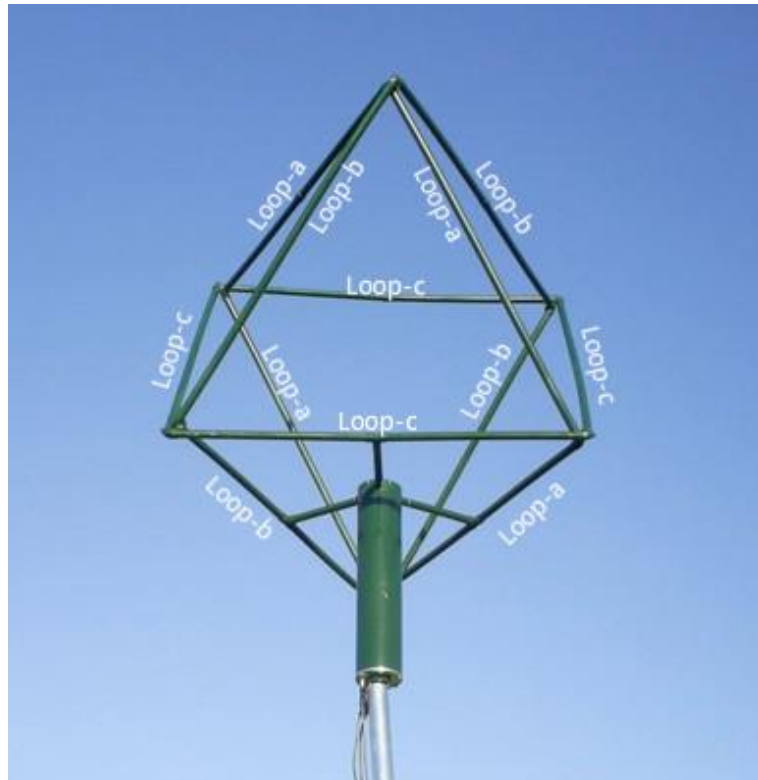


Figure 3.9 'Ground Symmetric' Loop receiver antenna array



Figure 3.10 Crossed dipole with single monopole receiver antenna array



Figure 3.11 Dual perpendicular octagonal loop transmitter antenna array

Chapter 4 Numerical electromagnetics code (NEC) modelling

4.1 Numerical Electromagnetics Code

The Numerical Electromagnetics Code version 2 (NEC-2) is a public domain computer code for the design and analysis of the electromagnetic response of antennas in general. The code was developed by G.J.Burke and A.J.Poggio at Lawrence Livermore National Laboratories (LLNL) in 1981 [Smith, 2008]. Version 4 (NEC-4) was developed in 1990s, but the program is licensed by LLNL and is under United States export control. As a result, NEC-2 is the highest version of the code within the public domain without a license, and the modelling in this thesis was carried out with a NEC-2 engine.

NEC-2 uses the method of moments [Harrington, 1987] numerical solution for the electric-field integral equation (EFIE) and magnetic-field integral equation (MFIE) to calculate electromagnetic response of conductors with different structures [Burke and Poggio, 1981]. The EFIE is attractive for thin-wire structures while the MFIE is more suitable for smooth surfaces. For HF-MIMO antenna design project, the EFIE is used as the designed antenna arrays are thin-wire structures. Antenna array elements are divided into small segments. For each segment, NEC-2 takes the method of moments solution for EFIE to calculate the E-field magnitude and phase response. Then these responses are summed to generate the whole radiation pattern for the antenna array.

4.1.1 Modelling working region

Electromagnetic waves are generated by an antenna when a current flows in it. The wave will propagate from the location of the radiating source to infinity. According to the different behaviour of the fields surrounding an antenna, the space can be divided into three regions:

(1) Far Field or Fraunhofer Region

For antenna when physically maximum dimension or aperture width (D) is large compared to the wavelength λ , the far field region (Fraunhofer region) starts from $\frac{2D^2}{\lambda}$ to infinity. At the same time, the far field region must satisfy another two conditions: 1) $R \gg D$; 2) $R \gg \lambda$. In this region, the fields are falling off with $\frac{1}{R}$ and the power density is falling off with $\frac{1}{R^2}$. However, radiation pattern keeps the same shape with the region radius (R) increment.

(2) Reactive Near Field

The region where $R < 0.62\sqrt{\frac{D^3}{\lambda}}$ is commonly named the reactive near field region. In this region, unlike far field (E-field and H-field are orthogonal propagating but in phase), the fields are mainly reactive fields, which means the E-field and H-field has 90° phase difference to each other.

(3) Radiating Near Field or Fresnel Region

The region $0.62\sqrt{\frac{D^3}{\lambda}} < R < \frac{2D^2}{\lambda}$ is called radiating near field (Fresnel) region.

In this area, the reactive fields are not predominant and the radiating fields start

to emerge. The relationship between E-field and H-field becomes very complex and the radiation pattern shape may change obviously with distance.

As the intended target is in the far field, this is the most important region for this research, and is the only region dealt with by the NEC software.

4.1.2 Modelling guidelines

The segment length becomes the first consideration when modelling the antenna arrays. Since the EFIE starts the computation from the middle of each segment, the length of the segments determines the resolution in solving for the currents in the antenna model. Although there is no limitation for the segments length and more segments number taken, more accuracy can be obtained, the relationship between the segment length Δ and the wavelength λ become the important standard to measure the modelling accuracy. In general, Δ should be set at the interval from approximately 0.001λ to 0.05λ at the desired frequency in order to prevent numerical inaccuracy. If the model needs different lengths of segments, the ratio of larger segment length to smaller segment length should be less than 5.

The antenna model wire radius α should satisfy the following case [Smith, 2008]:

- 1) λ/α should be greater than 30
- 2) $2\pi\alpha/\lambda \ll 1$
- 3) Δ/α must be greater than 8 in order to keep the errors below 1%. When

Extended Thin-Wire Kernel (EK) command is used, this value can be as small

as 2 without error rate increasing.

NEC-2 can only support the modelling structure above the ground. If the antenna model wires have some underground parts, the engine will stop work and an error will be shown. For the ground environment, NEC-2 supplies several conditions with different relative dielectric constants and conductivities: free space, perfect ground, poor ground (dielectric constant: 3.0, conductivity: 0.0010 Sm^{-1}), average ground (dielectric constant: 13.0, conductivity: 0.0050 Sm^{-1}), good ground (dielectric constant: 20.0, conductivity: 0.0303 Sm^{-1}), fresh water (dielectric constant: 80.0, conductivity: 0.0010 Sm^{-1}) and salt water (dielectric constant: 81.0, conductivity: 5.000 Sm^{-1}). Manually input values for dielectric constant and conductivity is also available for NEC-2.

Although there is no particular restriction for the angle of the intersection of wire segments in NEC-2, the angle should not be too small. Obtuse angle for the intersection is recommended. If the angle is too small, the segments will be overlapped and an error will occur. In addition, the voltage source segment should be vertical if the segment is connected to a ground plane.

For HF-MIMO project, the licensed transmission frequencies are 6.780 MHz, 8.100 MHz and 9.040 MHz, with corresponding wavelengths λ of 44.25 m, 37.04 m and 33.19 m respectively. The maximum single segment length Δ used in the modelling is about 0.1 m and minimum segment is approximately 0.03 m to ensure that Δ is in the range 0.001λ to 0.05λ . Antenna model wire radius is unified

with AWG#14 wire (radius: 0.8140 mm) except the antenna mast, which diameter is 5 cm. Average ground (dielectric constant: 13.0, conductivity: 0.0050 Sm^{-1}) is used for all the current model work.

The antenna arrays in this thesis were modelled as collocated instead of single antenna simulation. The coupling effect has been considered when NEC simulations were undertaken.

4.1.3 Modelling software CocoaNEC and NEC2C

CocoaNEC is an antenna designing and modelling application based on Mac OS X written by Kok Chen [Aminaei et al, 2014]. The software employs NEC-2 and NEC-4 (licence required) as the compute engine.

CocoaNEC provides two kinds of input methods for describing an antenna model structure: 1) programming language NEC-C (NC) model. The syntax and grammar of the NEC-C is very similar to C language. The advantage of using NEC-C language for the modelling is more flexible to control variables especially when writing optimizing loops. 2) spread-sheet interface model. Antenna model is expressed using XYZ coordinate. Users only need to input the start and end point coordinate for antenna wires (see Figure 4.1). Then set up parameters such as: wire radius, segments number, location of the excitation and frequency etc. After run the application, the model will be computed automatically. The spreadsheet interface model is much more intuitive and acceptable for beginners. Both of these two models

	Azimuth	Elevation	3D	Smith Chart	Scalar	Geometry	Summary	Cards	NEC2 Output
1	CM	COCOANEC 2.0 2015-01-07 22:41 2015-01-07 22:41							
2	CE	-----							
3	GW	1	21	0.000000	-5.18000	12.19200	0.000000	5.180000	12.19200 8.14E-04
4	GE	1							
5	FR	0	1	0	0	14.08000	0.000000		
6	GN	0	0	0	0	20.00000	0.030300		
7	EX	0	1	11	1	1.000000	0.000000		
8	XQ								
9	RP	0	1	360	1000	70.00000	0.000	0.000	1.000 5.100E+03
10	RP	0	360	1	1000	-90.000	0.000000	1.000	0.000 5.000E+03
11	RP	0	91	120	1001	0.000	0.000	2.000	3.000 5.000E+03
12	XQ								
13	EN								

Figure 4.2 NEC-2 standard input card: the sample includes two comment commands (CM, CE), two geometry commands (GW, GE), five program control commands (GN-ground, FR-frequency, EX-excitation, RP-radiation pattern, EN-end)

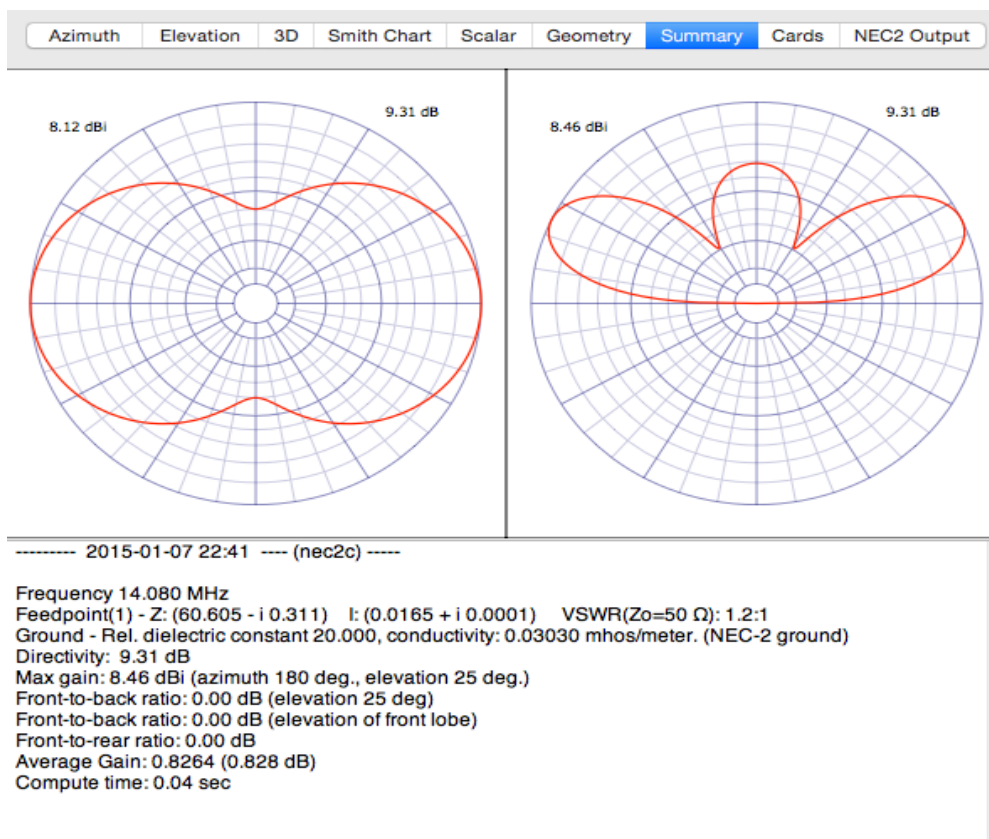


Figure 4.3 Summary provides antenna fundamental parameters for antenna modelling, including radiation pattern, directivity, max gain etc.

```

----- RADIATION PATTERNS -----
RANGE: 5.000000E+03 METERS
EXP(-JKR)/R: 2.00000E-04 AT PHASE: -28.16 DEGREES

---- ANGLES -----
THETA  PHI      VERTC  POWER GAINS  TOTAL  POLARIZATION  E(THETA)  E(PHI)
DEGREE DEGREE  DB     DB     DB     RATIO  DEGREE SENSE  MAGNITUDE  PHASE  MAGNITUDE  PHASE
1.00   0.00   -17.22 -87.16 -17.22 0.0002  0.02  LEFT  1.1494E-06 -138.01 3.6610E-10 -104.61
2.00   0.00   -17.01 -87.16 -17.01 0.0002  0.01  LEFT  1.1782E-06 -137.20 3.6601E-10 -104.61
3.00   0.00   -16.80 -87.16 -16.80 0.0002  0.01  LEFT  1.2064E-06 -136.43 3.6588E-10 -104.62
4.00   0.00   -16.61 -87.17 -16.61 0.0002  0.01  LEFT  1.2338E-06 -135.72 3.6569E-10 -104.63
5.00   0.00   -16.42 -87.17 -16.42 0.0001  0.01  LEFT  1.2605E-06 -135.05 3.6544E-10 -104.63
6.00   0.00   -16.24 -87.18 -16.24 0.0001  0.01  LEFT  1.2863E-06 -134.42 3.6514E-10 -104.64
7.00   0.00   -16.08 -87.19 -16.08 0.0001  0.01  LEFT  1.3113E-06 -133.83 3.6478E-10 -104.65
8.00   0.00   -15.92 -87.20 -15.92 0.0001  0.01  LEFT  1.3354E-06 -133.28 3.6436E-10 -104.67
9.00   0.00   -15.77 -87.21 -15.77 0.0001  0.01  LEFT  1.3584E-06 -132.77 3.6389E-10 -104.68
10.00  0.00   -15.63 -87.22 -15.63 0.0001  0.01  LEFT  1.3805E-06 -132.29 3.6336E-10 -104.70
11.00  0.00   -15.50 -87.24 -15.50 0.0001  0.01  LEFT  1.4016E-06 -131.84 3.6277E-10 -104.71
12.00  0.00   -15.38 -87.25 -15.38 0.0001  0.01  LEFT  1.4216E-06 -131.42 3.6211E-10 -104.73
13.00  0.00   -15.26 -87.27 -15.26 0.0001  0.01  LEFT  1.4405E-06 -131.03 3.6140E-10 -104.75
14.00  0.00   -15.15 -87.29 -15.15 0.0001  0.01  LEFT  1.4582E-06 -130.67 3.6063E-10 -104.78
15.00  0.00   -15.06 -87.31 -15.06 0.0001  0.01  LEFT  1.4749E-06 -130.34 3.5979E-10 -104.80
16.00  0.00   -14.97 -87.33 -14.97 0.0001  0.01  LEFT  1.4903E-06 -130.03 3.5889E-10 -104.82
17.00  0.00   -14.88 -87.36 -14.88 0.0001  0.01  LEFT  1.5046E-06 -129.75 3.5792E-10 -104.85
18.00  0.00   -14.81 -87.38 -14.81 0.0001  0.01  LEFT  1.5177E-06 -129.49 3.5689E-10 -104.88
19.00  0.00   -14.74 -87.41 -14.74 0.0001  0.01  LEFT  1.5296E-06 -129.26 3.5578E-10 -104.90
20.00  0.00   -14.68 -87.44 -14.68 0.0001  0.01  LEFT  1.5403E-06 -129.05 3.5461E-10 -104.93

```

Figure 4.4 Part of NEC2 standard output file sample. NEC2 uses a conventional spherical coordinate system (THETA, PHI) to express a certain direction or position. The output file provides power gains, polarization, magnitude and phase information for a certain point.

NEC2C is a Linux version of NEC-2 written by Neoklis Kyriazis using C language. It was translated from the original NEC-2 (written in Fortran). Like other versions of NEC-2, it can read standard NEC input cards and produce the standard NEC output file. Due to the operating system requirement, NEC2C was installed on High Performance Computing (HPC) cluster ALICE in University of Leicester. The details of modelling using HPC are explained in Chapter 8.

4.2 Modelling Methodology

After several experimental campaigns in the last five years, Warrington et al [2008] and Gunashekar et al [2008] investigated MIMO feasibility in the high frequency (HF) band. In the preliminary experiments, conventional spaced antenna arrays were employed at both ends of a radio link. The results indicated that the antenna arrays could provide significantly low values of correlation coefficient between the array elements at both sides when the inter-elements spaced at nearly half wavelength or more. Then co-located, heterogeneous antenna arrays were tested in the campaigns. The newly designed heterogeneous arrays showed a good decorrelation level between antenna array elements, which means that traditional widely spaced homogeneous HF antenna arrays could be replaced by co-located heterogeneous ones [Gunashekar et al, 2010]. In other words, radiation pattern diversity can be used to decrease the correlation level of antenna array elements instead of spatial diversity due to the large space requirement. The bivectorial model is used in this thesis in order to get better understand how the radiation pattern diversity works.

4.2.1 The Bivectorial Model

The bivectorial model was proposed by Bertel [1996] in order to research the narrow band signal model in ionospheric high frequency (3-30 MHz) channel.

Assume the signal launched by transmitter is:

$$e(t) = m(t)e^{j\omega_0 t} \tag{4.1}$$

where $m(t)$ is the modulation of the signal, ω_0 represents the carrier angular frequency. After joining the transit through the ionosphere, the radio wave will be split into O and X mode in general case.

The received signal for the k^{th} mode of propagation can be written as:

$$s_{rk}(t) = A_k m(t - \tau_{gk}) e^{j\omega_{rk}(t - \tau_{pk})} \quad 4.2$$

where A_k is the k^{th} model attenuation, τ_{gk} and τ_{pk} is the group and phase delay corresponding to the k^{th} model respectively, ω_{rk} is the angular frequency for the arrived signal included the Doppler shift.

For MIMO system, the output signal at the antenna i , transmit by the antenna l , can be expressed as:

$$X_{rli}(t) = \sum_{k=1}^{N_s} G_{lk} e^{j\gamma_{lk}} F_{ik} e^{j\delta_{ik}} s_{rk}(t) + n_i(t) \quad 4.3$$

where k identifies the O and X mode propagation paths, N_s is the number of path. G_{lk} and F_{ik} is the transmitting and receiving antenna response respectively. γ_{lk} and δ_{ik} represent the phase shift at the transmitter and receiver end respectively. $n_i(t)$ is the additive noise.

Traditional spatial diversity can be incarnated in different phase delay τ_{pk} due to the propagation path difference. The path difference for incident waves k_1 and k_2 at receiving antenna i_1 is not same as the path difference for incident signals k_3 and k_4 at receiving antenna i_2 . The different path lengths differences mean that

k_1 and k_2 has a different phase relationship compared with k_3 and k_4 . The different phase relationships between incident waves means the correlation coefficient is reduced for the output signals from receiving antennas.

Assume that receiving antenna i_1 and i_2 is moved to the same place, in that case, the propagation path difference will be the same, the angle of arrival will be identical and spatial diversity will be removed. However, if heterogeneous antenna is applied for i_1 and i_2 , the antenna i_1 response $F_{i_1k}e^{j\delta_{i_1k}}$ will be different with antenna i_2 response $F_{i_2k}e^{j\delta_{i_2k}}$, the combination relationship within $X_{rli_1}(t)$ can also be different with $X_{rli_2}(t)$. It is also suitable for transmitting side. In that case, the correlation level between the output signals can be reduced by using different $G_{ik}e^{j\gamma_{ik}}F_{ik}e^{j\delta_{ik}}$, which means that the antenna radiation pattern diversity can be used to replace spatial diversity if there is space limitation. Previous experiments designed by Gunashekar et al [2010] have shown that the radiation pattern diversity can be applied in HF-MIMO system instead of spatial diversity.

4.2.2 Radiation pattern diversity effect on correlation coefficients based on 2×2

MIMO simulation

In order to investigate the amplitude and phase effect on received signal, a 2×2 MIMO ideal model is employed in the simulation. For incident waves it is assumed that one signal is from the E layer and the other one from the F layer. The magnitude (A_{TE} and A_{TF}) and phase (P_{TE} and P_{TF}) of the incident waves are set to be same in order to identify the radiation pattern diversity easily. The output signal S1 from Rx1 can be written as:

$$S1 = A_{TE} e^{j(2\pi(f+f_{dE})+P_{TE})} M_{1E} e^{jP_{R1E}} + A_{TF} e^{j(2\pi(f+f_{dF})+P_{TF})} M_{1F} e^{jP_{R1F}} \quad 4.4$$

where M_{1E} and M_{1F} is the Rx1 magnitude response for incident wave from E and F layer respectively, P_{R1E} and P_{R1F} represent the phase response of Rx1 for E and F layer signal. f_{dE} and f_{dF} are the Doppler shift for the incoming signals via the different paths.

At the receiver Rx2, the output signal S2 can be expressed as:

$$S2 = A_{TE} e^{j(2\pi(f+f_{dE})+P_{TE})} M_{2E} e^{jP_{R2E}} + A_{TF} e^{j(2\pi(f+f_{dF})+P_{TF})} M_{2F} e^{jP_{R2F}} \quad 4.5$$

where M_{2E} and M_{2F} is the Rx2 magnitude response for incident wave from E and F layer respectively, P_{R2E} and P_{R2F} represent the phase response of Rx2 for E and F layer signal.

The incident signals frequency f is set to be constant and the Doppler shift f_{dE} and f_{dF} is set to be 1 Hz and 1.1 Hz respectively. In order to simplify the simulation model, $A_{TE} = A_{TF} = 1$, $P_{TE} = P_{TF} = 0$. The following Table 4.1 shows the receiving antennas magnitude response effect on correlation coefficient of antenna output signals amplitude, when antenna phase response $P_{R1E} = P_{R1F} = P_{R2E} = P_{R2F} = 0$.

Table 4.1 Antenna magnitude response effect on correlation coefficients of amplitude of received signals using random values for the magnitude response combination. The phase delays for these two antennas are set to be identical

$$(P_{R1E} = P_{R1F} = P_{R2E} = P_{R2F} = 0).$$

$(M_{1E}, M_{1F}, M_{2E}, M_{2F})$	Correlation coefficient of received signals amplitude
(1,1,1,1)	1
(1,2,1,1)	0.9940
(1,2,1,3)	0.9991
(2,3,6,1)	0.9923
(2,3,1,6)	0.9923
(2.3, 3.8, 6.2,1.7)	0.9966
(3, 20.5, 12,17)	0.9905

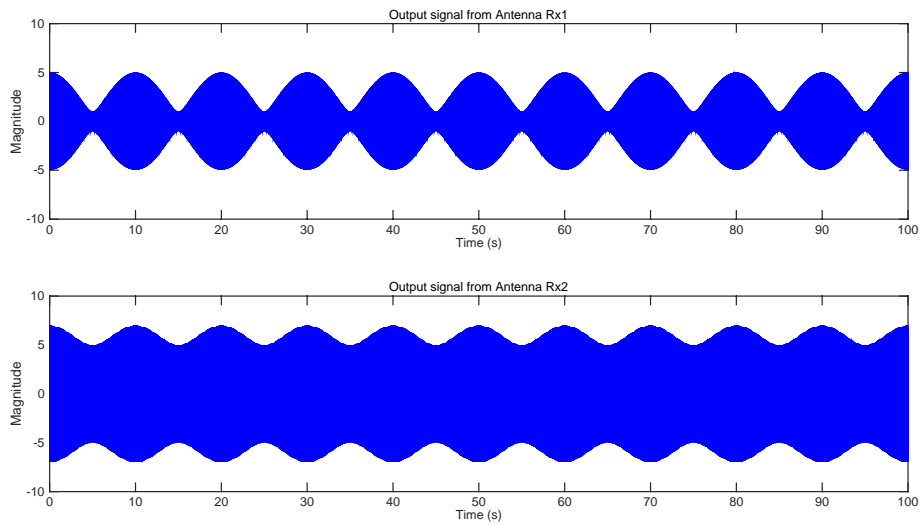


Figure 4.5 Output signal from Rx1 and Rx2 using random values for antennas magnitude responses combination ($M_{1E} = 2, M_{1F} = 3, M_{2E} = 6, M_{2F} = 1$) with identical phase delay.

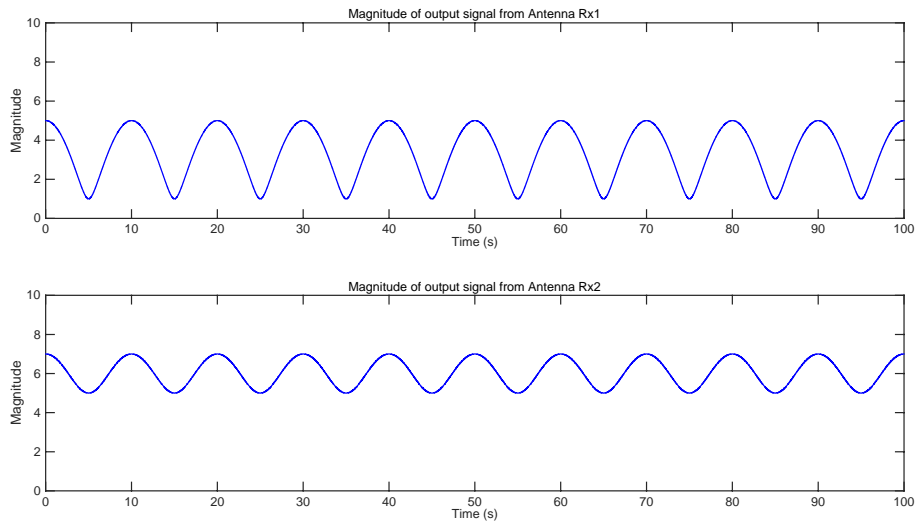


Figure 4.6 Amplitude of output signals from Rx1 and Rx2 using random values for antennas magnitude responses combination ($M_{1E} = 2, M_{1F} = 3, M_{2E} = 6, M_{2F} = 1$) with identical phase delay. The amplitude correlation coefficient between Rx1 and Rx2 is 0.99.

Table 4.2 Antenna phase response effect on correlation coefficients of amplitude of received signals. Random values are used for the phase response combination. The magnitude responses for these two antennas are set to be identical. All receiving antenna magnitude response is 1 for simplifying the simulation ($M_{1E} = M_{1F} = M_{2E} = M_{2F} = 1$).

$(P_{R_{1E}}, P_{R_{1F}}, P_{R_{2E}}, P_{R_{2F}})$ (Degree)	Phase difference difference (PDD) $P_{DD} = (P_{R_{1E}} - P_{R_{1F}}) - (P_{R_{2E}} - P_{R_{2F}})$ (Degree)	Correlation coefficient of received signals amplitude
(0,0,0,0)	0	1
(0,10,0,20)	10	0.98
(10,10,10,20)	10	0.98
(15,10,10,20)	15	0.96
(45, 0, 0,0)	45	0.67
(0, 45, 0,0)	-45	0.67
(90, 0, 0,0)	90	-0.04
(0, 90, 0,0)	-90	-0.04

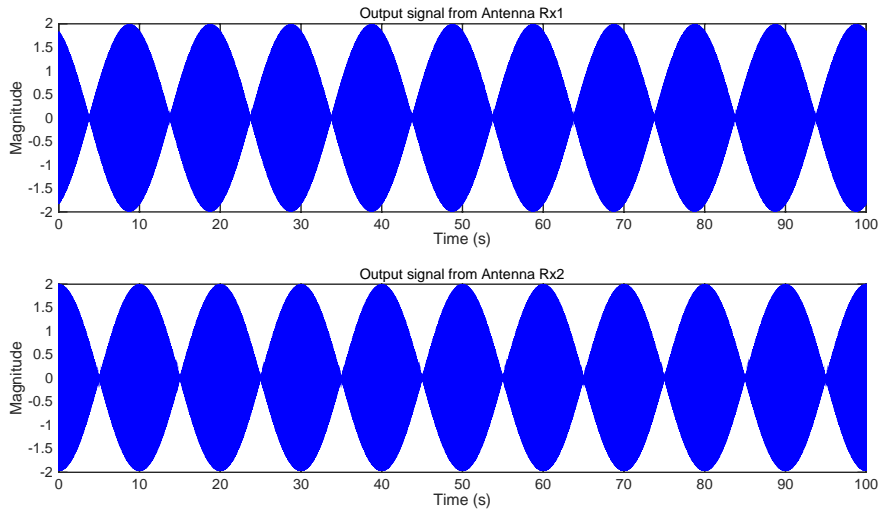


Figure 4.7 Output signal from Rx1 and Rx2 using random values for antennas phase responses combination ($P_{R_{1E}} = 0, P_{R_{1F}} = 45^\circ, P_{R_{2E}} = 0, P_{R_{2F}} = 0$) with identical magnitudes.

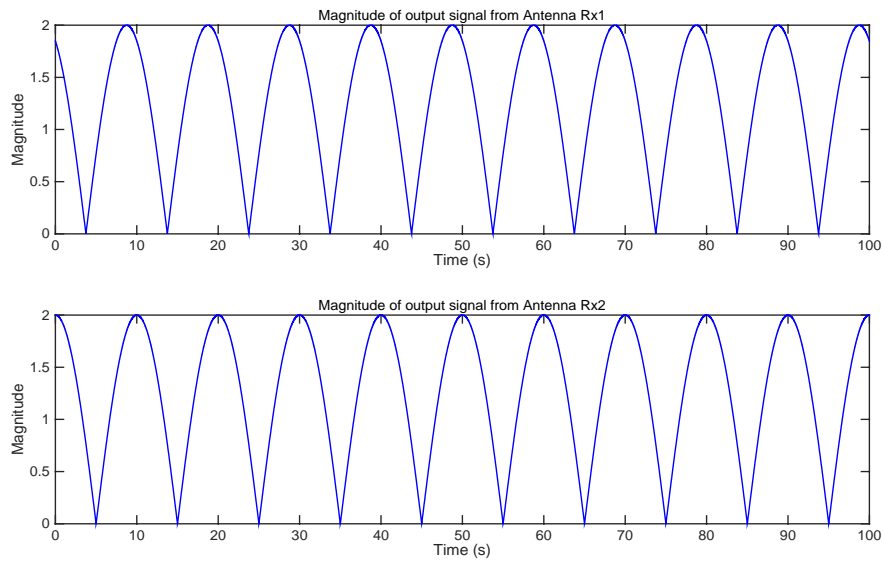


Figure 4.8 Amplitude of output signals from Rx1 and Rx2 using random values for antennas phase responses combination ($P_{R_{1E}} = 0, P_{R_{1F}} = 45^\circ, P_{R_{2E}} = 0, P_{R_{2F}} = 0$) with identical magnitude response. The amplitude correlation coefficient between Rx1 and Rx2 is 0.67.

Table 4.1 and 4.2 shows the magnitude and phase response diversity effect on the correlation coefficients of received signals. As the tables show, the correlation coefficient of received signals is more sensitive to different antenna phase responses. It is worth to notice that, the correlation coefficient will reduce rapidly with greater phase difference difference $P_{DD} = (P_{R_{1E}} - P_{R_{1F}}) - (P_{R_{2E}} - P_{R_{2F}})$. This is also suitable for transmitting antennas.

4.2.3 Phase difference difference (PDD) diversity

In order to get a better understanding of the antenna phase difference difference effect on received signal, antenna E-field phase information is needed. As the incident signals will be split into ordinary-wave (O mode) and extraordinary-wave (X mode) after reflection via ionosphere and one is left-hand polarization, the other is right-hand polarization. Finding the corresponding phase response of (\vec{E}_l, \vec{E}_r) for O and X incident signal becomes the key factor of modelling. Unfortunately, NEC-2 only provides \vec{E}_θ and \vec{E}_φ phase information instead of (\vec{E}_l, \vec{E}_r) (see Figure 4.4). In NEC coordinate system, the direction of \vec{E}_θ and \vec{E}_φ is the movement direction (tangent line) of the angles θ and φ respectively. And \vec{E}_θ is always perpendicular to \vec{E}_φ (see Figure 4.9). As a result, the transform from $(\vec{E}_\theta, \vec{E}_\varphi)$ to (\vec{E}_l, \vec{E}_r) become the first step of analysis.

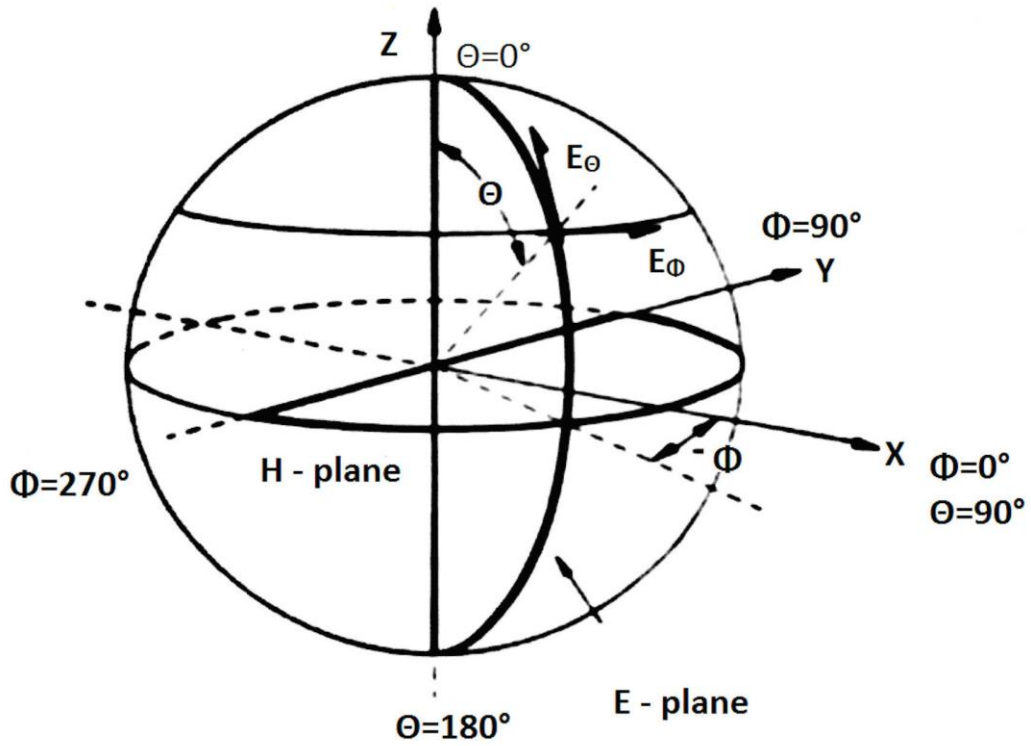


Figure 4.9 NEC-2 coordinate system

The real and imaginary part of \vec{E}_θ and \vec{E}_ϕ can be expressed as:

$$R_{\vec{E}_\theta} = M_\theta \times \cos P_\theta \quad \text{Real part of } \vec{E}_\theta \quad 4.6$$

$$I_{\vec{E}_\theta} = M_\theta \times \sin P_\theta \quad \text{Imaginary part of } \vec{E}_\theta \quad 4.7$$

$$R_{\vec{E}_\phi} = M_\phi \times \cos P_\phi \quad \text{Real part of } \vec{E}_\phi \quad 4.8$$

$$I_{\vec{E}_\phi} = M_\phi \times \sin P_\phi \quad \text{Imaginary part of } \vec{E}_\phi \quad 4.9$$

where M_θ and M_ϕ is the magnitude of \vec{E}_θ and \vec{E}_ϕ , respectively. P_θ and P_ϕ represents the phase of \vec{E}_θ and \vec{E}_ϕ , respectively. These four parameters can be obtained from NEC-2 standard output file.

Then the left and right circular polarization components can be deduced as:

Real part of left circular polarization component:

$$R_{\vec{E}_l} = 0.5 \times (R_{\vec{E}_\theta} + I_{\vec{E}_\varphi}) \quad 4.10$$

Imaginary part of left circular polarization component:

$$I_{\vec{E}_l} = 0.5 \times (I_{\vec{E}_\theta} - R_{\vec{E}_\varphi}) \quad 4.11$$

Real part of right circular polarization component:

$$R_{\vec{E}_r} = 0.5 \times (R_{\vec{E}_\theta} - I_{\vec{E}_\varphi}) \quad 4.12$$

Imaginary part of right circular polarization component:

$$I_{\vec{E}_r} = 0.5 \times (I_{\vec{E}_\theta} + R_{\vec{E}_\varphi}) \quad 4.13$$

Finally, the phase and magnitude of left and right circular polarization component can be deduced respectively as followed:

$$P_l = \tan^{-1}(I_{\vec{E}_l}/R_{\vec{E}_l}) \quad \text{Phase of left circular polarization component} \quad 4.14$$

$$P_r = \tan^{-1}(I_{\vec{E}_r}/R_{\vec{E}_r}) \quad \text{Phase of right circular polarization component} \quad 4.15$$

$$M_l = \sqrt{R_{\vec{E}_l}^2 + I_{\vec{E}_l}^2} \quad \text{Magnitude of left circular polarization component} \quad 4.16$$

$$M_r = \sqrt{R_{\vec{E}_r}^2 + I_{\vec{E}_r}^2} \quad \text{Magnitude of right circular polarization component} \quad 4.17$$

After the transform from $(\vec{E}_\theta, \vec{E}_\phi)$ to (\vec{E}_l, \vec{E}_r) , the magnitude and phase information of \vec{E}_l and \vec{E}_r can be obtained. Since the radio link distance is 202 km, once the reflection virtual height of signal can be confirmed, the angle of arrival of the incident wave can be deduced. Then the corresponding antenna responses including magnitude and phase information for O and X mode signal can be found. The virtual height of reflection can be obtained from ionogram produced by the UK Solar System Data Centre (Chilton station) (see Section 2.2.2).

4.2.4 Opposite expression in polarization

ITU defined that left-hand and right-hand polarized wave correspond to counter-clockwise and clockwise respectively, whilst looking in the direction of propagation [Radio Regulations, 2004]. NEC-2 takes the same definition for the polarization of a certain wave [Smith, 2008]. However, the ordinary wave (O mode) rotates with time in a left-hand and the extraordinary wave (X mode) rotates with time in a right-hand, when the thumb points in the direction of the magnetic field B [Davies, 1990]. As the opposite in the direction of thumb pointing, the X mode is expressed using left-hand polarization; the O mode is presented with right-hand polarization in the NEC-2 system. Experiments have been designed and carried out to verify this corresponding relationship in Chapter 7.

Chapter 5 Experimental set up

In order to investigate the correlation level of newly designed HF-band transmitting antenna arrays, several experimental campaigns have been conducted from June 2013 to July 2014. All the measurements were carried out over the 202 km radio link between Bruntingthorpe (52.49° N, 1.12° W) and Lancaster (54.00° N, 2.79° W).

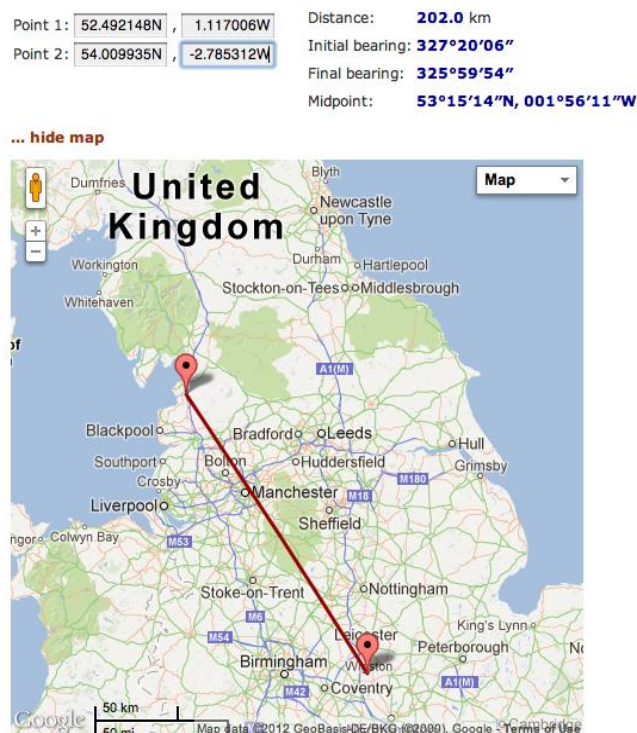


Figure 5.1 Bruntingthorpe-Lancaster HF radio link

5.1 Transmitting System

The transmitting system located at Bruntingthorpe consisted of four individual transmitters with a 250 W amplifier for each. The Racal MA3752 dual HF drive

unit was employed as the transmitter, which can generate USB, LSB, AM and CW signals with the frequency from 1.5 MHz to 40 MHz with minimum 1 Hz step. Continuous wave (CW) was employed for all the measurements with a selection of licensed frequencies depending on the ionosphere condition. Ionograms were obtained from UK Solar System Data Centre (UKSSDC) website, using Chilton ionosonde station investigation results, which is continuously updated every 10 minutes.



Figure 5.2 Racal transmitters and amplifiers

5.2 Receiving System

5.2.1 Receiving antenna

A wide band dipole antenna FWB/2530 (see Figure 5.3), which located on the roof of the Department of Engineering building, Lancaster University, was used as the receiving antenna for the early two experimental measurements. A 5 m high RX-5000 HF whip antenna (see Figure 5.4) was employed at the receiving end for the later experiments, which was built at Hazelrigg field site near Lancaster University.

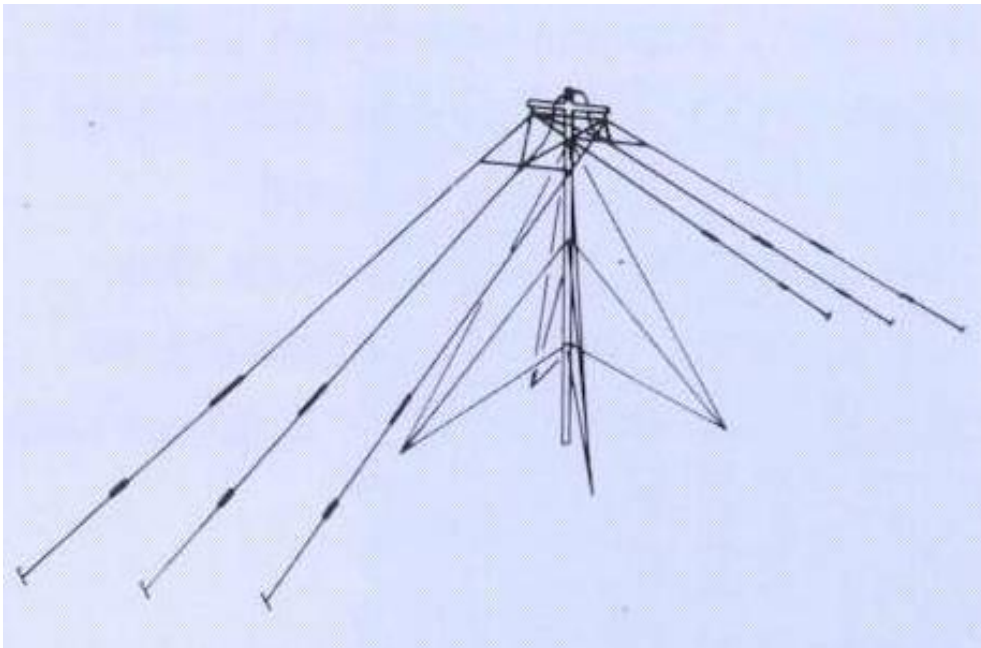


Figure 5.3 FWB 2530 wide band HF dipole antenna



Figure 5.4 Whip antenna at the Lancaster receiving site

5.2.2 Perseus software defined radio (SDR) receiving system

Perseus is a software defined radio receiver with operating frequency band from VLF to HF. There are two ports in the receiver: one port was connected to the 5m high whip-receiving antenna via 50 ohm coaxial cable, while the other port was connected to the computer using a high-speed 480 Mbits/s USB 2.0 cable. The received data, including header information (frame size, sample rate, receiver frequency, time etc), was stored in the computer hard disk. The received signals can be recovered from processed data files using Matlab.



Figure 5.5 Data receiving equipment

5.3 Experimental arrangement

Seven experimental campaigns have been conducted since 2013. The related experiment arrangement details are showed in the following table. All these measurements were carried out between Bruntingthorpe (Tx) and Lancaster (Rx).

Table 5.1 Experimental arrangement table

Experiment time (GMT)	Transmitter antenna array type	Receiver antenna type	Transmission frequency (MHz)
27/06/13 11:46-13:16	T1 and ORG	Wide band dipole	6.780
03/07/13 15:01-16:20	T2 and ORG	Wide band dipole	6.780
08/10/13 11:40-12:40	Ex-T2 and T2	Whip antenna	9.040
14/04/14 14:10-15:50	Ex-ORG and ORG	Whip antenna	8.100
10/07/14 14:00-15:00	E2 and ORG	Whip antenna	6.780
16/07/14 09:20-10:30	S2 and ORG	Whip antenna	6.780
31/07/14 14:40-16:00	NPT and ORG	Whip antenna	6.780

Chapter 6 Summary and modelling of previous experiments

Previous experimental measurements conducted by Gunashekar et al. [2009a, 2009b, 2010] indicated that the collocated crossed End-Fed Vee antenna array (ORG) had a useful level of decorrelation between array elements. Two previous campaigns using broadband HF End-Fed Vee antenna array at the transmitting and receiving end will be introduced, respectively. Furthermore, the modelling results and analysis for this antenna array, using CocoaNEC, will be displayed and explained in this chapter as well.

6.1 Experiment 1: Crossed End-Fed Vee array performance at the transmitter

6.1.1 Experimental Arrangement

A 2×8 MIMO measurement was carried out between Durham (tx) and Bruntingthorpe (rx) on 19 June 2009. At the transmitter, a collocated crossed End-Fed Vee wire antenna array was employed (see Figure 6.1). A balun and balancing network (300 ohm resistance) were located at opposite ends of the antennas. An approximately 8 m mast was employed to support the array at the crossed point. One of the pair (TX-2) was arranged to point to the receiver at Bruntingthorpe. The other antenna (TX-1) was perpendicular to TX-2. Each antenna was made of stainless steel wire (about 34 m).

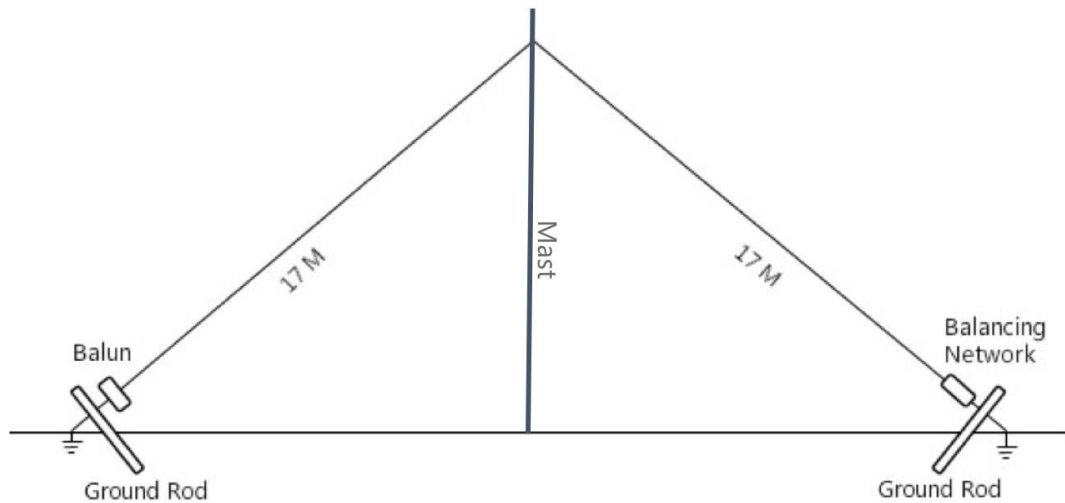


Figure 6.1 Construction of end-fed Vee antenna. The array (ORG) is composed by two identical orthogonally oriented end-fed Vee antennas.

At the receiving end, three antenna arrays were deployed in a line in the east-west direction: a crossed end-fed Vee array identical to that employed at the transmitting end (RX-1: The N-S arm of the array; RX-2: The E-W arm of the array), the ground symmetric loop 'GSL' antenna array mentioned in Section 3.4 (see Figure 3.9) (RX-3: GSL loop-1; RX-4: GSL loop-2; RX-5: GSL loop-3), the 'X-Y-Z' array (see Figure 3.8) (RX-6: vertical loop in N-S orientation; RX-7: vertical loop in E-W orientation; RX-8: vertical loop in horizontal orientation). The separations between the three array supporting masts were 32.2 m and 37.2 m, respectively.

6.1.2 Results and Discussion

The measurement was conducted for nearly 45 min (from 1135 UT to 1220 UT) with nominal transmission frequency 5.255 MHz. In order to identify different transmit signals, the frequencies were offset by 10 Hz (TX-1: 5.255020 MHz; TX-2: 5.255030 MHz). CW signals were simultaneously transmitted using the crossed end-fed Vee array with nominal transmit power of approximately 50 W on each antenna. 35 one-minute data files were collected for each of the receiving antennas.

Sufficiently low levels of correlation between antenna array elements is a key requirement for successfully implementing a MIMO system. Furthermore, Waldschmidt [2002] reports that signals are generally considered as independent when the correlation coefficients values are below 0.7. Besides, MIMO channel capacity does not decrease obviously if antenna array elements correlation level is under 0.9 [Loyka, 2001].

In order to investigate the correlation level between transmit antenna array elements, the occurrence frequency histograms of one minute received signal amplitude correlation coefficients by employing 'crossed end-fed Vee array', 'GSL array', 'X-Y-Z array' are depicted in Figure 6.2, 6.3 and 6.4, respectively.

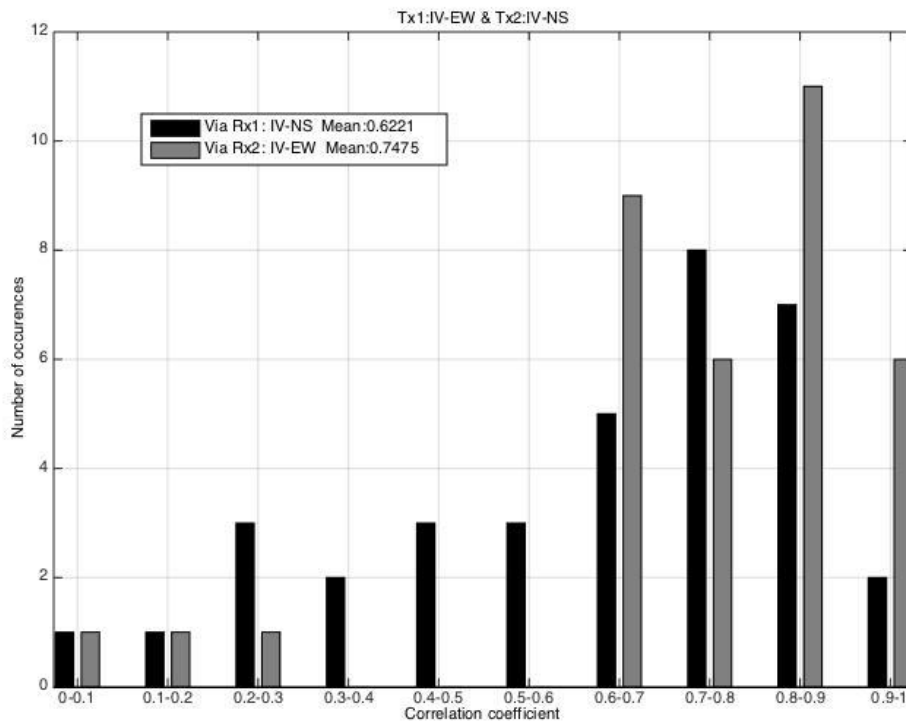


Figure 6.2 The occurrence frequency histograms of the one minute received signal amplitudes of correlation coefficients between crossed inverted end-fed Vee array elements at the transmitter (Durham), investigated via the identical end-fed Vee array at the receiver (Bruntingthorpe). The 2×8 MIMO measurement was carried out on 19 June 2009 with nominal transmission frequency 5.255 MHz. 35 one-minute data files were collected and analysed.

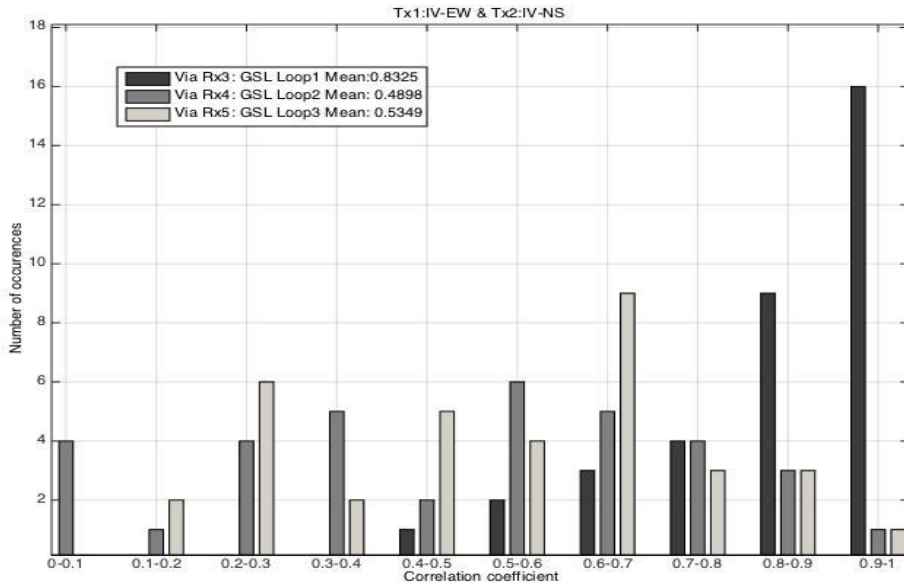


Figure 6.3 The correlation coefficients between transmitting antennas investigated via GSL array at the receiver (Bruntingthorpe).

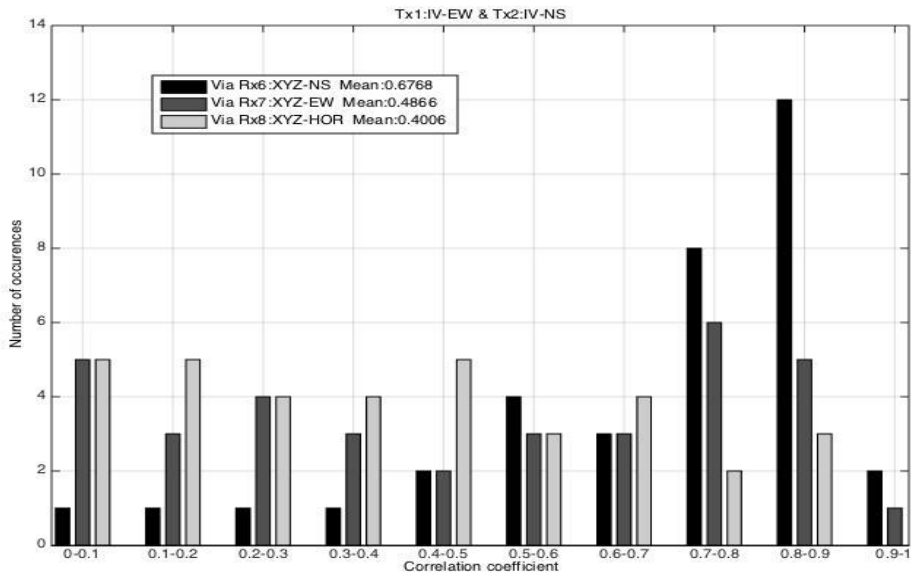


Figure 6.4 The correlation coefficients between transmitting antennas investigated via X-Y-Z array at the receiver (Bruntingthorpe).

The mean values of the amplitude correlation coefficients between crossed end-fed Vee antenna array elements at transmitting end, investigated via eight different receiving antennas, are displayed in Table 6.1. The collocated end-fed Vee antenna array, as a transmitting antenna array, showed a useful decorrelation level between the array elements: the maximum mean value of amplitude correlation coefficients is 0.83 (investigated via GSL-1 antenna). However, this numerical value is only 0.49 and 0.52, investigated via GSL-2 and GSL-3 antennas, respectively, which is collocated with GSL-1 antenna. The minimum mean value of correlation coefficients is 0.40, which is showed on the horizontal component of 'X-Y-Z array'. Specifically, the 'XYZ-HOR' antenna shows that all the correlation coefficient values are less than 0.9 and approximately 86% of the corresponding values do not exceed 0.7.

Table 6.1 Mean values (35 one minute data files) of the amplitude correlation coefficients between the collocated N-S and E-W oriented end-fed Vee long wire antennas at each of the receiving antennas for a 2×8 HF-MIMO experimental measurement carried out between Durham and Bruntingthorpe on 19 June 2009.

Receiving antenna	Mean correlation coefficient between collocated N-S and E-W Transmitting end-fed Vee antennas
Rx-1: N-S arm of end-fed Vee array	0.62
Rx-2: E-W arm of end-fed Vee array	0.75
Rx-3: GSL array Loop-1	0.83
Rx-4: GSL array Loop-2	0.49
Rx-5: GSL array Loop-3	0.53
Rx-6: X-Y-Z array N-S loop	0.68
Rx-7: X-Y-Z array E-W loop	0.49
Rx-8: X-Y-Z array horizontal loop	0.40

6.2 Experiment 2: Crossed end-fed Vee array performance at the receiver

6.2.1 Experimental Arrangement

A 4×8 MIMO link was established on 26 March 2009. Two pairs of collocated antenna arrays were set up at transmitter end (Durham): the collocated end-fed Vee antenna array, which was identical to the one described in Section 6.1.1, was employed in the campaign (TX-1: N-S oriented end-fed Vee wire antenna; TX-2: E-W oriented end-fed Vee wire antenna). In addition, a pair of collocated perpendicular dual octagonal loop array (see Figure 6.5) was utilized at the transmitter (TX-3: N-S oriented octagonal loop; TX-4: E-W oriented octagonal loop). 4.455 MHz was employed as the nominal transmission frequency and 10 Hz was selected as the frequency offset in order to identify transmitter antennas (TX-1: 4.455020 MHz; TX-2: 4.455030 MHz; TX-3: 4.455010 MHz; TX-4: 4.455040 MHz). The output power was approximately 50 W for each antenna, which was identical to the campaign in Section 6.1.



Figure 6.5 Dual perpendicular octagonal loop transmitter antenna array

At the receiver, in addition to the crossed end-fed Vee array (RX-1: N-S oriented end-fed Vee wire antenna; RX-2: E-W oriented end-fed Vee wire antenna) and ‘X-Y-Z’ active array (RX-6: N-S vertical loop; RX-7: E-W vertical loop; RX-8: horizontal loop), which were identical to the arrays in Section 6.1, a crossed dipole and vertical monopole array (see Figure 6.6) (RX-3: N-S crossed dipole; RX-4: E-W crossed dipole; RX-5: vertical monopole) was also utilized.



Figure 6.6 Crossed dipole with single monopole receiver antenna array

6.2.2 Results and Discussion

The campaign was carried out from 1348 UT to 1456 UT. 52 one-minute data files were collected at each of the receiving antennas. In order to investigate the correlation level between end-fed Vee array elements at receiver, the occurrence frequency histograms of magnitude correlation coefficients between the N-S oriented (RX-1) and E-W oriented (RX-2) end-fed Vee wire antennas, via four transmitting antennas, are displayed in Figure 6.7.

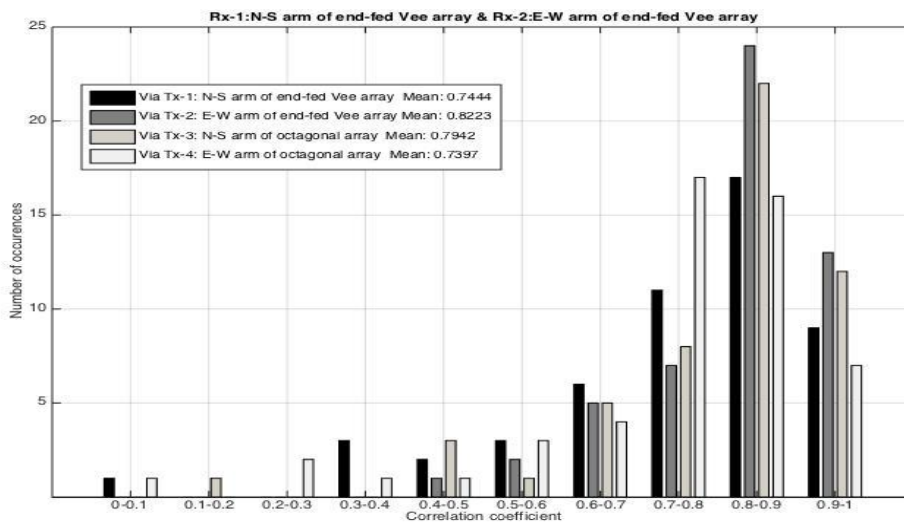


Figure 6.7 The occurrence frequency histograms of the one minute received signal amplitudes of correlation coefficients between crossed inverted end-fed Vee array elements at the receiver (Bruntingthorpe), investigated via four different antennas at the transmitter (Durham). The 4×8 MIMO measurement was carried out on 26 March 2009 with nominal transmission frequency 4.455 MHz. 52 one-minute data files were collected and analysed.

Figure 6.7 shows that majority of the amplitude correlation coefficients values via all four transmitting antennas lie in the range 0.6-1.0 for the crossed end-fed Vee antenna array at the receiver under the prevailing ionospheric conditions. The maximum mean value of the correlation coefficients of the end-fed Vee array is 0.82, showed on the E-W oriented end-fed Vee transmitting antenna. The minimum corresponding value is 0.74, by using the signal from the E-W oriented vertical octagonal loop antenna.

The campaign indicates that the correlation level of the crossed end-fed Vee antenna array lies in the range of approximately 0.70-0.85 when the array is utilized at the receiver to pick up 4.455 MHz signals. Another experimental measurement conducted by Gunashekar [2010] also shows that, by receiving 5.255 MHz signals, the mean values of correlation coefficients of the array are in an identical range.

6.3 Traditional collocated end-fed Vee antenna array modelling and analysis

Since the collocated crossed end-fed Vee antenna array (ORG) showed a useful decorrelation level between array elements both at transmitting and receiving end in the previous campaigns, the modelling for this array has been carried out employing 'CocoaNEC' and the phase difference difference calculated based on the assumption in Section 3.4.

The ORG array consists of two collocated end-fed Vee wire antennas, which are 34m long (see Figure 6.8). These two broadband antennas can be operated over the whole HF band. A balun and balancing network (300 ohm resistance) is located at opposite ends of the antennas. A 7.3 m mast is employed to support the array at the crossed point. There is 10cm spacing between the tops of the array elements.

In later campaigns, the ORG array was used as the reference antenna array (see Chapter 7). One of the pair (ORG-Lan) was arranged to point to Lancaster, which was built towards the direction of transmission (along the X-axis in the modelling).

The other antenna (ORG-Cross) was perpendicular to the previous antenna (along the Y-axis in the modelling). In order to correspond to later experiments, the antenna array is modelled at 6.780 MHz with average ground condition (dielectric constant: 13.0, conductivity: 0.005 Sm^{-1}). It is divided into 171 segments (0.1 m/segment) for each side of the antennas, and AWG #14 (0.8140 mm) is used for the antenna wire radius. The radius of the mast is set to be 25 mm. Power sources and resistances are supported by four short vertical wires (0.1 m), which are employed to connect the main structure of the antenna and ground plane. As the goal is antenna phase difference difference, an arbitrary excitation of 1 V is selected. The antennas are run separately by using the excitation only for the desired output. The 2D radiation pattern of elevation and azimuth for ORG-Lan and ORG-Cross is shown in Figures 6.9 and 6.10 respectively. 3D radiation pattern for these two antennas are presented in Figures 6.11 and 6.12.

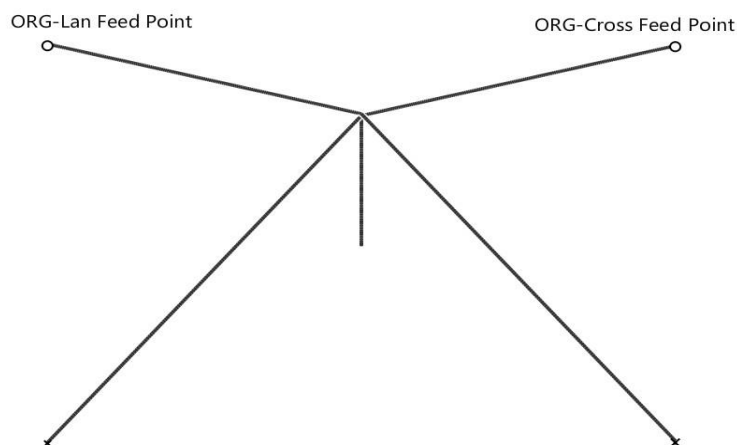


Figure 6.8 Collocated crossed end-fed Vee array (ORG)

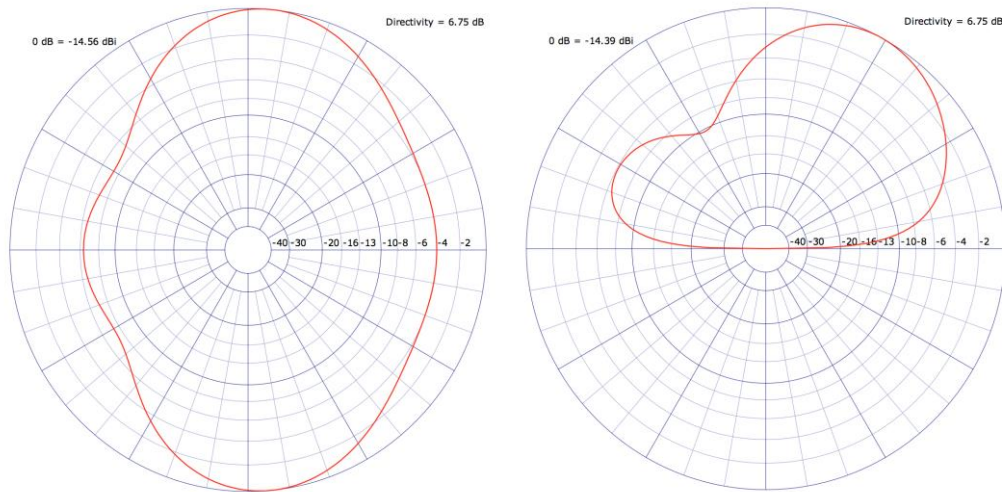


Figure 6.9 Radiation pattern produced by original crossed end-fed Vee array element points to Lancaster (ORG-Lan) at 6.780 MHz, Azimuth-plot (left) and Elevation-plot (right).

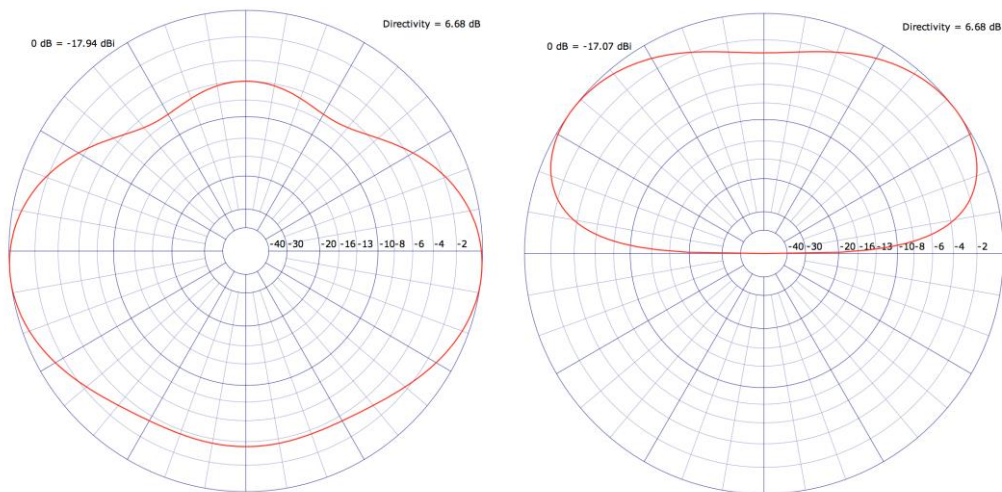


Figure 6.10 Radiation pattern produced by original crossed end-fed Vee array element perpendicular to Lancaster (ORG-Cross) at 6.780 MHz, Azimuth-plot (left) and Elevation-plot (right).

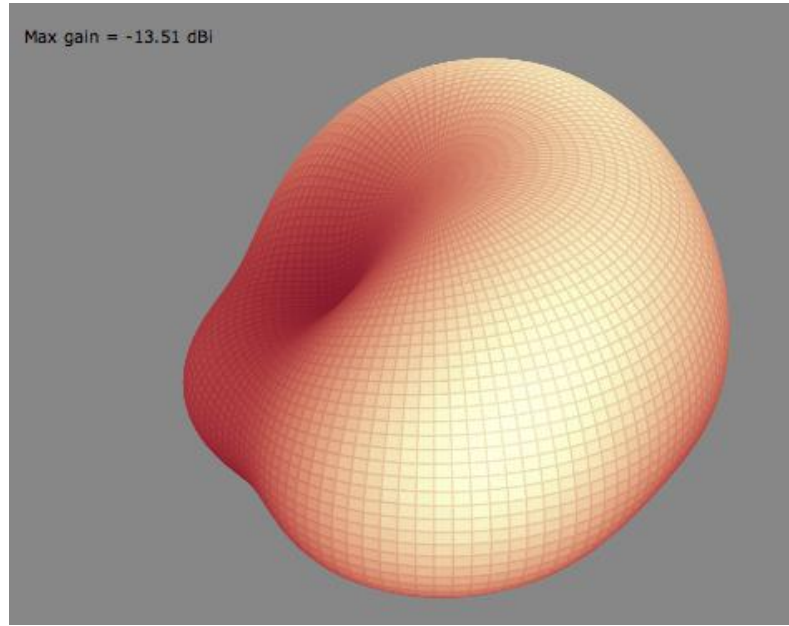


Figure 6.11 3D Radiation pattern produced by original crossed end-fed Vee array element points to Lancaster (ORG-Lan) at 6.780 MHz

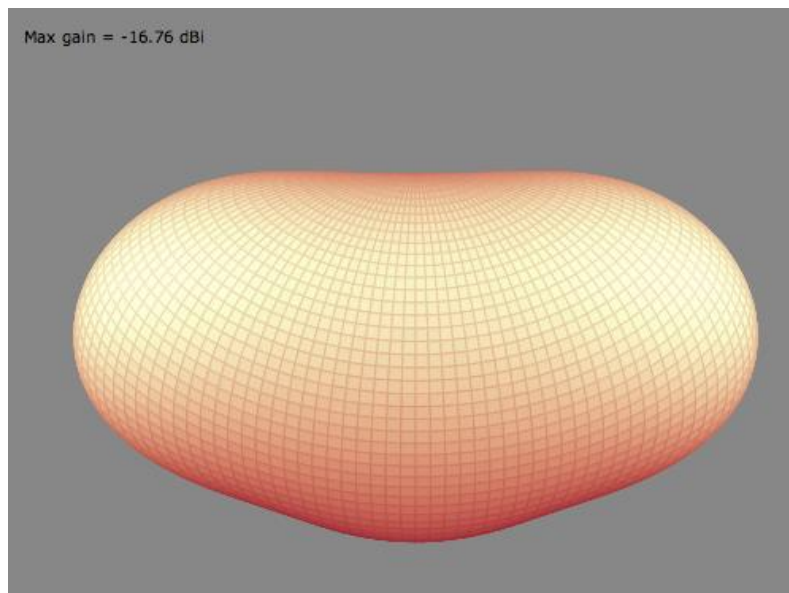


Figure 6.12 3D Radiation pattern produced by original crossed end-fed Vee array element perpendicular to Lancaster (ORG-Cross) at 6.780 MHz

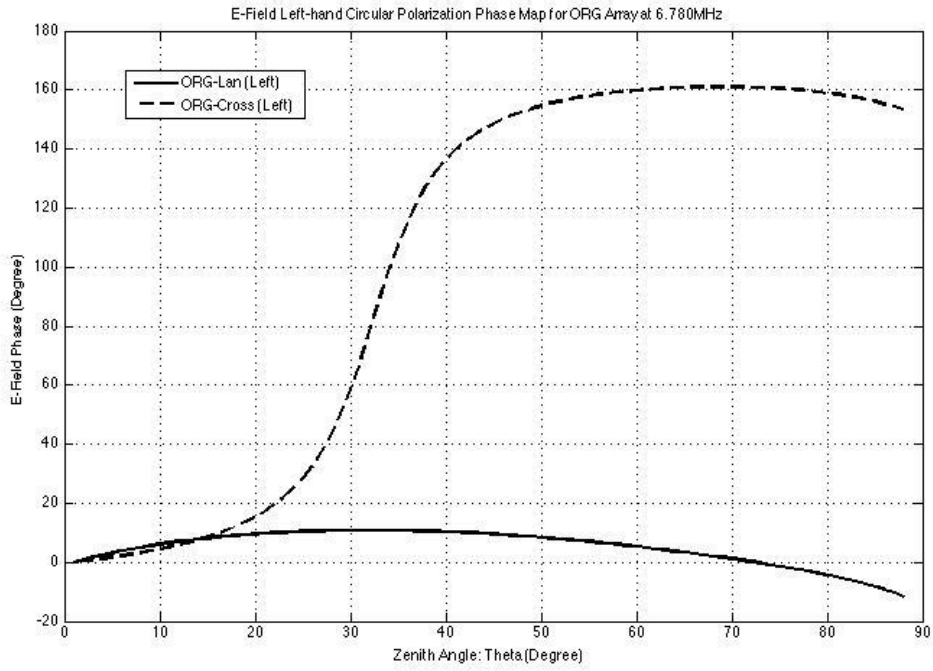


Figure 6.13 ORG array left-hand circular polarization phase map at 6.780 MHz

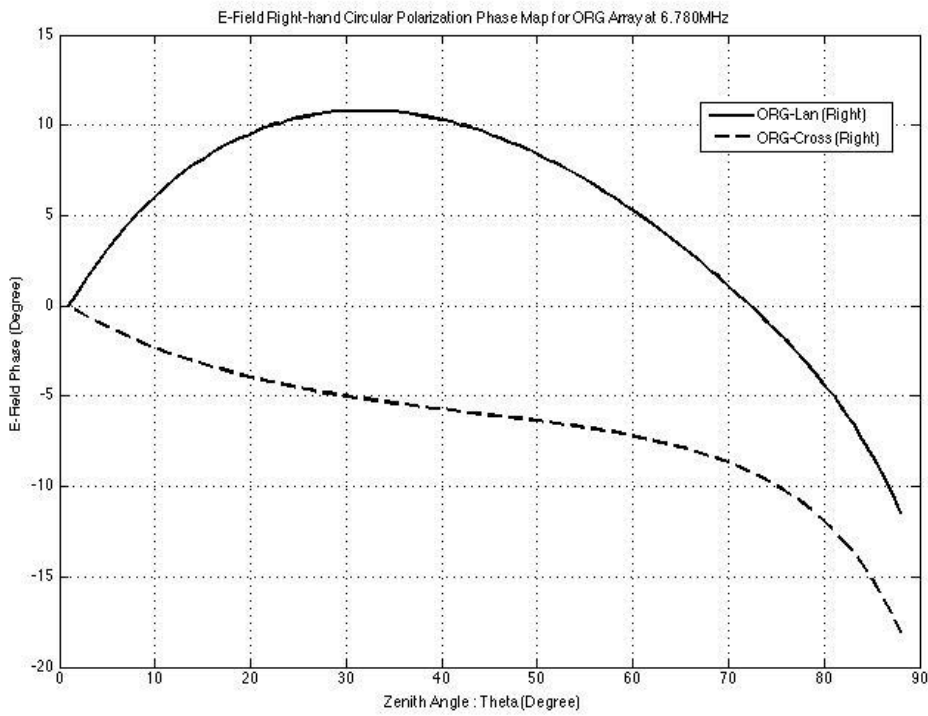


Figure 6.14 ORG array right-hand circular polarization phase map at 6.780 MHz

Figure 6.13 and 6.14 shows the ORG array phase response for left and right hand polarization incident waves respectively. As the new radio link (between Bruntingthorpe and Lancaster) is about 202 km, by considering the signals' virtual reflection height, the zenith angles found during the experimental is between 5° to 20° . Therefore, a zenith angle 14° and 7° is used as the angle of arrival for 1-hop and 2-hop signal in the prediction modelling. For the left-hand polarization incident waves (X mode), the ORG array can only provide 1.5° phase difference difference (see Figure 6.13); for the right-hand polarization incident waves (O mode), the phase difference difference provide by the array is 4.8° (see Figure 6.14). New antenna arrays designed to have more phase difference difference than the ORG array both in O and X mode, and to show a lower level of correlation between array elements in experimental measurements are discussed in Chapter 7.

Chapter 7 Modelling of novel antenna arrays and measurements

Since the collocated crossed end-fed Vee antenna array (ORG) showed a useful decorrelation level in the previous experimental measurements, the array is utilized as the reference antenna array in the following modelling and campaigns. In order to prove the PDD diversity assumption in Section 4.2, several novel antenna arrays evolved from the ORG array are modelled and tested in this chapter. All these novel antenna arrays aimed to obtain greater phase difference difference (PDD) than the ORG array. Then these novel antenna arrays were built at Bruntingthorpe and tested with referenced antenna array via a 202 km radio link to Lancaster.

The modelling work showed that all these newly designed novel antenna arrays can produce greater PDD than ORG array and the experimental measurements results indicated that these novel antenna arrays were more decorrelated than ORG array. The modelling for these novel antenna arrays (including radiation patterns, phase maps and predicted PDD etc.) are presented in Section 7.1. Experimental arrangements and results are described in Section 7.2. A summary and discussion are in Section 7.3.

7.1 Novel antenna arrays modelling

7.1.1 Antenna Array T1 Modelling

The newly designed antenna array T1 has the identical basic structure to the ORG array, except that, 6 vertical elements made by stainless steel wire are added on each antenna (see Figure 7.1). These components are spaced apart by $1/8$ of the antenna length and connect the antenna with ground. The antenna array is modelled at 6.780 MHz with average ground conditions (dielectric constant: 13.0, conductivity: 0.005 Sm^{-1}). The power source and balancing network is the same as for the ORG array. The 2D azimuth and elevation of radiation patterns and 3D radiation pattern produced by the array T1 are displayed in Appendix 1.

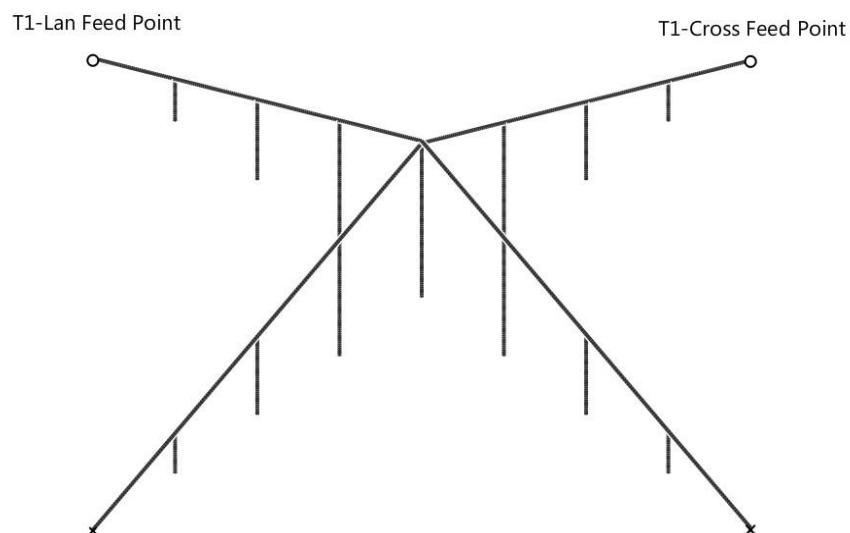


Figure 7.1 Collocated crossed end-fed Vee array T1

It is noteworthy that the radiation patterns of the newly designed array T1 is significantly different to the ORG array (see Figure 6.9 and Figure 6.10). Both the magnitude and phase response has been changed for the incident waves. Figure 7.2 and 7.3 show the array T1 left-hand and right-hand E-field phase response changing with zenith angle using ORG as referenced array, respectively. The phase change for the array T1 is greater than the ORG array for the range of zenith angles relevant to the experiment (5° - 20°).

By using 14° and 7° as incident zenith angle (θ) for 1-hop and 2-hop signal in the prediction model, it can be deduced that: for the X mode incident waves (left-hand polarization in NEC-2 system), array T1 can provide 7.5° PDD which is significantly higher than 1.5° given by ORG array; for the O mode incident waves (right-hand polarization in NEC-2 system), PDD for array T1 is 10.4° , which is also greater than ORG array (4.8°). Greater PDD means that the newly designed collocated antenna array T1 can provide more decorrelated signals at the receiving end compared with traditional crossed end-fed Vee array (ORG) in both O and X mode. The experimental correlation level measurement using T1 and ORG as the transmitting arrays will be discussed in Section 7.2.1.

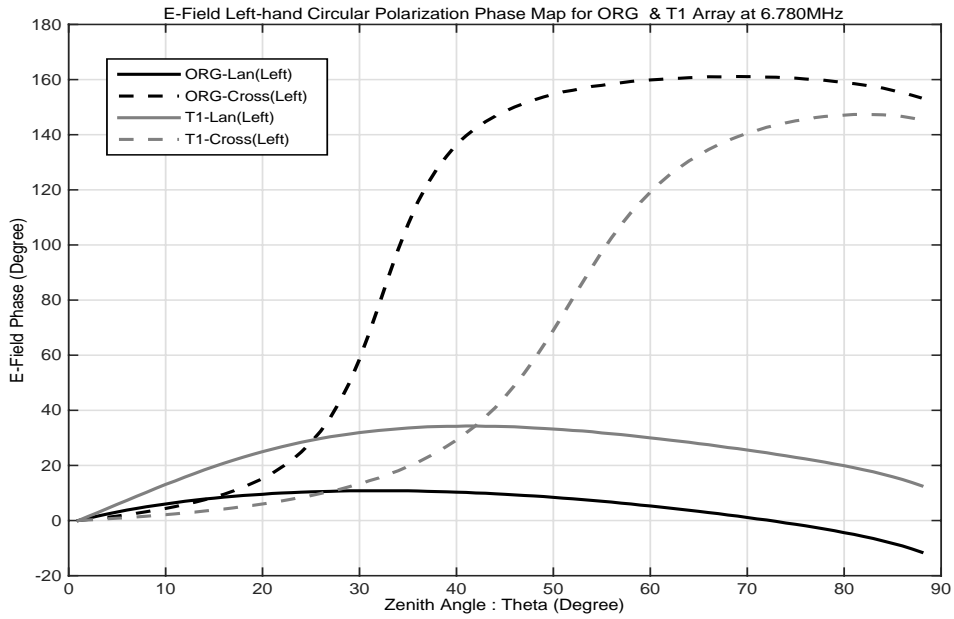


Figure 7.2 Left-hand circular polarization phase response map of T1 and ORG array at 6.780 MHz

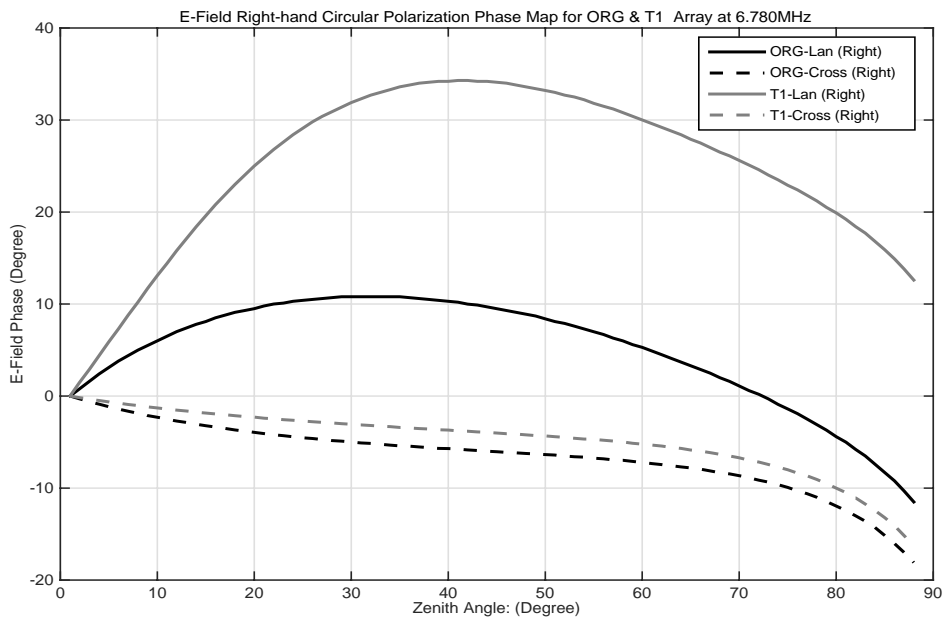


Figure 7.3 Right-hand circular polarization phase response map of T1 and ORG array at 6.780 MHz

7.1.2 Antenna Array T2 Modelling

Since the radiation patterns of ORG and T1 array have a significantly difference, a new antenna array T2 was designed to make these two different radiation patterns together to investigate the effect on the received signals. T2 is consisted by 'T1-Cross' antenna and 'ORG-Lan' antenna (see Figure 7.4). The 2D and 3D radiation patterns are displayed in Appendix 2.

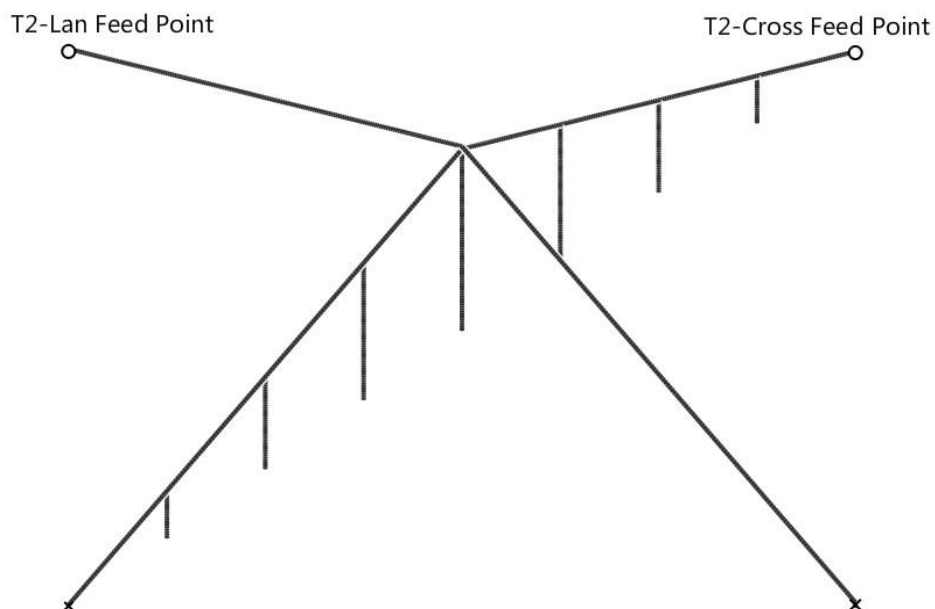


Figure 7.4 Construction of T2 antenna array. The array element pointing to Lancaster is a 34 m end-fed Vee broadband antenna, which is identical with 'ORG-Lan' antenna. The perpendicular antenna is same with 'T1-Cross' antenna, which has 6 wire elements connected with ground. A 7.3 m antenna mast is employed to support the array.

Figure 7.5 and 7.6 shows the T2 and ORG array phase response for left-hand and right-hand polarized incident waves respectively. For X mode, as showed in the Figure 7.5, the phase changing of the newly designed array T2 is greater than the ORG array in the zenith angle interval of 5-20°. According to prediction model, T2 array can provide a PDD of 4.4° for left-hand polarization between 1-hop (Zenith angle: 14°) and 2-hop (Zenith angle: 7°) signals, which is bigger than -1.5° given by the ORG array. For O mode, it can be deduced that T2 array has a PDD of 5.6° for right-hand polarization (the ORG array can provide a PDD of 4.8° for O mode). As a result, the newly designed array T2 can provide more phase difference difference for zenith angles less than 20°. Experimentally, the signals sent by T2 array can be more decorrelated at the receiving end compared with the ORG array (see Section 7.2.2).

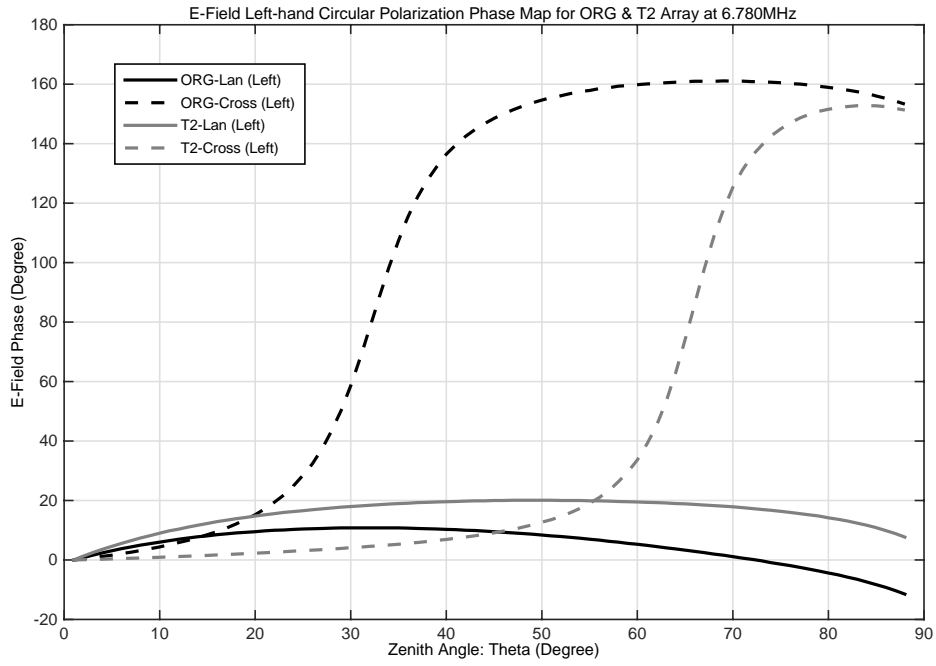


Figure 7.5 Left-hand circular polarization phase response map of T2 and ORG array at 6.780 MHz

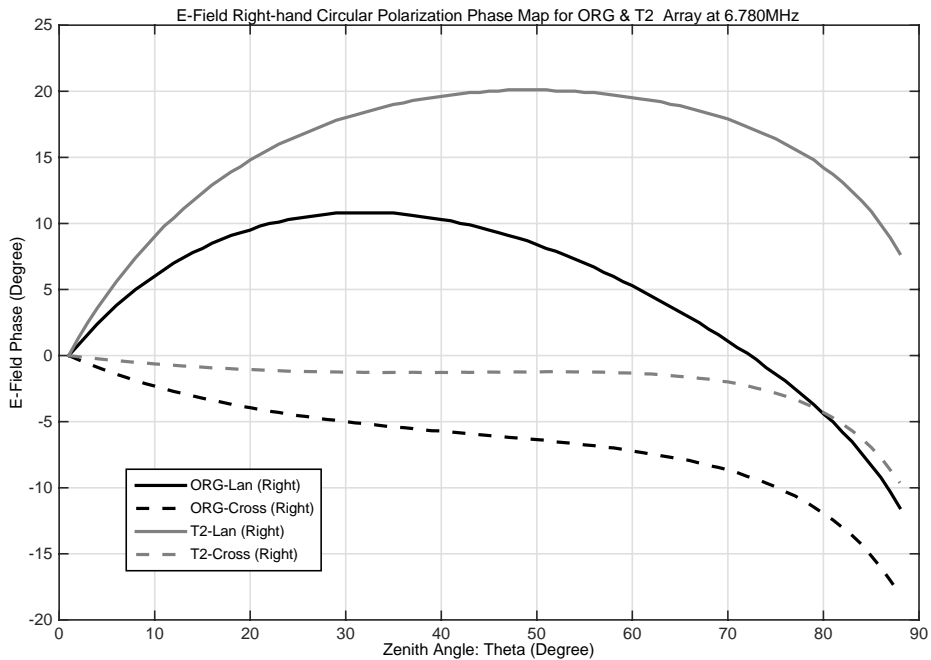


Figure 7.6 Right-hand circular polarization phase response map of T2 and ORG array at 6.780 MHz

7.1.3 Antenna array Ex-ORG and Ex-T2 Modelling

In order to investigate the power source location effect on antenna phase, the Ex-ORG and Ex-T2 array were designed. Ex-ORG keeps the same antenna array structure as the ORG array with the only difference being the location of the feed point for the antenna, which is perpendicular to the direction of Lancaster (see Figure 7.7). The correlation level of the antenna array elements under a single mode (X mode), at 8.100 MHz and 9.040 MHz is investigated. The 2D radiation patterns of ORG and Ex-ORG are displayed in Appendix 3. The 3D radiation patterns of the arrays are shown in Figure 7.8.

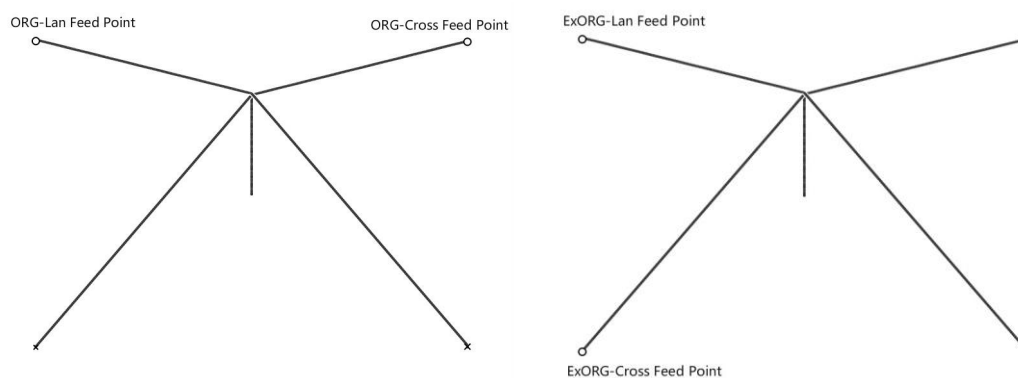


Figure 7.7 The structure of ORG (Left) and Ex-ORG (Right) array. The only difference between these two arrays is the opposite location of the feed point for the crossed antenna. The modelling frequency is 8.100 MHz for these two arrays.

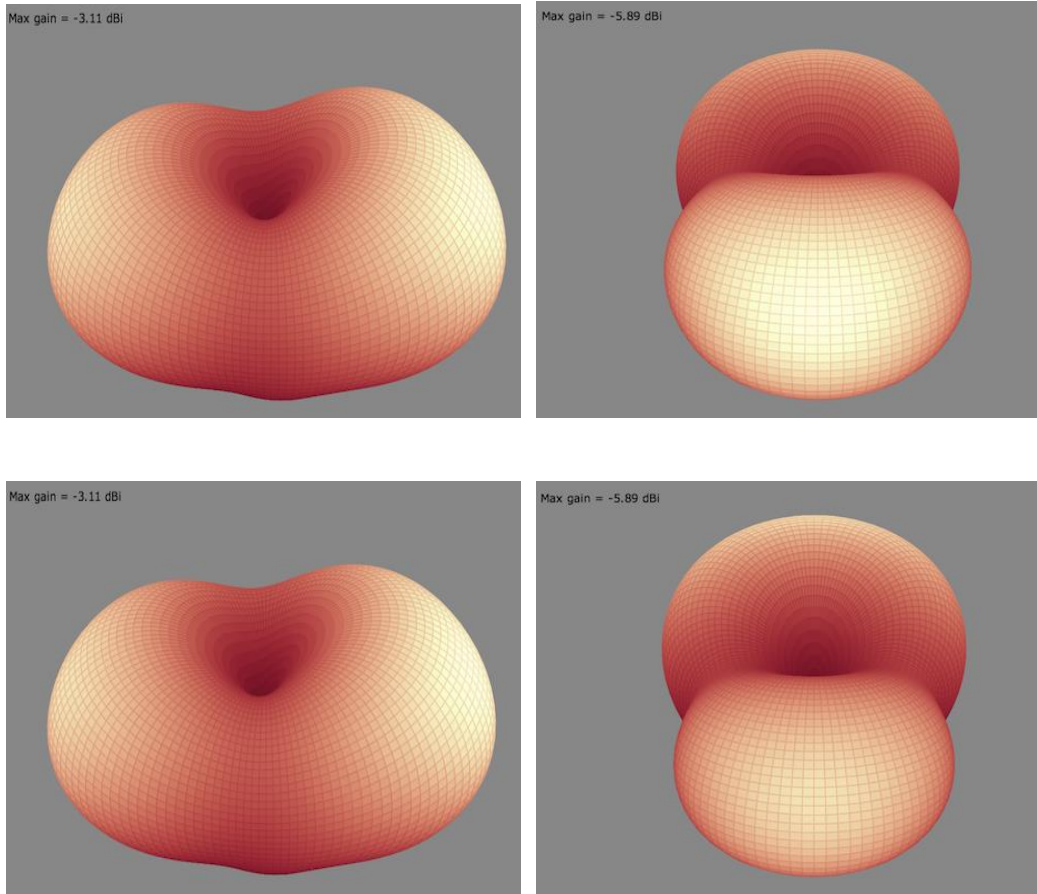


Figure 7.8 3D radiation pattern (modelling at 8.100 MHz) for ORG-Lan (Left-top), ORG-Cross (Right-top), ExORG-Lan (Left-bottom), ExORG-Cross (Right-bottom), respectively.

The radiation pattern is identical for the antenna ORG-Lan and ExORG-Lan. This can be found both in 2D and 3D (see Figure 7.8 Left-top and Left-bottom) pattern. For the antenna ORG-Cross and ExORG-Cross, due to the opposite location of the feed point, the radiation pattern is exchanged for these two antennas (see Figure 7.8 Right-top and Right-bottom). The phase responses of these two antenna arrays are displayed in Figure 7.9.

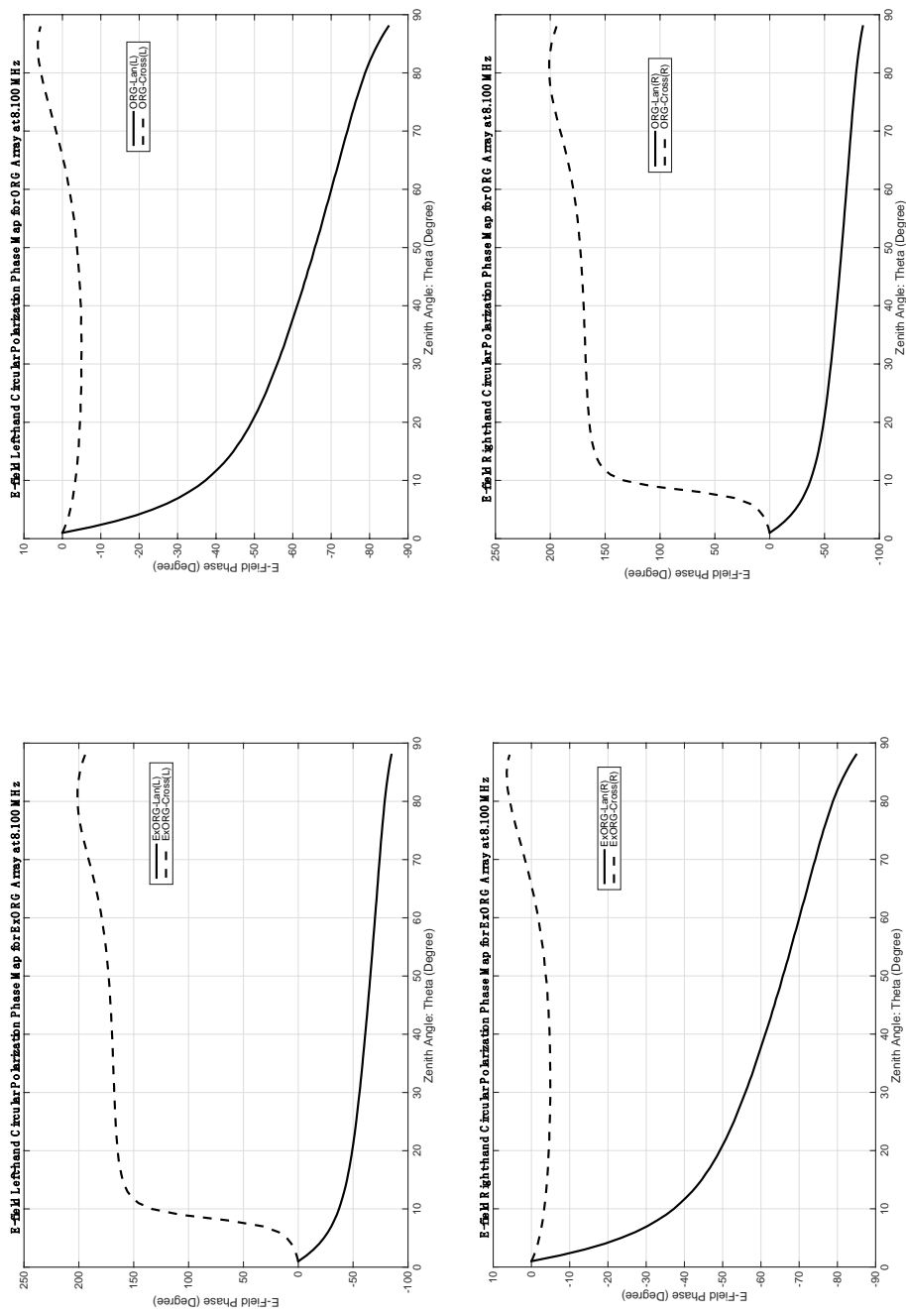


Figure 7.9 E-field left and right hand polarised phase map for the antenna array ORG and ExORG at modelling frequency 8.100 MHz (ExORG-left: Right-top; ORG-left: Right-top; ExORG-right: Right-bottom). The left hand phase of ORG is identical with right hand phase of ExORG (vice versa) in case that the feed points for the crossed antennas are inverted.

Again, the T2 and Ex-T2 array differ only with opposite feed point for the antenna perpendicular to the direction of transmission (see Figure 7.10). The 2D radiation patterns of T2 and ExT2 array with modelling frequency 9.040 MHz are displayed in Appendix 3. 3D radiation patterns are displayed in Figure 7.11. The radiation pattern keeps same for the antennas pointing to Lancaster. For the antennas perpendicular to the transmission direction, the radiation pattern is exchanged due to the opposite feed point. Figure 7.12 displays the phase response of T2 and ExT2 for O and X mode incident waves. The left-hand polarization phase of T2 is identical with the right-hand polarization phase of ExT2, vice versa.

It is worth to notice that: both 'ORG and ExORG' and 'T2 and ExT2' provide the same PDD, but the polarization is exchanged. The single X mode incident wave can be obtained if the experiment is carried out using higher frequency (8.100 MHz and 9.040 MHz) under a certain ionosphere condition. As a result, the effect of single polarized phase difference on the correlation level of received signals can be investigated. The details of the experiments using these antenna arrays will be discussed in Section 7.2.3 and 7.2.4.

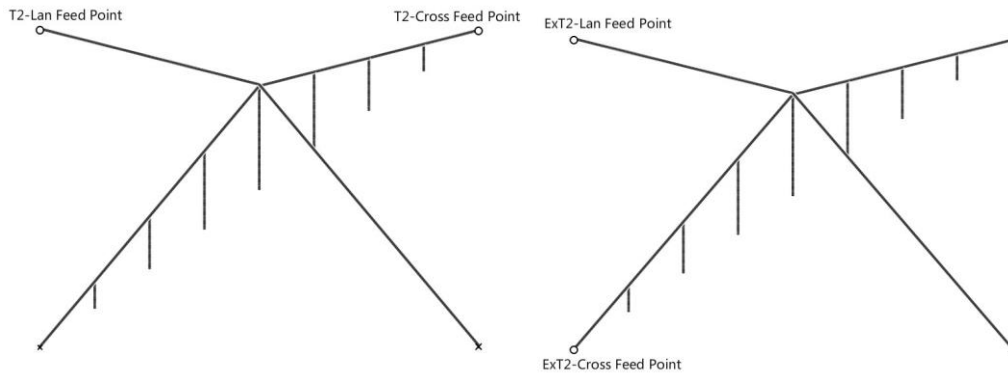


Figure 7.10 The structure of T2 (Left) and Ex-T2 (Right) array. These two arrays differ only with opposite feed point for the antenna perpendicular to the direction of Lancaster.

The modelling employs 9.040 MHz in order to get pure X mode reflection.

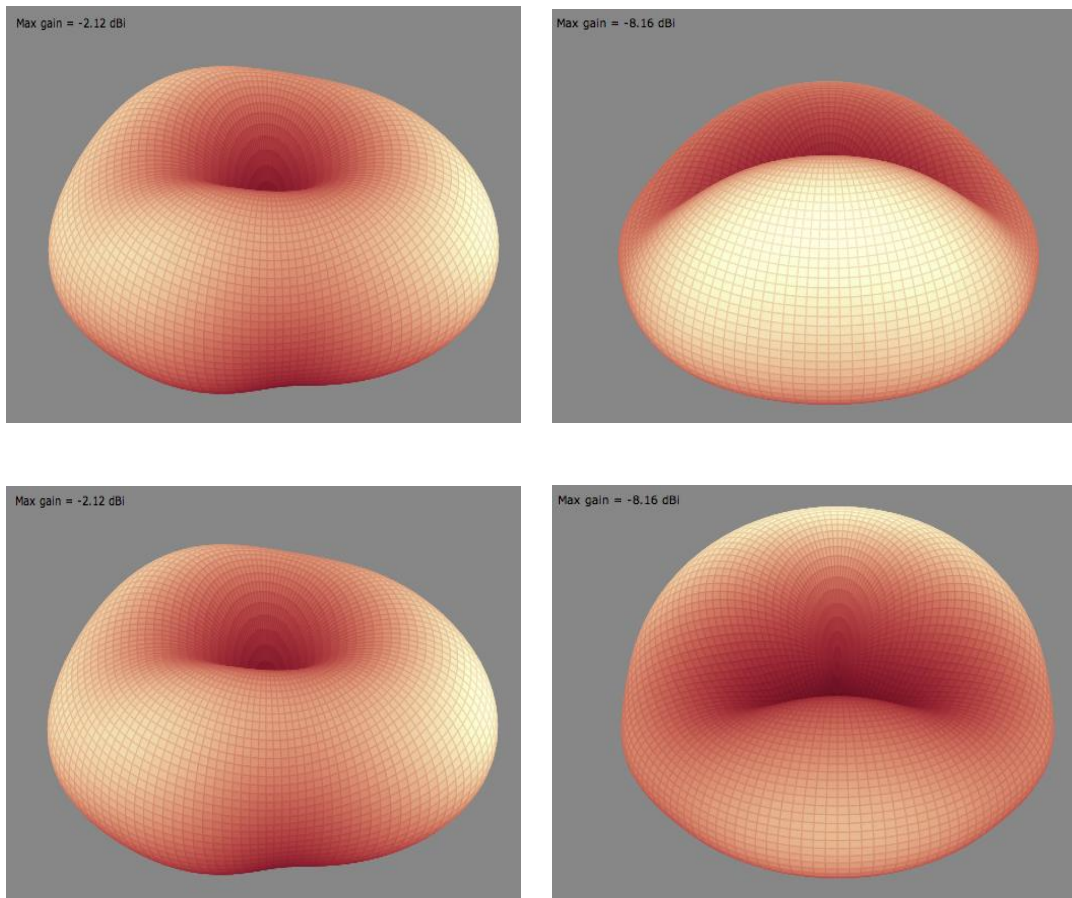


Figure 7.11 3D radiation pattern (9.040 MHz) for T2-Lan (Left-top), T2-Cross (Right-top), ExT2-Lan (Left-bottom), ExT2-Cross (Right-bottom), respectively.

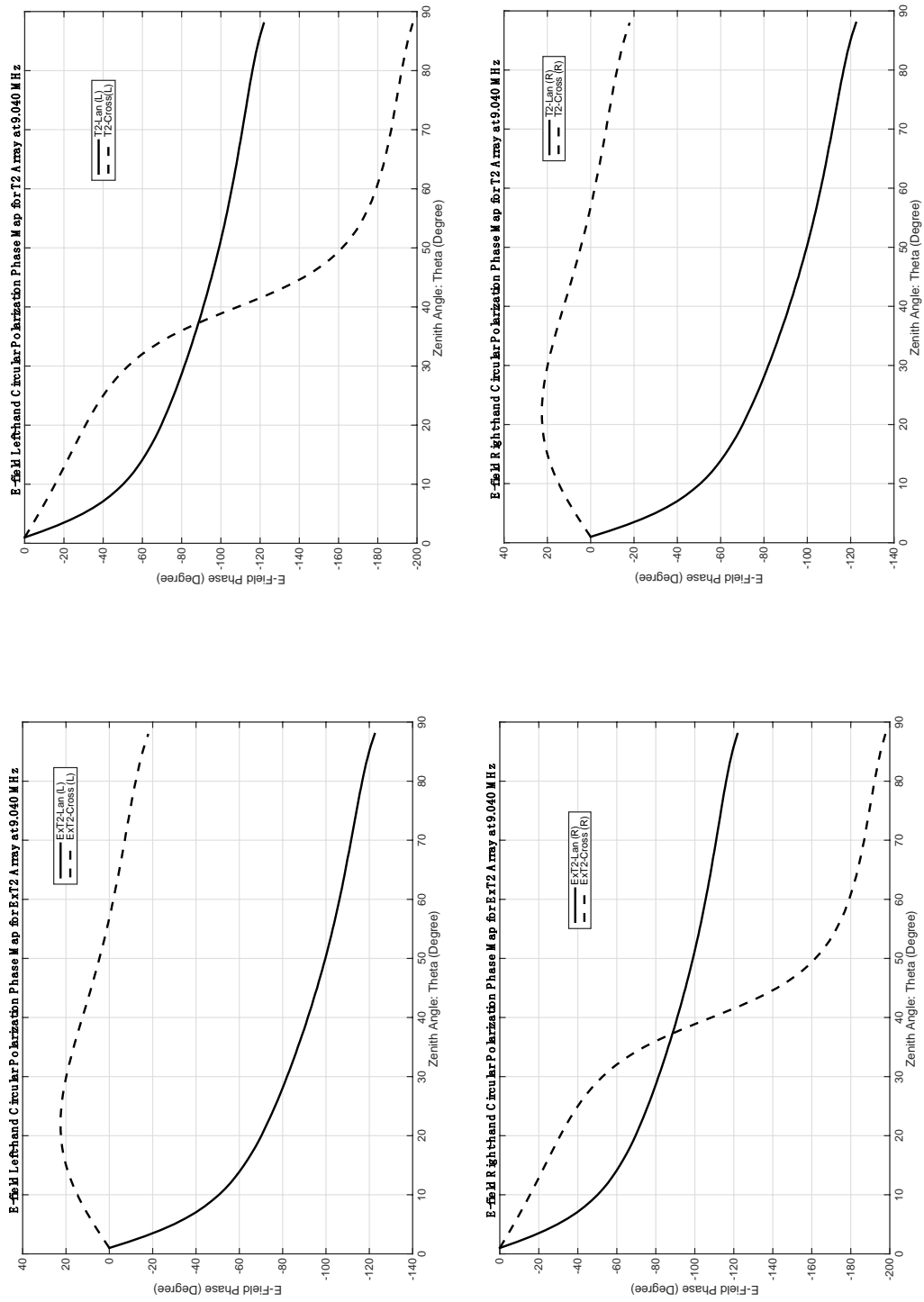


Figure 7.12 E-field left and right hand polarised phase map for the antenna array T2 and ExT2 at modelling frequency 9.040 MHz (ExT2-left: Left-top; T2-left: Right-top; ExT2-right: Left-bottom; T2-right: Right-bottom). It shows the same rule with ORG and ExORG array. The left and right hand phase is exchanged for T2 and ExT2 array with the opposite location of power source.

7.1.4 Antenna Array E2 Modelling

In order to get more phase difference difference in the investigated zenith angle interval, antenna arrays E2 and S2 were designed. The structure of the E2 array (see Figure 7.13) is also evolved from original crossed end-fed Vee array (ORG). In addition, there are four vertical elements, made of stainless steel wire, added on each antenna. These components are spaced by $1/6$ of the antenna length and connect the antenna with ground. An isolated metal mast is employed to support the array and these two antennas are isolated from each other by 10 cm at the crossing point. The antenna (E2-Lan) in X-axis is pointed to the direction of Lancaster; the other one (E2-Cross) is perpendicular to the transmission direction. The left-hand and right-hand phase response map of E2 is displayed in Figure 7.14 and Figure 7.15, respectively, using ORG array as reference.

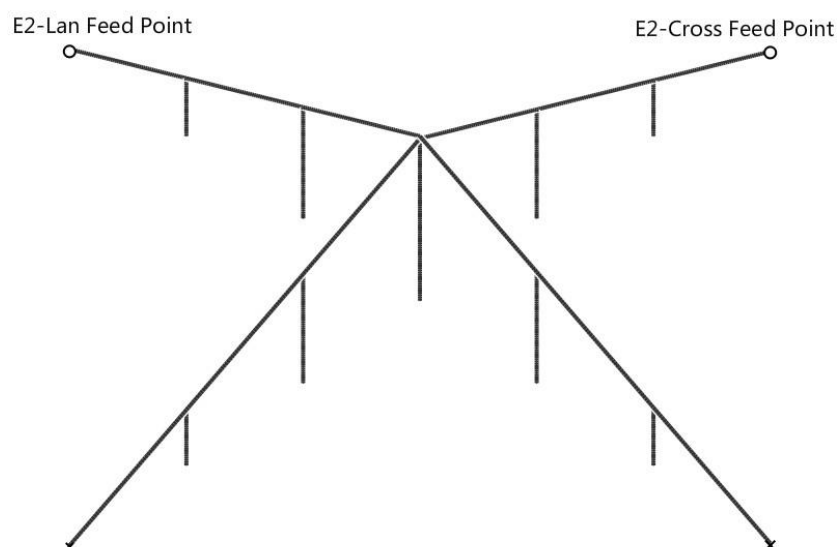


Figure 7.13 E2 Transmitting antenna array

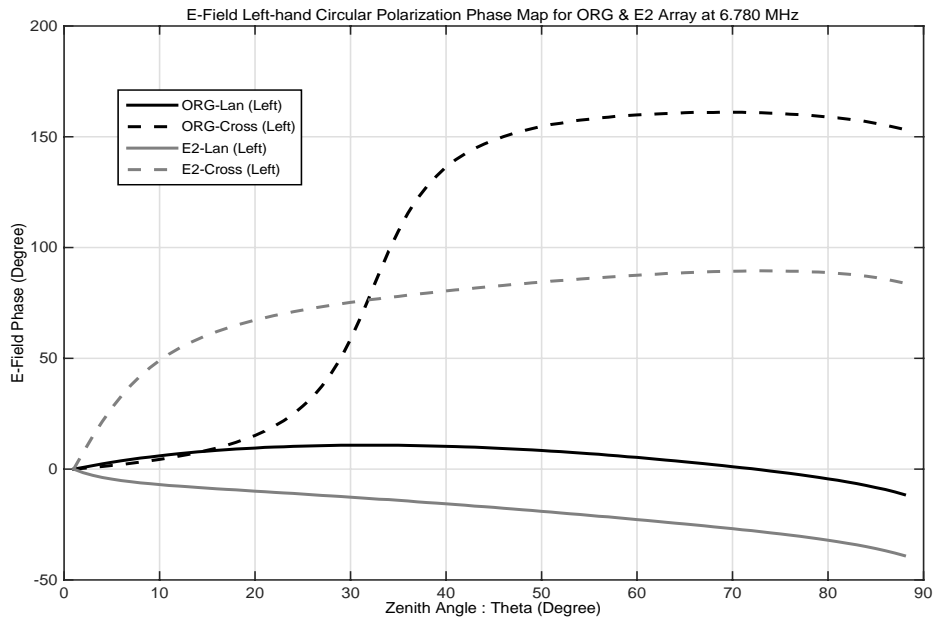


Figure 7.14 E-field left-hand circular polarization phase map of the E2 and ORG array with the transmission frequency 6.780 MHz.

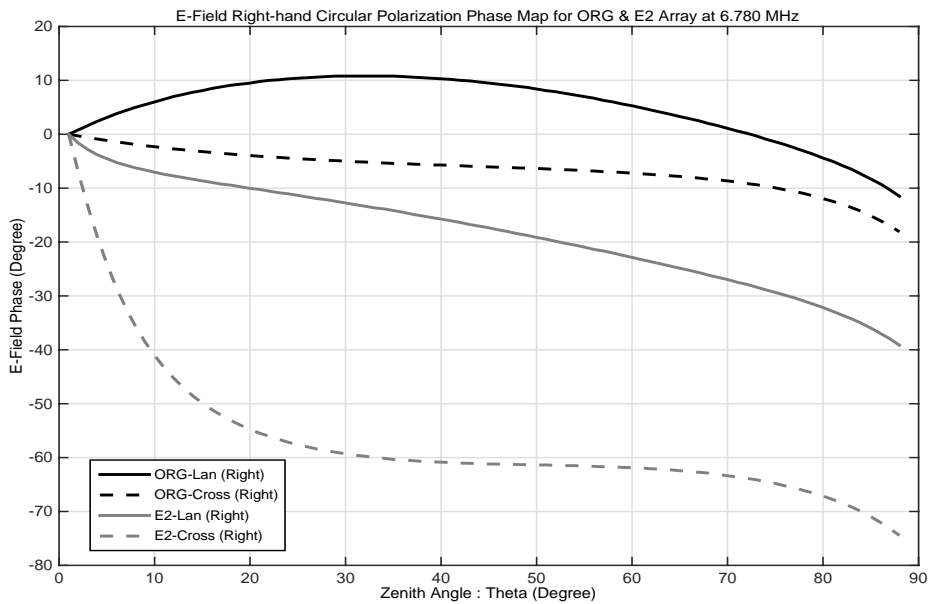


Figure 7.15 E-field right-hand circular polarization phase map of the E2 and ORG array with the transmission frequency 6.780 MHz.

Figure 7.14 and 7.15 show that: the phase difference difference (PDD) of the newly designed array E2 is obviously greater than ORG array for both left and right hand polarization in the zenith angle interval from 5° to 20° . According to the model, for the left-hand polarization, the array element E2-Lan can provide -2.6° phase difference, the crossed antenna E2-Cross can give 20.8° phase difference. As a result, the left-hand PDD provided by E2 array is 23.4° , which is significantly bigger than 1.5° generated by the ORG array. For the right-hand polarization, the phase difference for E2-Lan and E2-Cross is -2.6° and -16.3° , respectively. And the E2 array can generate a PDD of 13.7° for the right-hand polarization, which is also greater than ORG array (4.8°). The model shows that the array E2 is likely to produce more decorrelated signals both in O and X mode, compared with the ORG array. This has been demonstrated by the experiment in Section 7.2.5.

7.1.5 Antenna Array S2 Modelling

Another array S2 is designed based on E2. The idea of S2 is same with T2. One arm of S2 (S2-Lan) is identical with ORG-Lan; the other arm (S2-Cross) keeps same with E2-Cross, which has 4 vertical stainless steel wires connected with ground (see Figure 7.16).

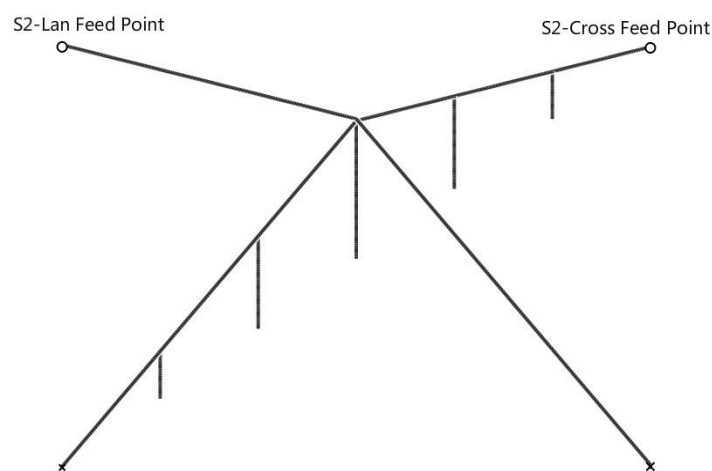


Figure 7.16 S2 Transmitting antenna array

Figure 7.17 and 7.18 show the phase variation comparison between the array S2 and ORG for the left and right hand circular polarization, respectively. The figures indicate that the arm of S2 pointed to Lancaster (S2-Lan) has a significantly left-hand phase changing at zenith angles from 5° to 20° . In addition, the right-hand phase changing of the arm S2-Cross is also faster than other antennas. As a result, the PDD generated by S2 array is obviously bigger than the referenced array ORG for both left and right hand circular polarization at zenith angles from 5° to 20° .

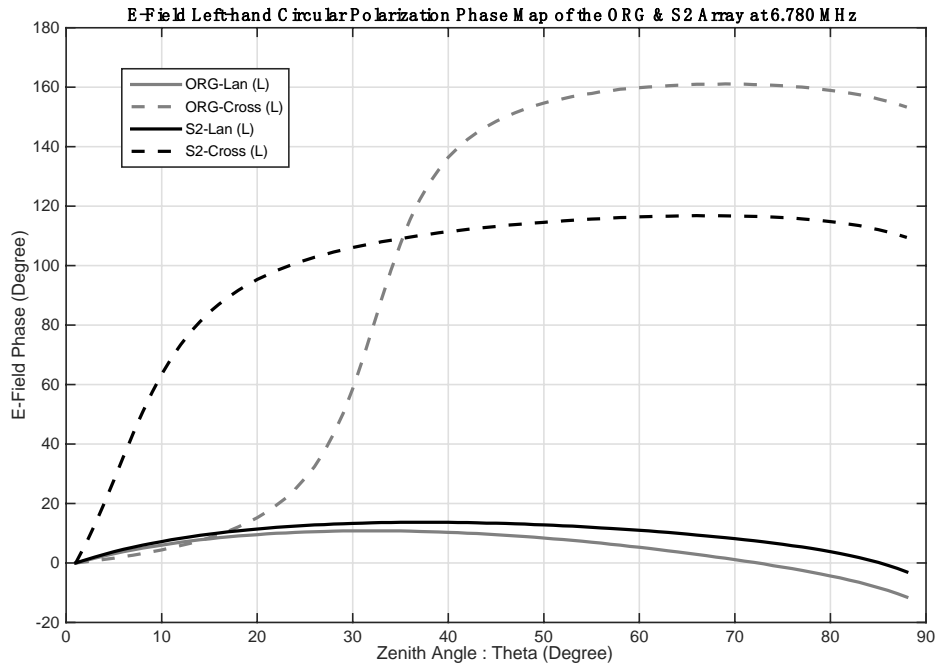


Figure 7.17 E-field left-hand circular polarization phase map of the S2 and ORG array with the transmission frequency 6.780 MHz

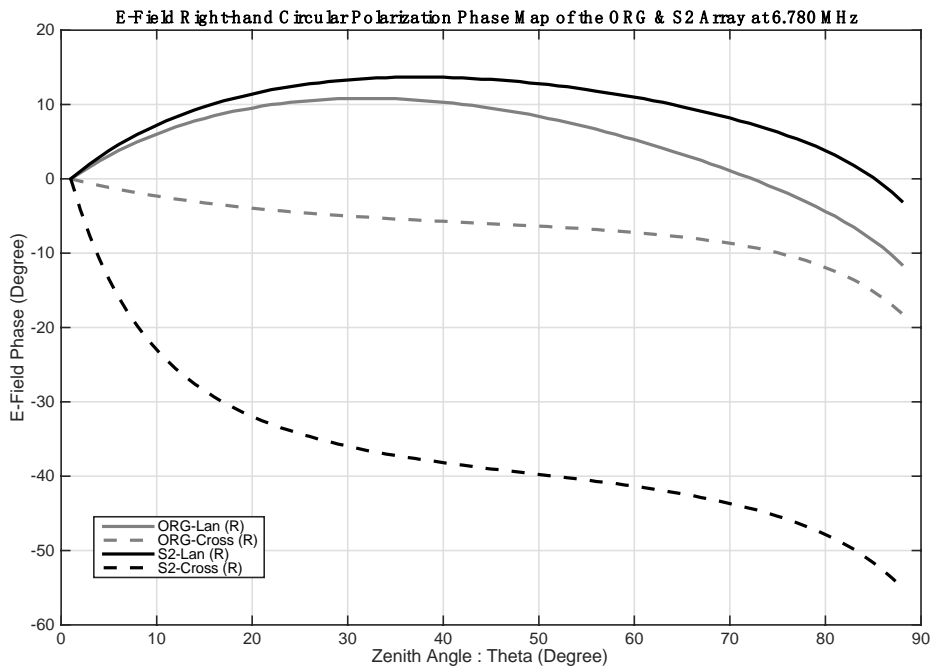


Figure 7.18 E-field right-hand circular polarization phase map of the S2 and ORG array with the transmission frequency 6.780 MHz

7.1.6 Non-Planar twisted (NPT) transmitting antenna array modelling

This novel antenna array is constructed in two parts: 1) for the Lancaster direction (along X axis), it is an end-fed Vee antenna which is 34 m long and 7.3m high (same as ORG-Lan); 2) for the other antenna, it is made of same end-fed Vee with twisted 60° in anticlockwise from perpendicular direction of Lancaster. Then it extends back to the perpendicular direction of Lancaster from the points at $\frac{1}{4}$ and $\frac{3}{4}$ length of the antenna (see Figure 7.19). In order to achieve this tweak, string is used to pull up the antenna at these two points. One point is pulling to Lancaster direction and the other one is pulling to the opposite direction, to create a right-handed helical shape. The left and right hand circular polarization phase map for NPT and ORG array are shown in Figure 7.20 and 7.21 respectively.

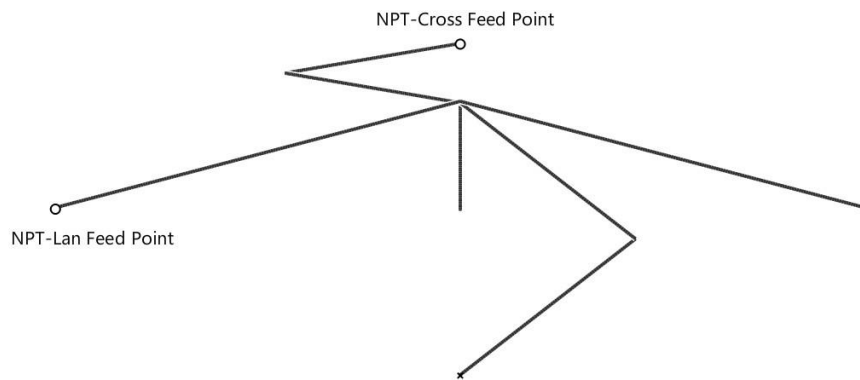


Figure 7.19 Non-Planar Twisted Transmitting Antenna Array

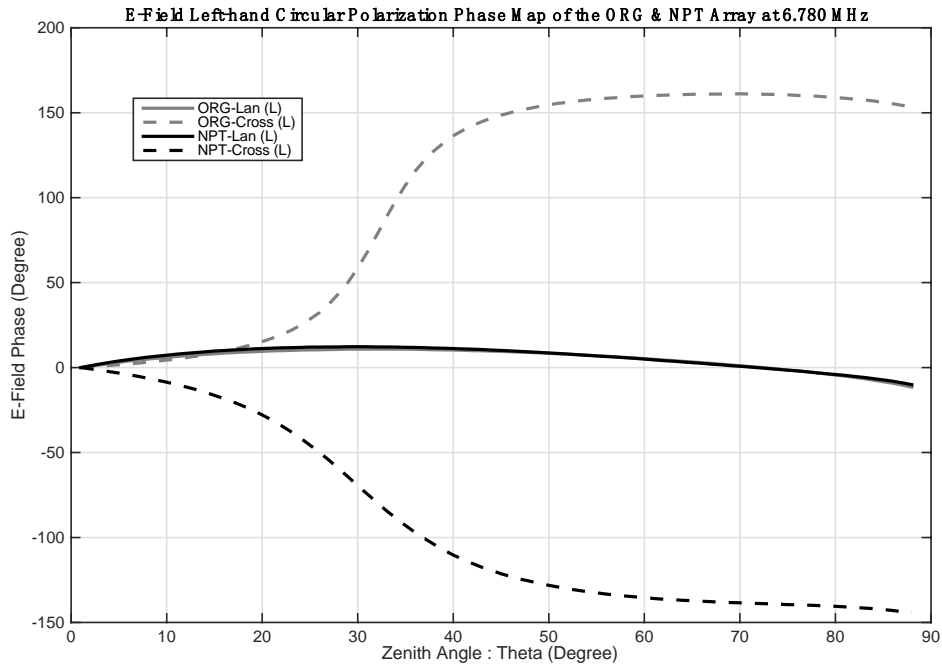


Figure 7.20 E-field left hand circular polarization phase map of the NPT and ORG array with the transmission nominal frequency 6.780 MHz.

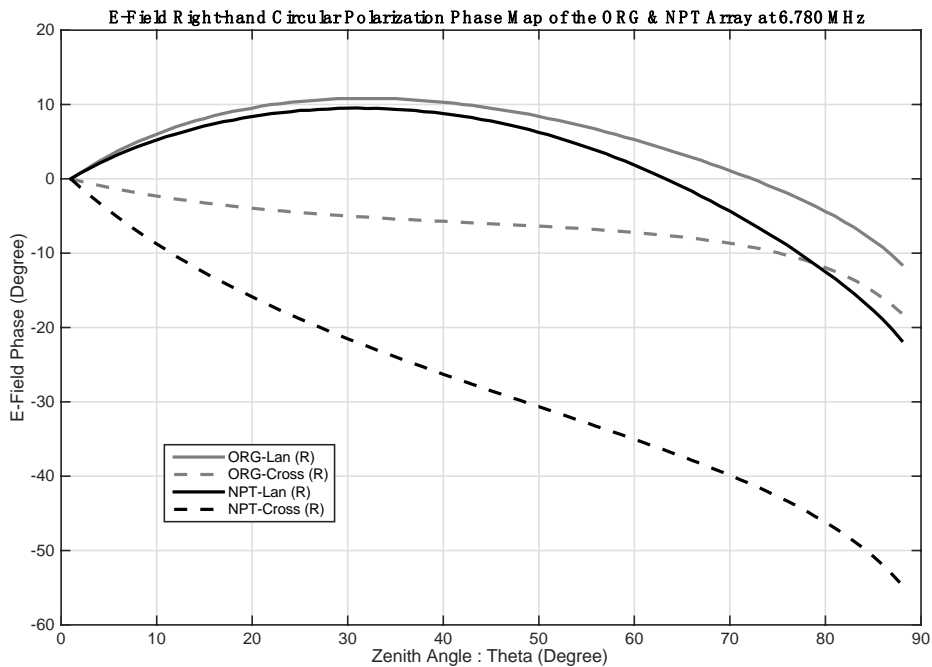


Figure 7.21 E-field right hand circular polarization phase map of the NPT and ORG array with the transmission nominal frequency 6.780 MHz.

For the left-hand polarization, as shown in Figure 7.20, the phase response for the antenna array element ‘NPT-Lan’ is almost same with ‘ORG-Lan’. However, the other arm ‘NPT-Cross’ can generate greater phase difference than ‘ORG-Cross’ in the investigated zenith angle interval $[5^\circ, 20^\circ]$. As a result, more phase difference can be obtained from NPT array for the left-hand polarization. For the right-hand polarization, although ‘NPT-Lan’ phase changing is slight less than ‘ORG-Lan’, the NPT array can still produce more decorrelated signals due to the twisted antenna ‘NPT-Cross’, which shows a significantly bigger phase changing compared with ‘ORG-Cross’. As a result, the newly designed non-planar twisted transmitting antenna array is more decorrelated than traditional crossed end-fed Vee array with the same ionosphere condition according to the modelling. This has also been demonstrated by the experiment results in Section 7.2.7.

7.2 Measurements for modelled novel antenna arrays

In this section, observations and results are represented from HF-MISO experiments in which the modelled transmitting antenna arrays were utilized. The original crossed end-fed Vee array (ORG) was employed as reference array, which showed a useful decorrelation level between the array elements in previous measurements. All the measurements were conducted via a 202 km radio link, transmitted CW signals at Bruntingthorpe and received at Lancaster.

7.2.1 Comparison of T1 and ORG array in 4×1 MISO measurement

7.2.1.1 Experimental Arrangement

A 4×1 MISO experiment was carried out on 27 June 2013. At the transmitter, the collocated crossed end-fed Vee array (ORG) and the antenna array T1 were utilized in the campaign. All these antennas made by stranded stainless steel wire were end-fed, resistively terminated and approximately 34 m long. For the ‘ORG’ array, one arm of the array (TX-1: ORG-Lan) was directed to the receiver site (Lancaster University). The other arm of the array (TX-2: ORG-Cross) was perpendicular to the previous arm. The mast supporting these two antennas was about 7.3 m tall. The spacing between the tops of these two antennas was 10 cm. The antenna array T1 was located at 50 m away from the ORG array. The basic configuration of T1 was same as the ORG array except for the vertical stainless steel wire elements, which provided an enhanced phase difference difference in the modelling (see Figure 7.2 and Figure 7.3). The transmitting frequency during the campaign was 6.780 MHz. In order to identify the signals send by different antennas, the signals frequencies were offset by 10 Hz (TX-1: 6.780000 MHz; TX-2: 6.780010 MHz; TX-3: 6.780020 MHz; TX-4: 6.780030 MHz). At the receiver, a wide band dipole antenna was employed which was located on the roof of the Lancaster University Engineering building.

7.2.1.2 Results and Discussion

The experiment was conducted for approximately 100 minutes. The antenna array ‘ORG’ and T1 transmitted CW signals at the same time. 91 one-minute data files were collected at the receiver between 11:46 GMT and 13:16 GMT. Figure 7.22 displays one frame of the received signals (58 seconds) sent by these two arrays at 13:00 GMT on 27 June 2013. The amplitude correlation coefficient for T1 and ORG array was 0.16 and 0.37 respectively during this period.

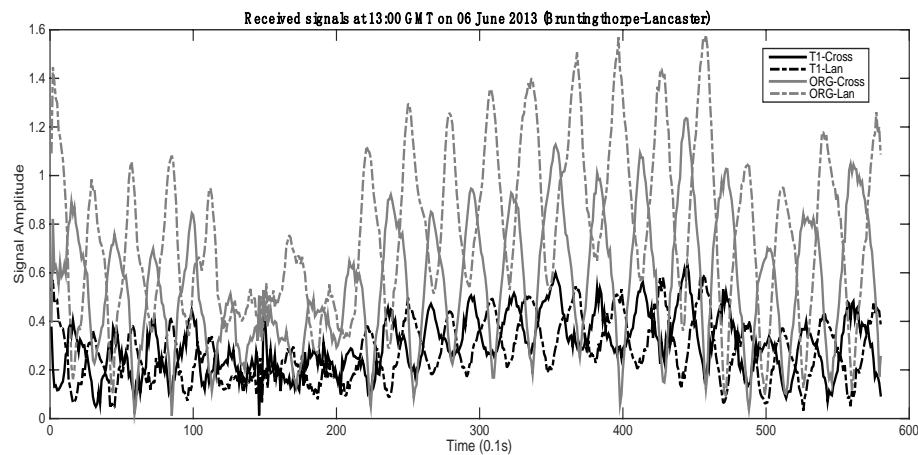


Figure 7.22 Received signals (amplitude) observed for a period of 58 seconds at 13:00 GMT on 27 June 2013 during a 4×1 HF-MISO experiment carried out between Bruntingthorpe and Lancaster. Four CW signals were transmitted at 6.780 MHz from Bruntingthorpe using the ORG and T1 array. In order to identify these signals, 10 Hz was used as the offset frequency.

Combined with vertical ionograms obtained from Chilton ionospheric station (which is situated approximately 191.6 km from the midpoint of the Bruntingthorpe-Lancaster path at a bearing of 167°), after being superimposed on the transmission curves (at 6.780 MHz), the signals propagation modes can be found on the ionograms. The ionogram overlaid with the transmission curves (1-hop and 2-hop at 6.780 MHz) corresponding to the measurement period is displayed in Figure 7.23. Under the prevailing ionosphere conditions, the virtual heights for 1-hop and 2-hop X mode signals were around 420 km and 430 km, respectively. Using these virtual reflection heights and the geographic distance between transmitter and receiver, it can be deduced that the zenith angle for the 1-hop and 2-hop signal are approximately 14° and 7° , respectively. Combined with the antennas' E-field left and right hand polarization phase map (see Figure 7.2 and 7.3), phase information for each antenna is displayed in Tables 7.1 and 7.2. The left-hand PDD provided by the ORG array and the T1 array are -1.5° and 7.5° , respectively. For the right-hand, the corresponding values are 4.8° and 10.4° , respectively. The result indicated that under the prevailing ionospheric conditions, no matter left-hand or right-hand circular polarization, the array T1 can provide a bigger PDD. As mentioned before, for a co-located antenna array, there is no spatial gain benefit to the correlation coefficient. Greater phase difference provided by co-located array elements means that the combination relationship for incident signals from different hops is more different. As a result, the array T1 is more decorrelated than the ORG array.

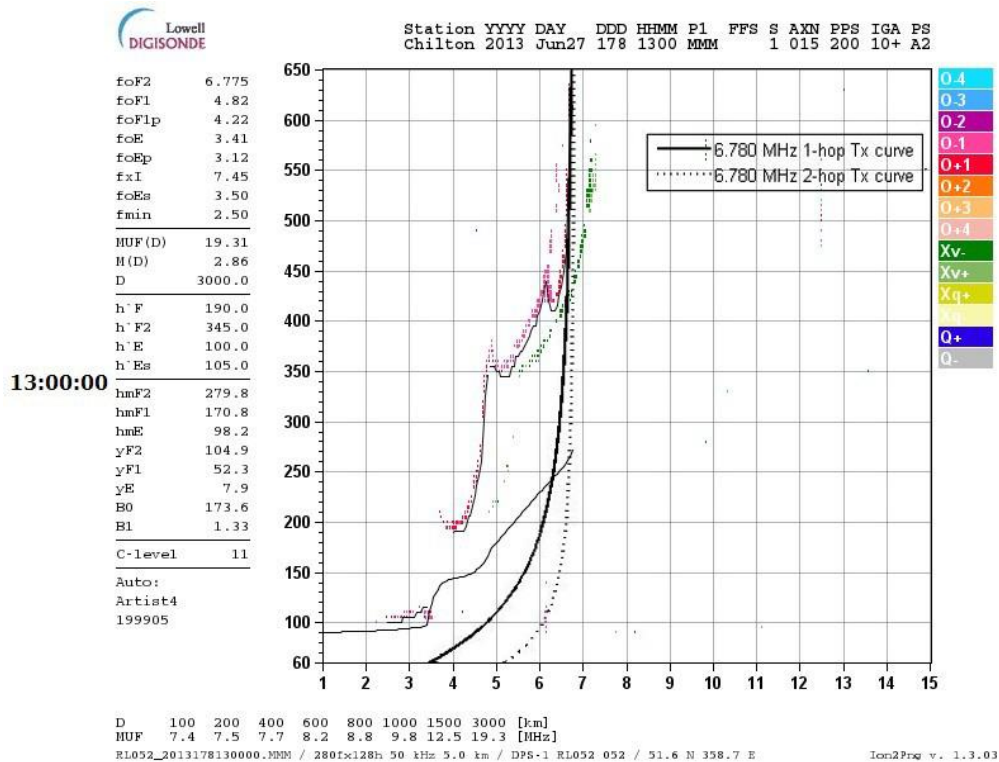


Figure 7.23 Vertical ionogram obtained from the Chilton ionospheric station superimposed on 1-hop and 2-hop transmission curves (6.780 MHz) for the Bruntingthorpe-Lancaster path at 13:00 GMT on 27 June 2013.

A graph of correlation coefficients changing with time for these two arrays during the measurement (top) and a graph of critical frequency variation for different ionosphere layers corresponding to the period (bottom) are displayed in Figure 7.24. It's worth noticing that almost all correlation coefficient values of the array T1 are less than the 'ORG' array value at the corresponding periods. A significantly drop for correlation coefficients occurred between 12:56 and 13:06, and can be investigated for both two arrays. After checked the corresponding ionograms (obtained from Chilton ionostation) and critical frequency variation for different

layers (see Figure 7.24 bottom), there was no significantly changing for ionosphere modes. However, the ionosphere at the mid-point of the radio path could be different to Chilton. There is a small (0.5 MHz) decrease in foF2 at Chilton about 10 minutes before the change in correlation, but it is uncertain whether it is this that leads to the change in correlation.

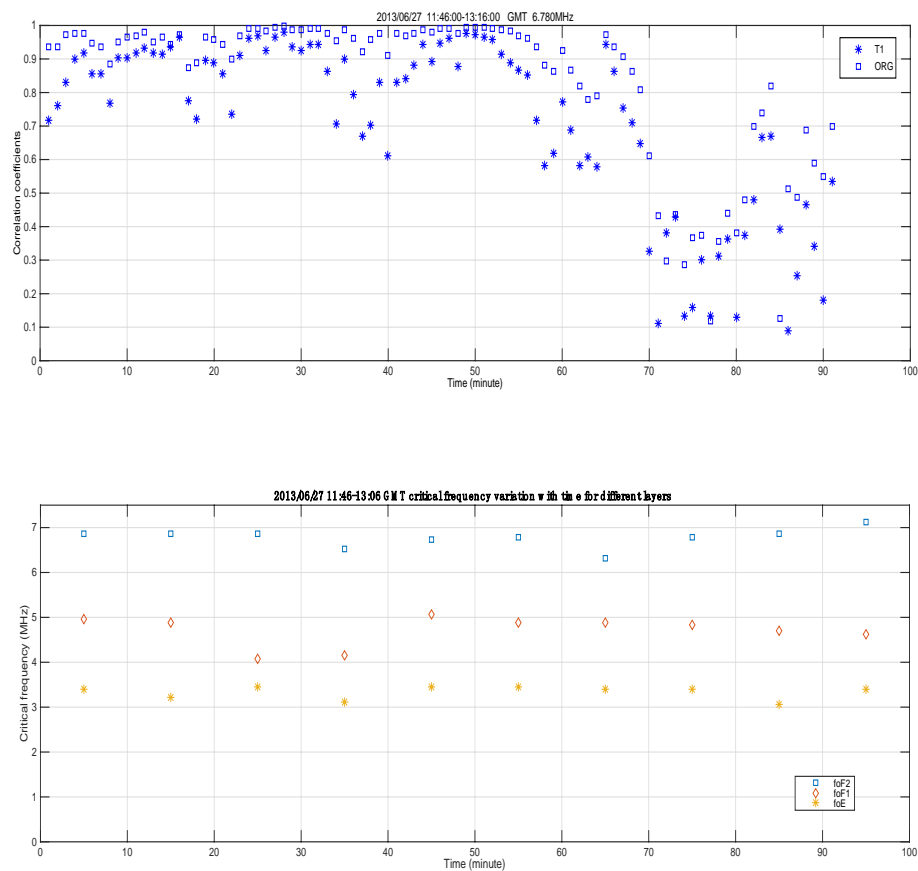


Figure 7.24 The time-varying correlation coefficients of the link obtained using different transmitter antenna arrays (top) and critical frequency variation for different ionosphere layers during the same period (bottom). Data collection was conducted between 11:46 GMT and 13:16 GMT on 27 June 2013.

Table 7.1 E-field (left-hand polarization) phase information for transmitting arrays (6.780 MHz) at 13:00 GMT on 27 June 2013

Unit (degree)	1-Hop signal E-field (left hand) Phase (Zenith: 14°)	2-Hop signal E-field (left hand) Phase (Zenith: 7°)	E-field (left hand) Phase Difference	E-field (left hand) Phase Difference provide by the array
ORG-Lan	7.8	4.4	3.4	-1.5
ORG-Cross	7.5	2.6	4.9	
T1-Lan	18.4	8.8	9.6	7.5
T1-Cross	3.5	1.3	2.2	

Table 7.2 E-field (right-hand polarization) phase information for transmitting arrays (6.780 MHz) at 13:00 GMT on 27 June 2013

Unit (degree)	1-Hop signal E-field (right hand) Phase (Zenith: 14°)	2-Hop signal E-field (right hand) Phase (Zenith: 7°)	E-field (right hand) Phase Difference	E-field (right hand) Phase Difference provide by array
ORG-Lan	7.8	4.4	3.4	4.8
ORG-Cross	-3.1	-1.7	-1.4	
T1-Lan	18.4	8.8	9.6	10.4
T1-Cross	-1.8	-0.9	-0.8	

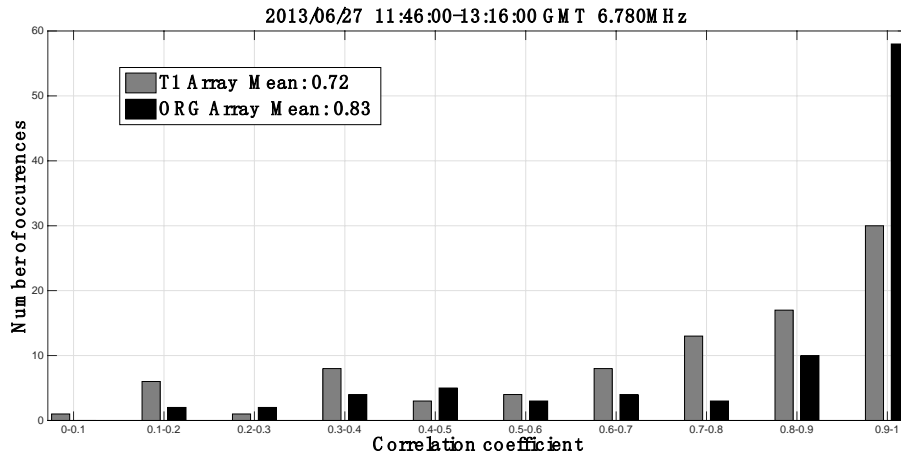


Figure 7.25 The occurrence frequency histograms of the correlation coefficients (of 58 s amplitude records) between original end-fed Vee array inter-elements (TX-1: ORG-Lan and TX-2: ORG-Cross) and the array T1 inter-elements (TX-3: T1-Lan and TX-4: T1-Cross) at nominal frequency 6.780 MHz. The 4×1 MISO experiment was carried out between Bruntingthorpe and Lancaster on 27 June 2013. 91 one-minute data files were collected and analysed.

For comparison, the occurrence frequency histograms of the correlation coefficients (of the 58 s amplitude records) between the antenna array ‘ORG’ (TX-1 and TX-2) and T1 array (TX-3 and TX-4) are shown in Figure 7.25. The mean value of correlation coefficients for the collocated end-fed Vee antenna array and T1 array were 0.83 and 0.72, respectively. For the T1 array, approximately 67% and 34% of the one-minute correlation coefficients values were less than 0.9 and 0.7, respectively. However, these indices fall to 36% and 22% respectively for the ‘ORG’ array. As a result, the measurement shows that the T1 array is more decorrelated than the ORG array.

7.2.2 Comparison of T2 and ORG array in 4×1 MISO measurement

7.2.2.1 Experimental Arrangement

In order to verify the new diversity based on antenna arrays phase difference difference, another 4×1 HF-MISO experiment was conducted on 03 July 2013. The newly designed antenna array T2 was used in the campaign (TX-3: T2-Lan and TX-4: T2-Cross). The array was the combination of ORG array and T1. The arm directed to Lancaster (TX-3: T2-Lan) was identical to the arm of ORG array. The other arm of the array (TX-4: T2-Cross) has the same vertical stainless steel wire elements as T1. ORG array was employed as the reference antennas as in the previous experiment (TX-1: ORG-Lan and TX-2: ORG-Cross). The nominal transmission frequency was 6.780 MHz and 10 Hz was used as the offset frequency (TX-1: 6.780000 MHz; TX-2: 6.780010 MHz; TX-3: 6.780020 MHz; TX-4: 6.780030 MHz). The output power was approximately 55 W for each antenna. The receiver was the same as described in Section 7.2.1.

7.2.2.2 Results and Discussion

The experiment was carried out for nearly 90 minutes and 80 one-minute data files were collected between 15:01 GMT and 16:20 GMT. Figure 7.26 showed the time-varying correlation coefficients. Almost all values of correlation coefficients of T2 array were lower than ORG array during the campaign.

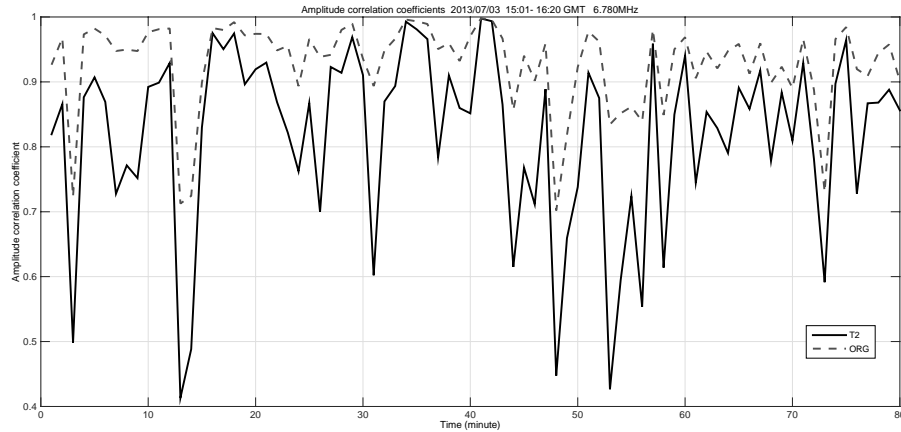


Figure 7.26 The time-varying correlation coefficients of the link obtained using different transmitter antenna arrays. Data collection was conducted between 15:01 GMT and 16:20 GMT on 03 July 2013.

The occurrence frequency histograms of the amplitude correlation coefficients between T2 array elements and ORG array elements at the receiving antenna are displayed in Figure 7.27. Under the prevailing ionospheric conditions, 78% correlation coefficient values were higher than 0.9 for the ORG array during the campaign period. By comparison, for the antenna array T2, only 29% of correlation coefficient values were higher than 0.9. The experimental result verified that, under the prevailing ionospheric conditions, the correlation level between collocated heterogeneous antennas can be decreased by enhanced array elements phase difference difference.

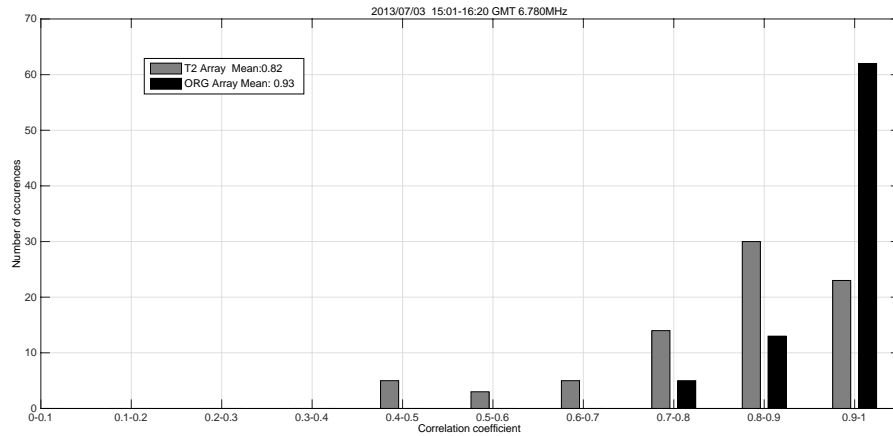


Figure 7.27 The occurrence frequency histograms of the correlation coefficients (of 58 s amplitude records) between ORG array inter-elements (TX-1: ORG-Lan and TX-2: ORG-Cross) and T2 array inter-elements (TX-3: T2-Lan and TX-4: T2-Cross) at nominal frequency 6.780 MHz. The 4×1 MISO experiment was carried out between Bruntingthorpe and Lancaster on 03 July 2013. 80 one-minute data files were collected and analysed.

7.2.3 Comparison of T2 and ExT2 in 4×1 MISO measurement

7.2.3.1 Experimental Arrangement (T2 and ExT2)

Another 4×1 MISO experiment was conducted on 8 October 2013. Antenna arrays T2 and ExT2 were utilized in the campaign at the transmitter side. These two arrays are separated by 50 m in the direction of the radio link. One arm (T2-Lan) of the array T2, which points to the direction of Lancaster, was made by 34 m long end-fed Vee antenna. The other arm (T2-Cross) of T2 was built crossed to the T2-Lan with same main structure, except that 6 vertical stainless steel wires were

added which enhanced the phase difference according to the previous campaigns. The top of these two antennas were spaced by 10 cm on the same mast (7.3 m high). As mentioned before, the array ExT2 has the same structure with T2 except that the feed point was located at the opposite end point for the crossed arm. A CW signal was used in the campaign with the transmission frequency 9.040 MHz and 10 Hz was utilized as the offset frequency (ExT2-Lan: 9.040000 MHz; ExT2-Cross: 9.040010 MHz; T2-Lan: 9.040020 MHz; T2-Cross: 9.040030 MHz). At the receiver, a whip antenna (5 m high) was employed to pick up these four CW signals.

7.2.3.2 Results and Discussion

The experiment was carried out from 10:00 GMT to 16:00 GMT. 61 one-minute data files were extracted from the receiver side between 11:40 GMT and 12:40 GMT. During this period, according to the ionogram obtained from Chilton ionospheric station, the ionosphere only supported X mode propagation for the transmission frequency 9.040 MHz (see Figure 7.29). The occurrence frequency histogram of correlation coefficients between T2 array (T2-Lan and T2-Cross) and ExT2 array (ExT2-Lan and ExT2-Cross) is displayed in Figure 7.28. The mean value of correlation coefficients for the T2 and ExT2 arrays were 0.78 and 0.75, respectively. For the T2 array, about 85% and 28% of the correlation coefficients were less than 0.9 and 0.7, respectively. However, these indices increased to 92% and 36% respectively for ExT2 array. This means that under the prevailing

ionosphere conditions, ExT2 array had a lower level of correlation than T2 array with transmission frequency 9.040 MHz.

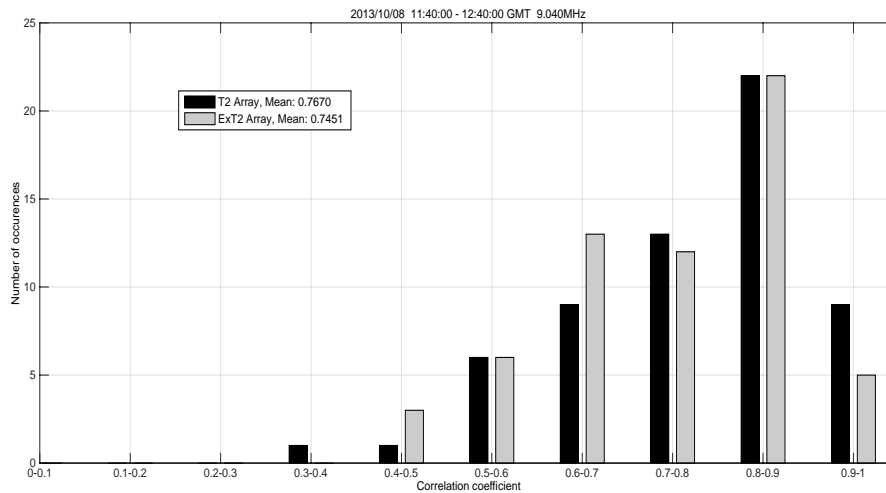


Figure 7.28 The occurrence frequency histograms of the correlation coefficients (of 58 s magnitude records) between the array ExT2 inter-elements (ExT2-Lan and ExT2-Cross) and the array T2 inter-elements (T2-Lan and T2-Cross) at frequency 9.040 MHz. The 4 × 1 MISO campaign was conducted from 11:40 GMT to 12:40 GMT between Bruntingthorpe and Lancaster on 08 October 2013. 61 one-minute data files were collected and analysed.

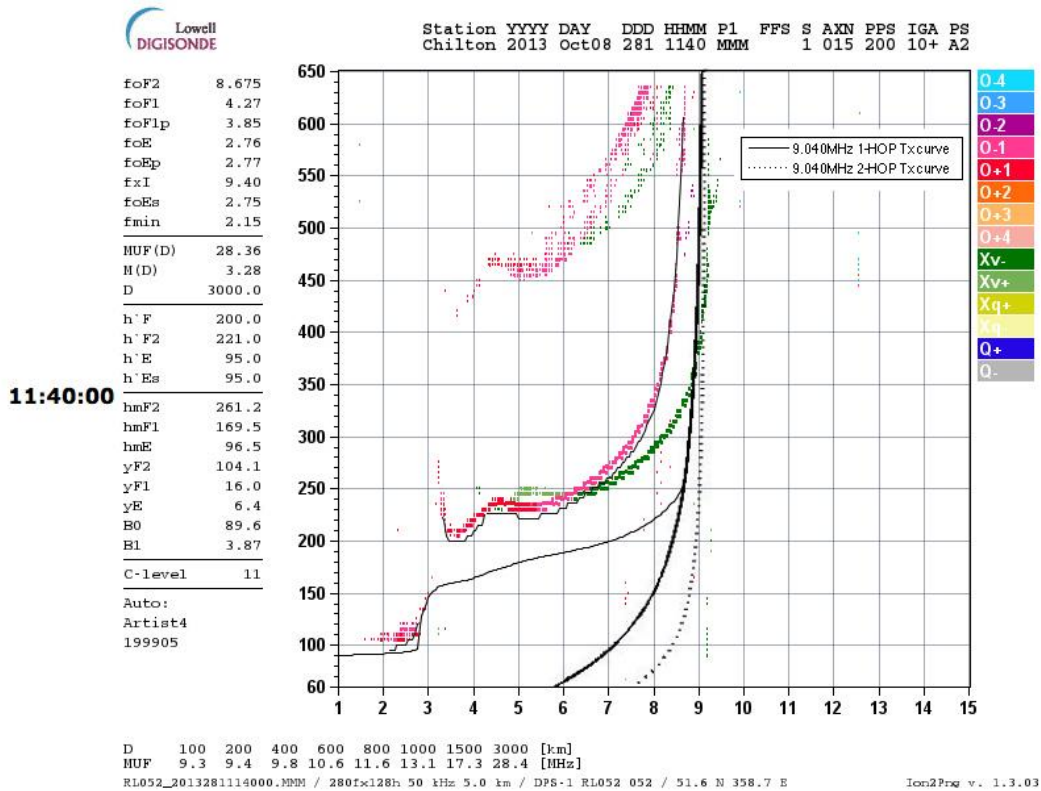


Figure 7.29 Vertical ionogram obtained from the Chilton ionospheric station superimposed on 1-hop and 2-hop transmission curves (9.040 MHz) for the Bruntingthorpe-Lancaster path at 11:40 GMT on 08 October 2013.

After superimposing the transmission curves (9.040 MHz) on to the prevailing vertical ionogram, the virtual reflection height of 1-hop and 2-hop signal can be found. For instance, at 11:40 GMT, only X mode signal can be reflected back to ground for the transmission frequency 9.040 MHz. The virtual reflection height for 1-hop and 2-hop signal was 350 km and 420 km, respectively (see Figure 7.29). Since the distance of the radio link is 202 km, it can be deduced that the zenith angles for launching at the transmitter side is 16° for 1-hop signal and 7° for 2-hop

signal. Combined with the E-field left and right hand circular polarization phase map of antenna array T2 and ExT2 at 9.040 MHz (displayed in Figure 7.12), the left and right PDD provided by these two arrays are displayed in Tables 7.3 and 7.4. The values of PDD produced by these two arrays are nearly same but with opposite polarization. For the E field left-hand polarization, the PDD provided by the array ExT2 is approximately -34.4° , which is significantly bigger than the value produced by the array T2 (-9.7°). In other words, the modelling simulation shows that the array ExT2 can have a lower correlation level between transmitting signals with left-hand polarization; the array T2 can produce more de-correlated signals with right-hand polarization with transmission frequency 9.040 MHz. Since the experiment was carried out with X mode only, and the array ExT2 showed a lower level of correlation in the campaign, it shows that: X mode corresponds to left-handed polarization in NEC-2 modelling. This is opposite with the X mode traditional definition in text book [Davies, 1990]. Section 7.2.4 will verify this finding using original crossed end-fed Vee antenna arrays with a different transmission frequency.

Table 7.3 E-field (left-hand) phase information for transmitting arrays (9.040 MHz) at 11:40 GMT on 8 October 2013

Unit (degree)	1-hop signal E-field (left hand) Phase (Zenith: 16°)	2-hop signal E-field (left hand) Phase (Zenith: 7°)	E-field (left hand) Phase Difference	E-field (left hand) PDD provide by the array
T2-Lan	-63.4	-39.5	-23.9	-9.7
T2-Cross	-24.8	-10.6	-14.2	
ExT2-Lan	-64.0	-39.9	-24.1	-34.4
ExT2-Cross	20.7	10.4	10.3	

Table 7.4 E-field (right-hand) phase information for transmitting arrays (9.040 MHz) at 11:40 GMT on 8 October 2013

Unit (degree)	1-hop signal E-field (right hand) Phase (Zenith: 16°)	2-hop signal E-field (right hand) Phase (Zenith: 7°)	E-field (right hand) Phase Difference	E-field (right hand) PDD provide by the array
T2-Lan	-64.0	-39.9	-24.1	-34.4
T2-Cross	20.7	10.4	10.3	
ExT2-Lan	-63.4	-39.5	-23.9	-9.7
ExT2-Cross	-24.8	-10.6	-14.2	

7.2.4 Comparison of ORG and ExORG in 4 × 1 MISO measurement

7.2.4.1 Experimental Arrangement (ORG and ExORG)

In order to verify ionosphere X mode is left-hand polarization in NEC-2 modelling, a new experiment was carried out in 14 April 2014. The original crossed end-fed Vee antenna arrays ORG and Ex-ORG (see Figure 7.7), which had the opposite power feed for the cross pair, was employed with a lower transmission frequency 8.100 MHz and 10 Hz frequency offset (ExORG-Lan: 8.100000 MHz; ExORG-Cross: 8.100010 MHz; ORG-Lan: 8.100020 MHz; ORG-Cross: 8.100030 MHz). Before the campaign was conducted, the modelling work showed that the array ExORG had a greater phase difference difference with left-hand polarization for zenith angle between 5° and 20° (see Figure 7.9).

7.2.4.2 Results and Discussion

The campaign was carried out from 14:10:00 GMT to 15:50:00 GMT. 101 one-minute data files were collected and analysed. The ionosphere only supported X mode propagation for the transmission frequency (8.100 MHz) during that period. This was confirmed by Chilton ionospheric station (see Figure 7.31). The occurrence frequency histogram of magnitude correlation coefficients between ORG array (ORG-Lan and ORG-Cross) and ExORG array (ExORG-Lan and ExORG-Cross) is displayed in Figure 7.30. The mean value of correlation coefficient for the array ORG and ExORG was 0.73 and 0.70, respectively. There

were approximately 89% of correlation coefficients below 0.9 for the ORG array, which was same as the array ExORG. The percentage of correlation coefficients below 0.7 for the array ORG and ExORG was about 41% and 43%, respectively. As a result, at the prevailing ionosphere condition with transmission frequency 8.100 MHz, antenna array ExORG showed a slightly lower level of correlation between the array elements than the array ORG.

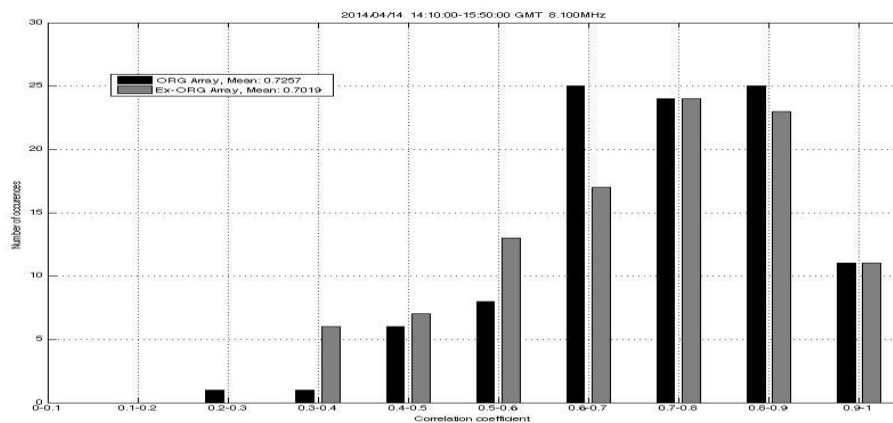


Figure 7.30 The occurrence frequency histograms of the correlation coefficients (of 58 s magnitude records) between the original crossed end-fed Vee antenna array inter-elements (ORG-Lan and ORG-Cross) and the array ExORG inter-elements (ExORG-Lan and ExORG-Cross) at frequency 8.100 MHz. The 4 × 1 MISO campaign was conducted between Bruntingthorpe and Lancaster on 14 April 2014. 101 one-minute data files were collected and analysed.

Combined with the prevailing vertical ionogram (see Figure 7.31), after being superimposed on the transmission curves (8.100 MHz), the virtual reflection height of 1-hop and 2-hop signal can be found as 348 km and 352 km, respectively.

Utilizing the same propagation model, it can be deduced that the zenith angles for 1-hop and 2-hop signal are 16° and 8° , respectively. The left and right hand phase difference difference produced by these two arrays are displayed in Table 7.5 and 7.6. The left-hand phase difference difference provided by the antenna array ExORG is approximately -110.9° , which is significantly better than the -11.3° provided by the array ORG. The modelling prediction was verified by the experimental result. This result also shows that X mode corresponds to left-hand polarization in NEC2.

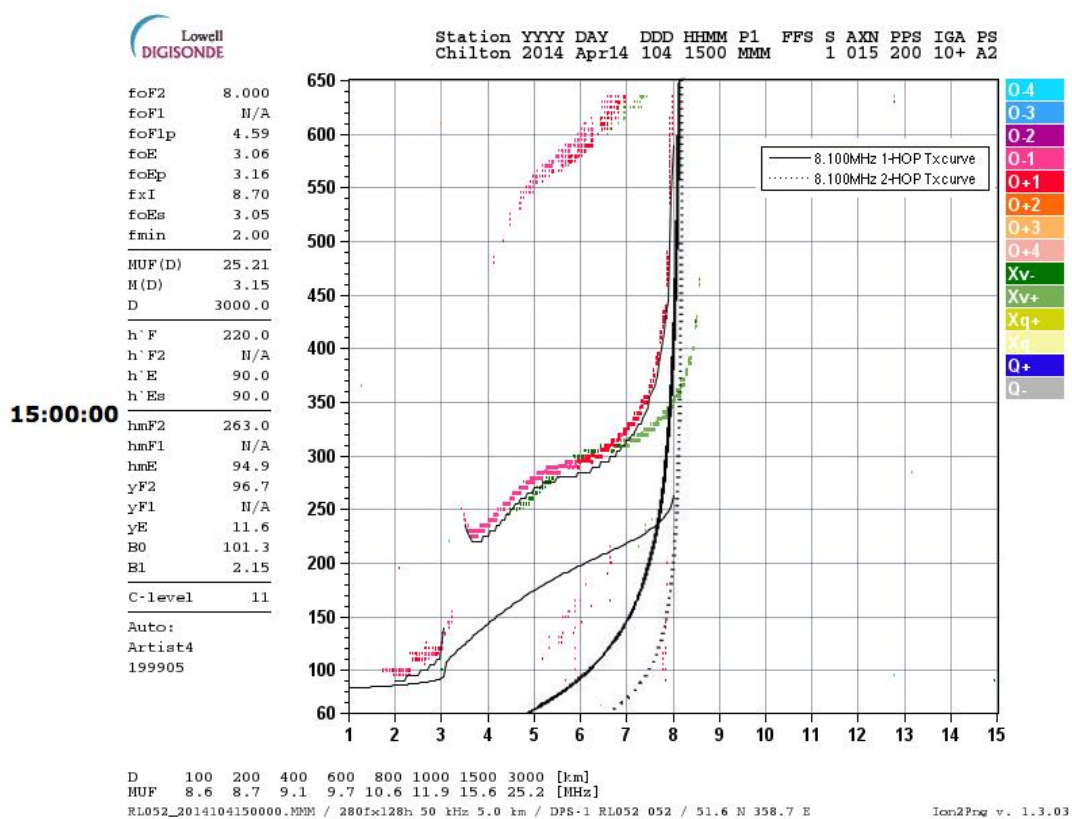


Figure 7.31 Vertical ionogram obtained from the Chilton ionospheric station superimposed on 1-hop and 2-hop transmission curves (8.100 MHz) for the Bruntingthorpe-Lancaster path at 15:00 GMT on 14 April 2014.

Table 7.5 E-field (left-hand polarization) phase information for transmitting arrays (8.100 MHz) at 15:00 GMT on 14 April 2014

Unit (degree)	1-hop signal E-field (left hand) Phase (Zenith: 16°)	2-hop signal E-field (left hand) Phase (Zenith: 8°)	E-field (left hand) Phase Difference	E-field (left hand) PDD provide by the array
ORG-Lan	-45.6	-32.9	-12.7	-11.4
ORG-Cross	-4.3	-2.9	-1.3	
ExORG-Lan	-45.4	-32.7	-12.7	-110.9
ExORG-Cross	161.4	63.2	98.2	

Table 7.6 E-field (right-hand polarization) phase information for transmitting arrays (8.100 MHz) at 15:00 GMT on 14 April 2014

Unit (degree)	1-hop signal E-field (right hand) Phase (Zenith: 16°)	2-hop signal E-field (right hand) Phase (Zenith: 8°)	E-field (right hand) Phase Difference	E-field (right hand) PDD provide by the array
ORG-Lan	-45.4	-32.7	-12.7	-110.7
ORG-Cross	161.1	63.2	98.0	
ExORG-Lan	-45.6	-32.9	-12.7	-11.4
ExORG-Cross	-4.2	-2.9	-1.3	

7.2.5 Comparison of E2 and ORG array in 4×1 MISO measurement

7.2.5.1 Experimental Arrangement

A 4×1 MISO measurement was conducted on 10 July 2014. At the transmitter, the newly designed heterogeneous antenna array E2 and reference antenna array ORG were employed. One arm of the new array, E2-Lan, was pointing in the direction of the receiving site. The other arm of the array, E2-Cross, was supported by the same mast and was perpendicular to the previous arm. The wires were isolated at the crossing point, which was approximately 7.3 m above the ground level. Each arm of the array was composed of nearly 34 m of stranded stainless steel wire with vertical wire elements connected with the ground. The referenced antenna array ORG was built with the same height and length and located about 50m away from the array E2. The transmitting frequency was set to 6.780 MHz. 10 Hz was selected as the offset frequency in order to identify the signals from different transmitting antennas (ORG-Lan: 6.780000 MHz; ORG-Cross: 6.780010 MHz; E2-Lan: 6.780030 MHz; E2-Cross: 6.780040 MHz). A whip antenna (5 m high) was set up to pick up these signals at the receiving site near Lancaster University.

7.2.5.2 Results and Discussion

The experiment was carried out between 14:00 GMT and 15:00 GMT. Four CW signals were sent simultaneously from the transmitting site. 61 one-minute data files were collected and analysed at the receiver end. One frame of received signals

at 14:10 GMT during the measurement were presented in Figure 7.32 and Figure 7.33. The amplitude correlation coefficient for the E2 array and ORG array was 0.23 and 0.55, respectively, corresponding to the period.

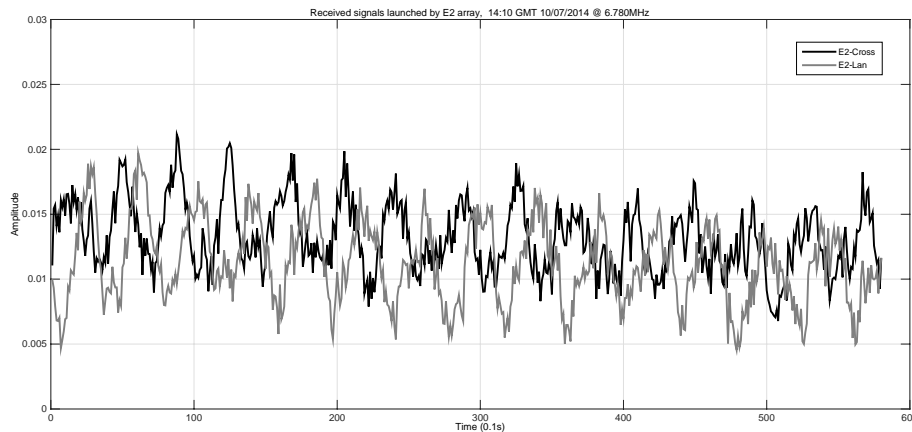


Figure 7.32 Received signals from transmitting array E2 (58 second) at 14:10 GMT on 10 July 2014. The absolute value of amplitude correlation coefficient between the received signals is 0.23.

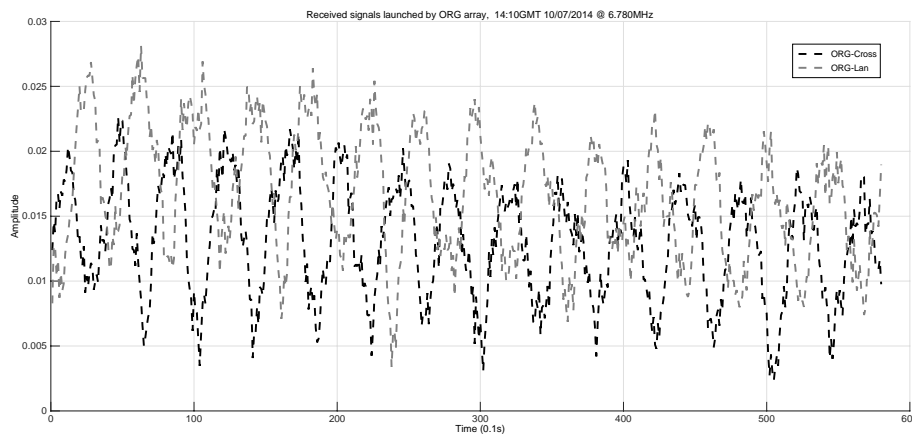


Figure 7.33 Received signals from transmitting array ORG (58 second) at 14:10 GMT on 10 July 2014. The absolute value of amplitude correlation coefficient between the received signals is 0.55.

The ionogram at 14:10 GMT on 10 July 2014 from Chilton ionospheric station is presented in Figure 7.34. After overlaying the transmission curves (1-hop and 2-hop at 6.780 MHz), the virtual reflection height can be found: for O mode, the 1-hop and 2-hop signal are reflected at a virtual height of approximately 370 km and 390 km, respectively; for X mode, the virtual reflection heights become about 370 km for both 1-hop and 2-hop signal. Combined with the geographic distance of the radio link 202 km, the launched zenith angle at the transmitter site can be deduced: for the O mode, the zenith angle of 1-hop and 2-hop are 15° and 7° , respectively; for the X mode, the zenith angle of 1-hop and 2-hop are 15° and 8° , respectively. Combining with left and right hand circular phase map of E2 and ORG (see Figure 7.14 and 7.15), the E-field PDD produced by these two arrays can be deduced. Table 7.7 shows that, for the O mode propagation, the PDD produced by the antenna array E2 and referenced array ORG is approximately 14.7° and 5.3° , respectively. Table 7.8 displays the PDD produced by these two arrays under X mode. Antenna array E2 can produce PDD of nearly -20.8° between the array elements, compared to about -2.2° in the array ORG. As a result, antenna array E2 can produce greater phase difference compared with original crossed end-fed Vee antenna array for both the O and X mode under the prevailing ionospheric conditions.

As mentioned before, the elements of these two arrays are collocated, which means that there is no spatial diversity gain benefit to the correlation coefficients. Large

phase difference difference between co-located transmitting array elements means that the launched signals have more independent linear combination of the 1-hop and 2-hop signals. As a result, the correlation level of the received signals is reduced.

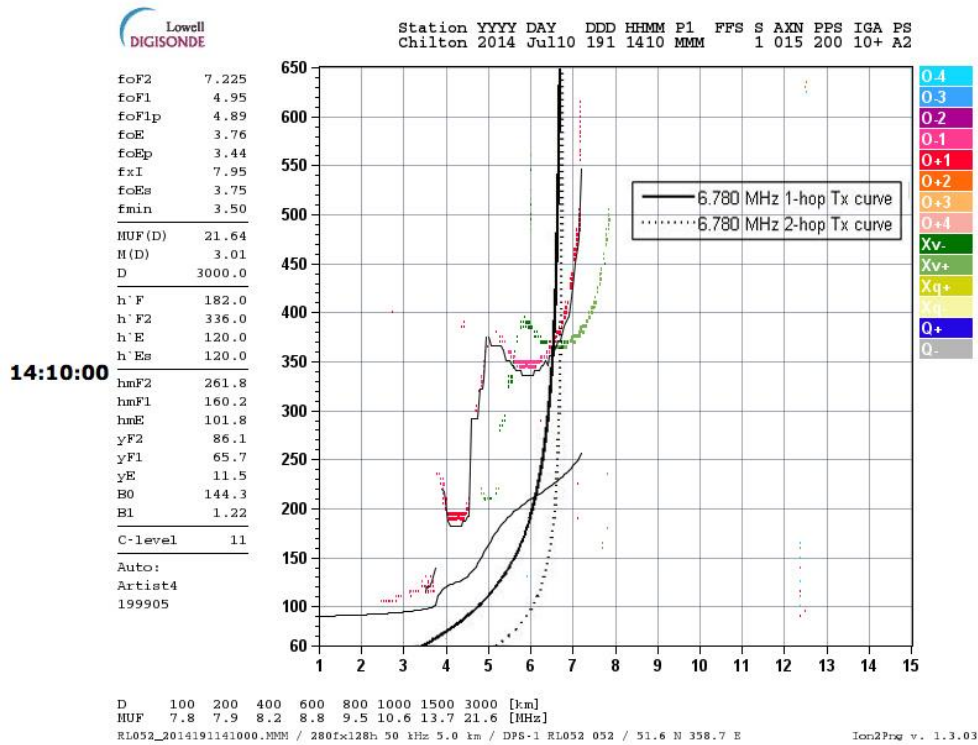


Figure 7.34 Vertical ionogram obtained from the Chilton ionosonde station superimposed on the 1-hop and 2-hop transmission curves (6.780 MHz) for the Bruntingthorpe-Lancaster path at 14:10 GMT on 10 July 2014.

Table 7.7 E-field right-hand circular polarization (O mode) phase information
for transmitting arrays (6.780 MHz) at 14:10 GMT on 10 July 2014

Unit (degree)	1-hop signal E-field (right hand) Phase (Zenith: 15°)	2-hop signal E-field (right hand) Phase (Zenith: 7°)	E-field (right hand) Phase Difference	E-field (right hand) PDD provide by the array
ORG-Lan	8.1	4.4	3.7	5.3
ORG-Cross	-3.2	-1.7	-1.6	
E2-Lan	-8.6	-5.7	-2.9	14.7
E2-Cross	-49.9	-32.3	-17.6	

Table 7.8 E-field left-hand circular polarization (X mode) phase information for
transmitting arrays (6.780 MHz) at 14:10 GMT on 10 July 2014

Unit (degree)	1-hop signal E-field (left hand) Phase (Zenith: 15°)	2-hop signal E-field (left hand) Phase (Zenith: 8°)	E-field (left hand) Phase Difference	E-field (left hand) PDD provide by the array
ORG-Lan	8.1	5.0	3.1	-2.2
ORG-Cross	8.5	3.2	5.3	
E2-Lan	-8.6	-6.2	-2.4	-20.8
E2-Cross	60.5	42.1	18.4	

Figure 7.35 presents the correlation coefficients variation with time for these two arrays. In the first 50 minutes of the test, the array elements decorrelation level of the array E2 is significantly lower than original crossed end-fed Vee array. Figure 7.36 displays the occurrence frequency histograms of the amplitude correlation coefficients between the array E2 antennas (E2-Lan and E2-Cross) and between the referenced array ORG antennas (ORG-Lan and ORG-Cross). The mean value of correlation coefficients for the array E2 and ORG were about 0.32 and 0.57, respectively. All the correlation coefficients are less than 0.9, which means that both of these two antenna arrays can meet the requirement of a successful MIMO system. It is worth noticing that: for the array E2, only 3.28% of correlation coefficients exceed 0.6. However, this value is 59% for the original crossed end-fed Vee array.

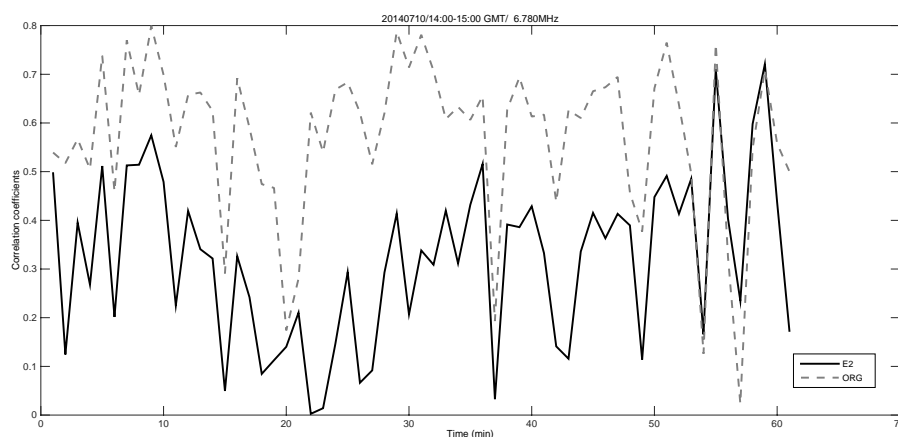


Figure 7.35 The Correlation coefficients variation with time. Four transmitting antennas sent CW signals at the same time with the transmission frequency 6.780 MHz.

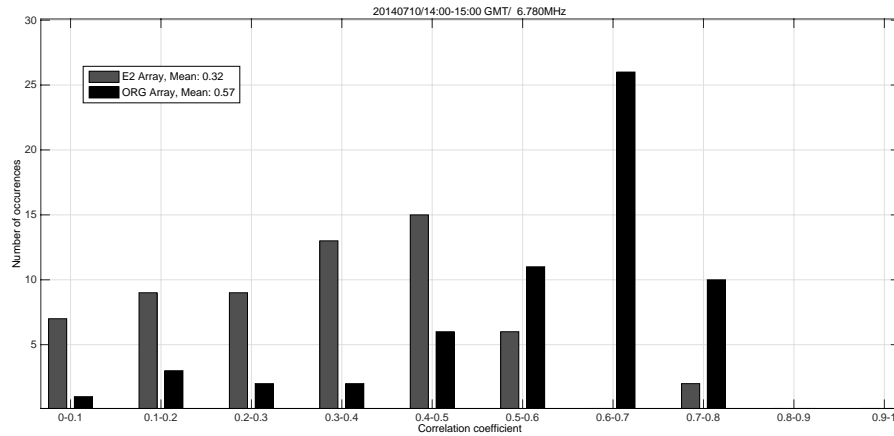


Figure 7.36 The occurrence frequency histograms of the correlation coefficients (of 58 s amplitude recodes) between newly designed heterogeneous antenna array E2 inter-elements (E2-Lan and E2-Cross) and original crossed end-fed Vee antenna array ORG inter-elements (ORG-Lan and ORG-Cross). 61 one-minute data files were collected and analysed from 14:00 GMT to 15:00 GMT.

7.2.6 Comparison of S2 and ORG in 4×1 MISO measurement

7.2.6.1 Experimental Arrangement

Another 4×1 campaign was conducted on 16 July 2014. The heterogeneous antenna array S2 was employed instead of the array E2 to investigate the decorrelation level between the array elements. The ORG array was utilized as referenced antenna array as previous campaigns. The array S2 is evolved from the array E2 with four vertical wire elements of the E2-Lan arm removed. Other parameters were same with the last experiment. The transmission nominal

frequency was set to 6.780 MHz and 10 Hz was selected as offset frequency (ORG-Lan: 6.780000 MHz; ORG-Cross: 6.780010 MHz; S2-Lan: 6.780030 MHz; S2-Lan: 6.780040 MHz).

7.2.6.2 Results and Discussion

The campaign was carried out between 9:20 GMT and 10:30 GMT. 71 one-minute data files were collected and analysed. One frame (58 second) of received signals was displayed in Figure 7.37. The amplitude correlation coefficient for the received signals sent by the array S2 and ORG is 0.27 and 0.69 in this particular frame, respectively.

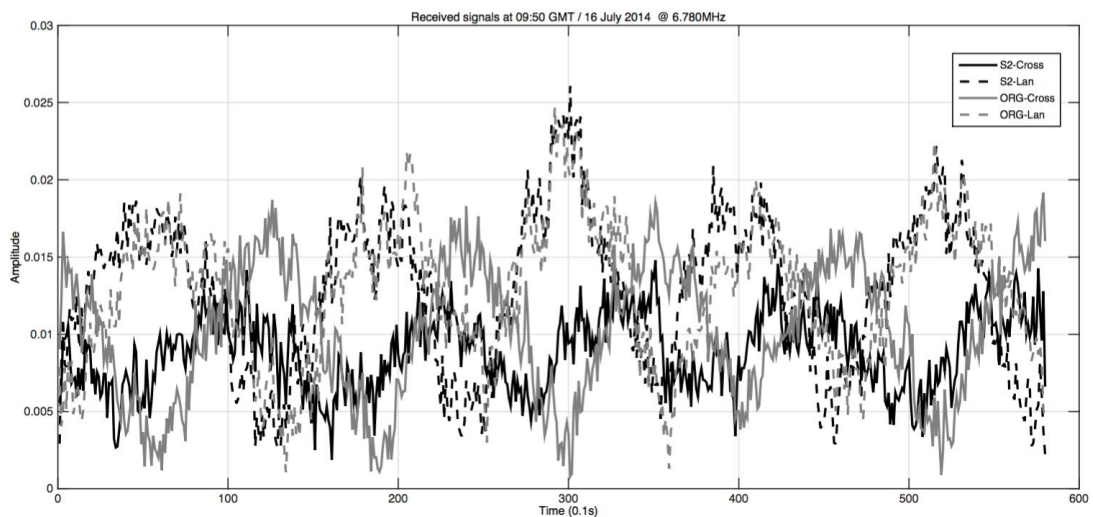


Figure 7.37 Received signals (58 second) at 09:50 GMT on 16 July 2014. The absolute value of amplitude correlation coefficient between the inter-elements of the newly designed array S2 (S2-Lan and S2-Cross) and referenced array ORG (ORG-Lan and ORG-Cross) is 0.27 and 0.69, respectively.

The ionogram corresponding to the period overlaid with transmission curves corresponding to 6.780 MHz is displayed in Figure 7.38. The 1-hop and 2-hop signal was reflected at virtual height approximately 320 km and 340 km respectively via the ionospheric O mode; for X mode propagation, the virtual reflection height was nearly 320 km for both 1 and 2 hop signals. Considering the radio link distance, it can be deduced that: the launched zenith angle was 18° and 8° for 1-hop and 2-hop signal under O mode propagation; 18° and 9° under X mode transmission. Combining with the left and right hand circular polarization phase map of the array S2 and ORG displayed in Section 7.1.5 (see Figure 7.17 and 7.18), the phase difference difference produced by the arrays inter-elements were showed in Table 7.9 and 7.10. Under the prevailing ionospheric conditions, the inter-elements of newly designed array S2 produced nearly 15.7° phase difference difference via O mode propagation, which was greater than the corresponding value (5.9°) generated by the referenced array ORG. For X mode propagation, the phase difference difference produced by the array ORG was only -4.7° . This index significantly increased to -30.1° for the new array S2. As a result, the antenna array S2 can generate more phase difference difference compared to the array ORG, which means that the signals from inter-elements of the array S2 are more decorrelated. This is consistent with the result of the experiment.

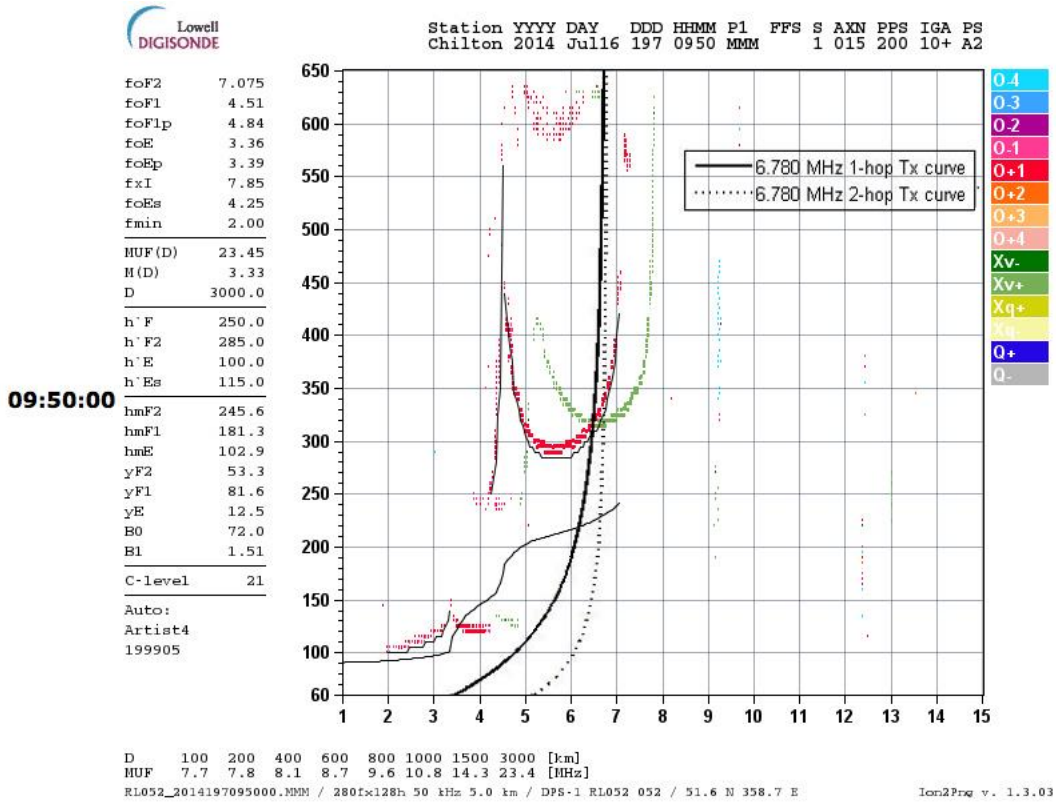


Figure 7.38 Vertical ionogram obtained from the Chilton ionosonde station superimposed by a 1-hop and 2-hop transmission curves (6.780 MHz) for the Bruntingthorpe-Lancaster path at 09:50 GMT on 16 July 2014.

Table 7.9 E-field right-hand circular polarization (O mode) phase information for transmitting arrays (6.780 MHz) at 09:50 GMT on 16 July 2014

Unit (degree)	1-hop E-field hand) (Zenith: 18°)	signal (right Phase	2-hop E-field hand) (Zenith: 8°)	signal (right Phase	E-field hand) Phase Difference	E-field (right hand) PDD provide by the array
ORG-Lan	9.1		5.0		4.1	5.9
ORG-Cross	-3.7		-1.9		-1.8	
S2-Lan	10.8		6.0		4.8	15.7
S2-Cross	-30.7		-19.8		-10.9	

Table 7.10 E-field left-hand circular polarization (X mode) phase information for transmitting arrays (6.780 MHz) at 09:50 GMT on 16 July 2014

Unit (degree)	1-hop signal E-field (left hand) Phase (Zenith: 18°)	2-hop signal E-field (left hand) Phase (Zenith: 9°)	E-field (left hand) Phase Difference	E-field (left hand) PDD provide by the array
ORG-Lan	9.1	5.5	3.6	-4.7
ORG-Cross	12.1	3.8	8.3	
S2-Lan	10.8	6.6	4.2	-30.1
S2-Cross	91.7	57.4	34.3	

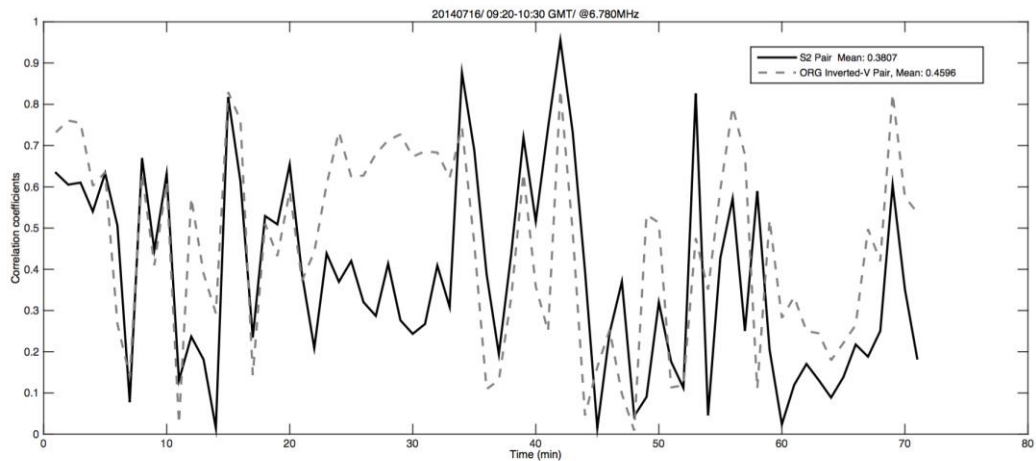


Figure 7.39 The time-varying magnitude correlation coefficients generated by the inter-elements of the S2 array and ORG array. Data collection was carried out between 9:20 GMT and 10:30 GMT on 16 July 2014. The mean value of correlation coefficients produced by the S2 array and the ORG array was 0.38 and 0.46 respectively.

Figure 7.39 displays the time-varying magnitude correlation coefficients generated by the inter-elements of the S2 array and ORG array. The mean value of correlation coefficients of the array E2 and ORG array were about 0.38 and 0.46, respectively. The occurrence frequency histograms of the amplitude correlation coefficients between inter-elements of S2 and ORG are presented in Figure 7.40. As mentioned before, 0.7 is usually considered as the threshold value for signals being independent of each other. As a result, both of these two heterogeneous antenna arrays can meet the requirement of a successful MIMO system. Further comparison showed that nearly 90% and 76% correlation coefficients produced by E2 inter-elements were less than 0.7 and 0.6, respectively. However, these indices reduced to 83% and 63% for the referenced array ORG. As a result, the array S2 can produce more decorrelated signals than the ORG array.

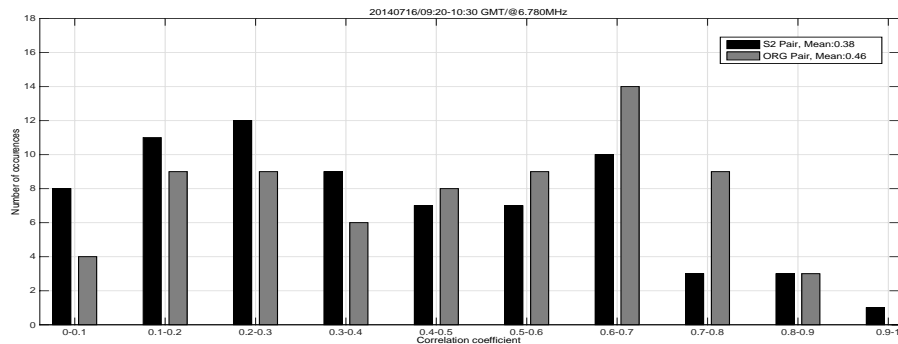


Figure 7.40 The occurrence frequency histograms of the correlation coefficients (of 58 s amplitude recodes) between the array S2 inter-elements (S2-Lan and S2-Cross) and original crossed end-fed Vee antenna array ORG inter-elements (ORG-Lan and ORG-Cross). 71 one-minute data files were collected and analysed from 09:20 GMT to 10:30 GMT.

7.2.7 Comparison of NPT and ORG in 4×1 MISO measurement

In previous campaigns, phase difference diversity was achieved by adding vertical stainless steel wire elements on the arm of the antennas. The Non-Planar Twisted antenna array is also designed to increase phase difference. This antenna differs from previous designs in that it is non-coplanar.

7.2.7.1 Experiment Arrangement

A 4×1 MISO experiment was conducted on 31 July 2014 with the Non-Planar Twisted (NPT) antenna array and referenced ORG at the transmitting site. Four CW signals were transmitted simultaneously with the nominal frequency 6.780 MHz (NPT-Lan: 6.780000 MHz; NPT-Cross: 6.780010 MHz; ORG-Lan: 6.780020 MHz; ORG-Cross: 6.780030 MHz). At the receiver, a 5 m high whip antenna was used to pick up signals same as previous measurements.

7.2.7.2 Results and Discussion

The campaign was conducted between 14:40 GMT and 16:00 GMT. 81 one-minute data files were collected and analysed. One frame (58 second) of received signals was displayed in Figure 7.41. The amplitude correlation coefficient for the received signals sent by the array NPT and ORG is 0.69 and 0.93 in this particular frame, respectively.

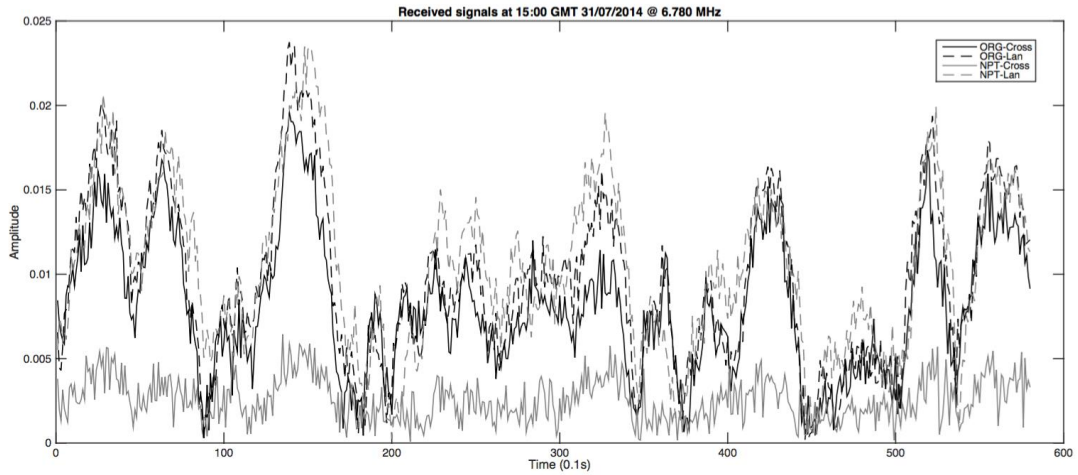


Figure 7.41 Received signals (58 second) at 15:00 GMT on 31 July 2014.

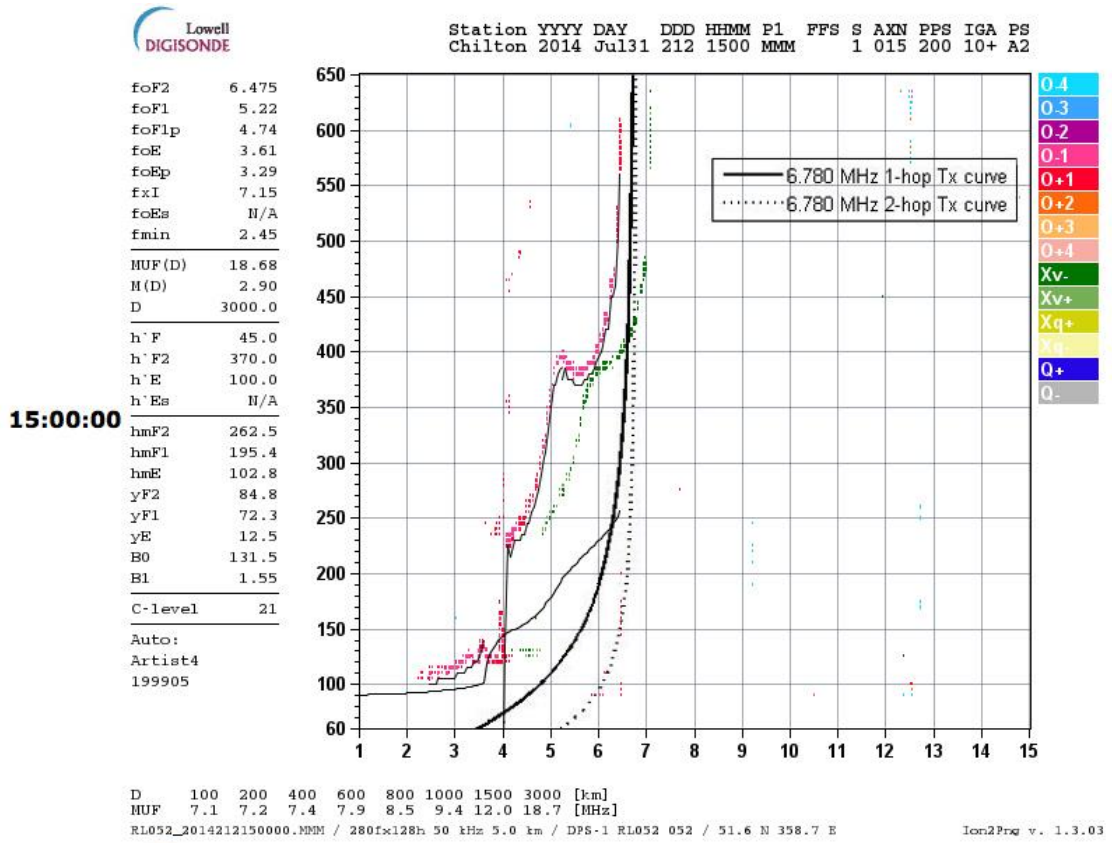


Figure 7.42 Vertical ionogram obtained from the Chilton ionosonde station superimposed by a 1-hop and 2-hop transmission curves (6.780 MHz) for the Bruntingthorpe-Lancaster path at 15:00 GMT on 31 July 2014.

The ionogram corresponding to the moment obtained from Chilton station is shown in Figure 7.42. After being overlaid with the transmission curves 6.780 MHz, the transmission mode and signal virtual reflection height can be found. Under the prevailing ionospheric condition, only X mode (left-hand circular polarization in NEC coordination system) can support the transmission with 6.780 MHz. The virtual reflection height was 410 km and 430 km for 1-hop and 2-hop signal, respectively. Considering the transmission distance, the launched zenith angle for 1-hop and 2-hop signal can be deduced as 14° and 7°. Combining with left-hand circular polarization phase map of the NPT and ORG array, the phase difference difference produced by these two arrays under the prevailing ionospheric condition was displayed in Table 7.11. The phase difference difference for the newly designed NPT array was about 13.2° which is significantly greater than the ORG array (-1.5°) via X mode propagation.

Table 7.11 E-field left-hand circular polarization (X mode) phase information for transmitting arrays (6.780 MHz) at 15:00 GMT on 31 July 2014.

Unit (degree)	1-hop signal E-field (left hand) Phase (Zenith: 14°)	2-hop signal E-field (left hand) Phase (Zenith: 7°)	E-field (left hand) Phase Difference	E-field (left hand) PDD provide by the array
ORG-Lan	7.8	4.4	3.4	-1.5
ORG-Cross	7.5	2.6	4.9	
NPT-Lan	9.3	5.4	3.9	13.2
NPT-Cross	-14.5	-5.2	-9.4	

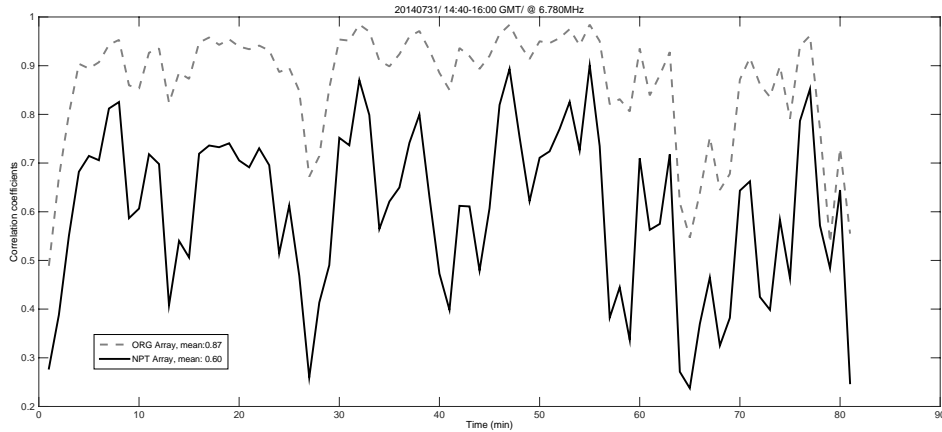


Figure 7.43 The time-varying magnitude correlation coefficients generated by the inter-elements of the NPT array and ORG array. Data collection was carried out between 14:40 GMT and 16:00 GMT on 31 July 2014. The mean value of correlation coefficients produced by the NPT array and the ORG array was 0.60 and 0.87 respectively.

Figure 7.43 shows the correlation coefficients variation with time. It is worth noticing that the correlation coefficients generated by the newly designed NPT array were less than that of the ORG array at all times during the campaign. Figure 7.44 showed the occurrence frequency histograms of the correlation coefficients produced by the inter-elements of the Non-Plane Twisted antenna array and ORG array. There were about 48.1% and 18.5% of correlation coefficients less than 0.9 and 0.7 respectively for the original crossed end-fed Vee array. For the newly designed NPT antenna array, these indices increased significantly to 98.7% and 90.1% respectively. The mean value of correlation coefficients produced by the NPT array inter-elements was 0.60, which was obviously less than the

corresponding value 0.87 generated by the ORG array inter-elements. As a result, signals from the newly designed NPT array are more decorrelated than original end-fed Vee array under the prevailing ionospheric conditions.

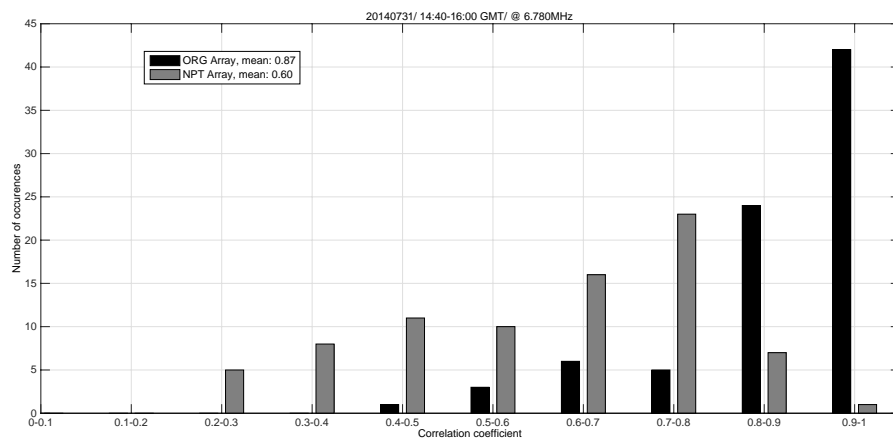


Figure 7.44 The occurrence frequency histograms of the correlation coefficients (of 58 s amplitude recodes) between the newly designed NPT array inter-elements (NPT-Lan and NPT-Cross) and original crossed end-fed Vee antenna array inter-elements (ORG-Lan and ORG-Cross). 81 one-minute data files were collected and analysed from 14:40 GMT to 16:00 GMT.

7.3 Summary

Five novel antenna arrays (T1, T2, E2, S2, NPT) have been designed according to the PDD assumption in Section 4.2. The modelling simulations show that the newly designed antenna arrays can generate more phase difference difference at modelled frequency both in O and X mode compared with reference antenna array ORG, which showed a good decorrelation level in previous campaigns. Furthermore, the experimental measurements showed that these novel antenna arrays had a lower correlation level between array elements than the ORG array, which demonstrated that the correlation level of antenna array employed in MIMO systems can be reduced by increasing PDD of the array. Besides these five novel antenna arrays, same antenna arrays with opposite power feed were also tested in the campaigns, which demonstrated the corresponding relationship between ‘O and X mode’ and ‘left and right hand polarization’ in NEC modelling system. Table 7.12 summarized these arrays’ PDD and mean value of correlation coefficients in previous campaigns. Figure 7.45 and 7.46 displays the correlation coefficients changing with left and right hand polarization PDD, respectively. For both modes, with the increased PDD, the correlation between antenna array elements are significantly reduced. As a result, phase difference difference, as a kind of pattern diversity, can be utilized as a new MIMO diversity in the future antenna design and optimisation. Compared with spatial diversity, PDD diversity can significantly reduce the space requirement for MIMO application, especially for HF band.

Table 7.12 Novel antenna arrays phase difference difference (PDD) and corresponding mean value of amplitude correlation coefficients during experiments.

	Antenna array	Phase difference difference of antenna array (PDD) (degree)		Mean value of amplitude correlation coefficients
		Left-hand (X mode)	Right-hand (O mode)	
Campaign	ORG	-1.5	4.8	0.83
27/06/13	T1	7.5	10.4	0.72
Campaign	ORG	-1.5	4.8	0.93
03/07/13	T2	4.4	5.6	0.82
Campaign	ORG	-1.5	4.8	0.57
10/07/14	E2	-23.4	13.7	0.32
Campaign	ORG	-1.5	4.8	0.46
16/07/14	S2	-33.7	13.6	0.38
Campaign	ORG	-1.5	4.8	0.87
31/07/14	NPT	13.2	8.7	0.60

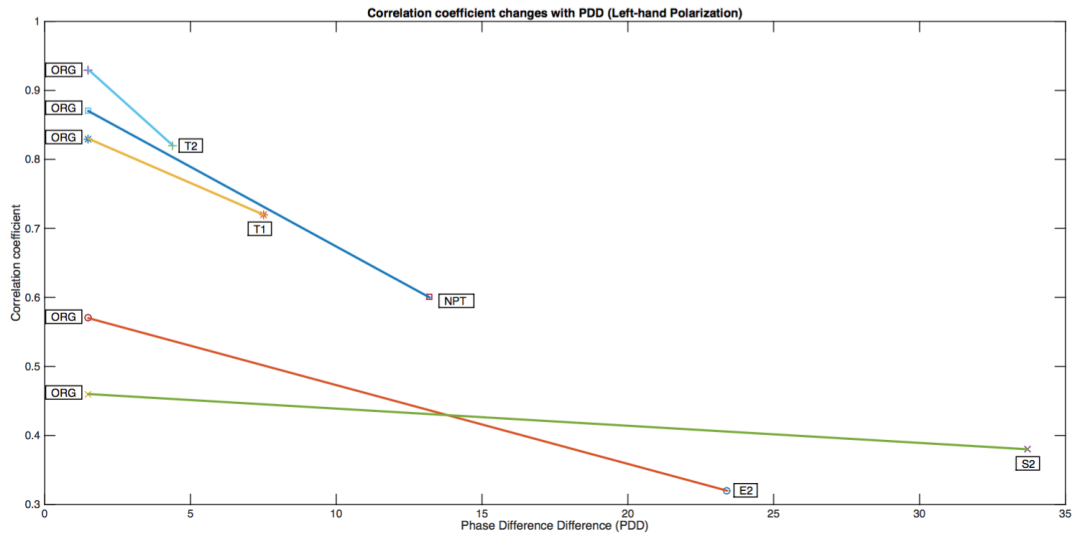


Figure 7.45 Correlation coefficient changes with PDD based on left-hand polarization

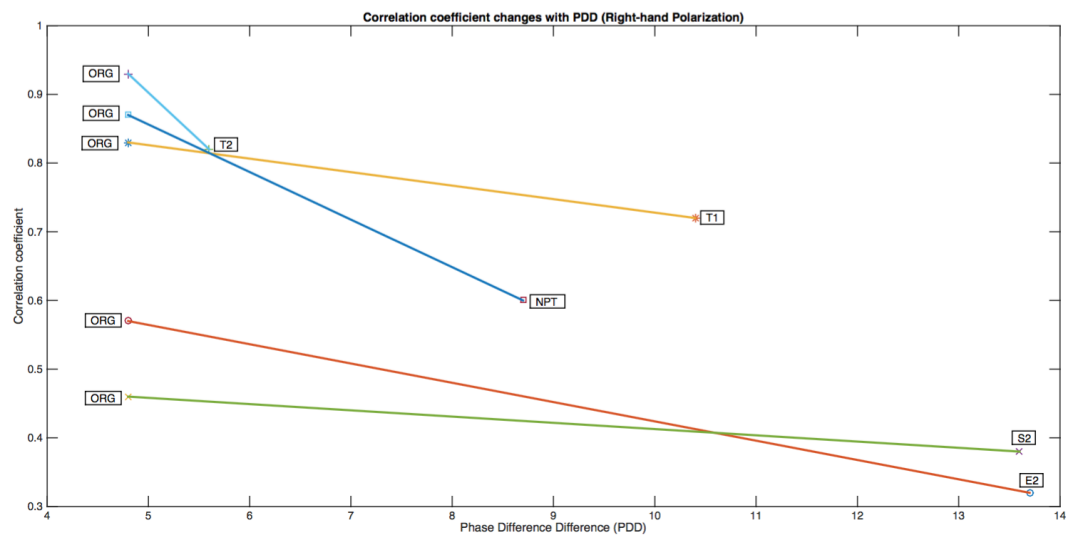


Figure 7.46 Correlation coefficient changes with PDD based on right-hand polarization

Chapter 8 Antenna modelling using High Performance Computing (HPC)

In order to better understand the relationship between antenna array geometry and phase difference difference, the universities high performance computing cluster is employed to process and analyse millions of different antenna arrays. The optimized antenna array geometries were recommended according to obtain greater PDD in this chapter.

8.1 HPC-Alice

Alice is the high-performance computing cluster provided by the University of Leicester, which is one of the most powerful computing systems in a UK University. It can provide modelling and simulations, data processing and analysis etc services based on Linux environment. Alice has 208 standard computer nodes. Each standard node consists of a pair of eight-core Intel Xeon Ivy Bridge CPUs running at 2.6 GHz. The storage space of Alice is approximately 550 TB provide by Panasas storage system. Once Alice received a task, the scheduler will automatically decide which compute node the task should use, depending on the requirement of the task and available resources.



Figure 8.1 High Performance Computing Cluster – Alice in University of Leicester

8.2 Modelling program construction on HPC

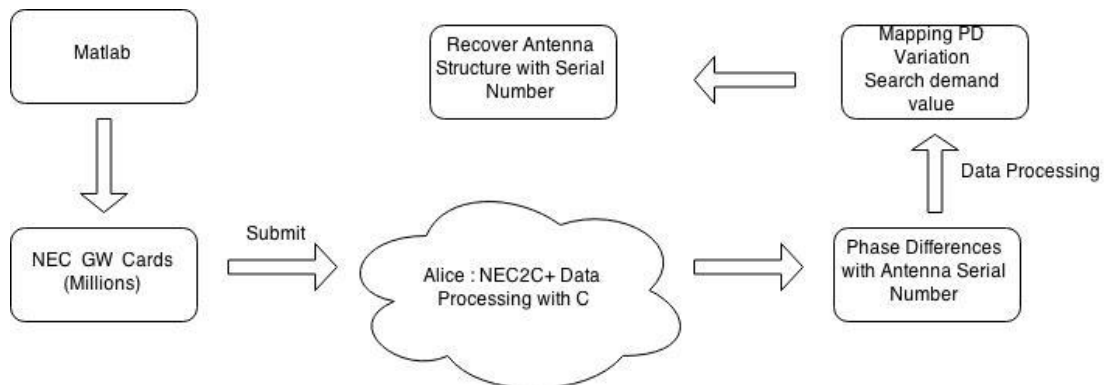


Figure 8.2 Modelling program constructions

Millions of NEC standard input cards (GW) are generated by Matlab on a single node on Alice. Each card is marked with a serial number. Every 100000 NEC cards are packaged into an input-file folder to feed NEC2C on Alice. Thousands of nodes on Alice will process these input files and generate standard NEC output files.

Then a program is used to extract the relevant information from the NEC output file and calculate the phase difference between zenith angle 7° and 14° for the left and right hand polarization respectively. In order to enhance the processing speed, the program is written in C language instead of Matlab. After phase difference calculation, these results with related antenna serial number are collected from Alice nodes and written into a single file. By combining the phase differences produced by different antenna array elements, the phase difference difference can be deduced for the array. The left and right hand phase difference differences are plotted with antenna array serial number. Then a program will start to search the wanted values among PDD data. For different polarizations, the antenna array which its geometry can generate PDD (absolute value) has the minimum difference with 90° is recommended. Furthermore, in order to obtain most PDD for both left and right hand polarizations, the trade-off antenna array is also recommended. The geometry of the optimum antenna array can be recovered conveniently by using its serial number.

8.3 Optimized collocated heterogeneous antenna array

The optimum collocated antenna array is still based on original crossed end-fed Vee antenna array. According to previous modelling work (Chapter 7), the PDD of the array can be altered by adding vertical stainless steel wires on the antennas. Previously, these wires were spaced apart by $1/8$ or $1/6$ of the antenna length and

connect the antenna with ground. In order to investigate how the wire-element positions on the antenna affect the array phase difference difference, a single position-adjustable wire-element was used in the primary modelling (named with IV-1E) with different moving steps. Then two position-adjustable wire-elements were added on the antenna array elements (named with IV-2E) with a fixed moving step 50 cm. The calculation amount has reached millions level for IV-2E.

8.3.1 IV-1E

The main structure of IV-1E is same with ORG array: for the antenna pointed to Lancaster, it is located in x-axis from -15.5 m to +15.5 m; for the antenna perpendicular to the direction of transmission, it is put in y-axis from -15.5 m to +15.5 m. Except that, for each antenna, there is a moving vertical wire-element connecting the antenna with ground. The program set the wire-element on y-axis moving first, starting at $y=15.0$ m. After it moves to the other end ($y=-15.0$ m), then the wire-element on x-axis can move a step forward (start at $x=-15.0$ m). After that, the wire-element on y-axis gets back to starting point ($y=+15.0$ m) and move to the ending point again. Once the wire-element on x-axis arrived the other end ($x=15.0$ m), the loop on y-axis will be stopped and the modelling is finished.

8.3.1.1 IV-1E with step 50cm

The number of modelling calculation depends on the step size. Due to the moving distance on Y-axis is 30 m, as well as in X-axis, if the moving step is set to be 50cm, it will take 60 steps for the loop on Y-axis. For the wire-element on X-axis, it also needs 60 steps moving from one end of the antenna to the other. As a result, there will be approximately 3600 different antenna array geometry combinations. Figure 8.3 and 8.4 shows the left and right hand phase difference difference map changing with the serial number of the antenna arrays, respectively, with modelling frequency 5.255 MHz. According to the definition of correlation coefficient, if the signals amplitude ratio is a constant, the signals will not be correlated (correlation coefficient become 0) when the phase difference of these two signals reaches 90° . If there is no phase difference, the correlation coefficient become +1, which means these two signals are total positive correlation. If phase difference is 180° , the correlation become -1 and the signals are total negative correlation. As a result, the most ideal PDD of the array should be near 90° . After zoom in the PDD maps, the antenna arrays which can provide the nearest absolute values to 90° can be found according to serial numbers. The 2D PDD maps are displayed separately according to different polarization modes and modelling frequencies (see Figure 8.3 to 8.10).

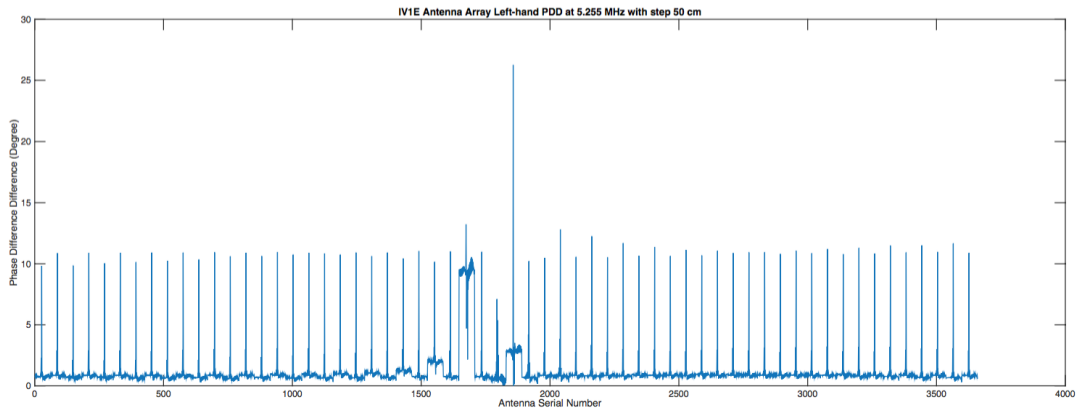


Figure 8.3 IV-1E left-hand PDD with step 50 cm modelling at 5.255 MHz

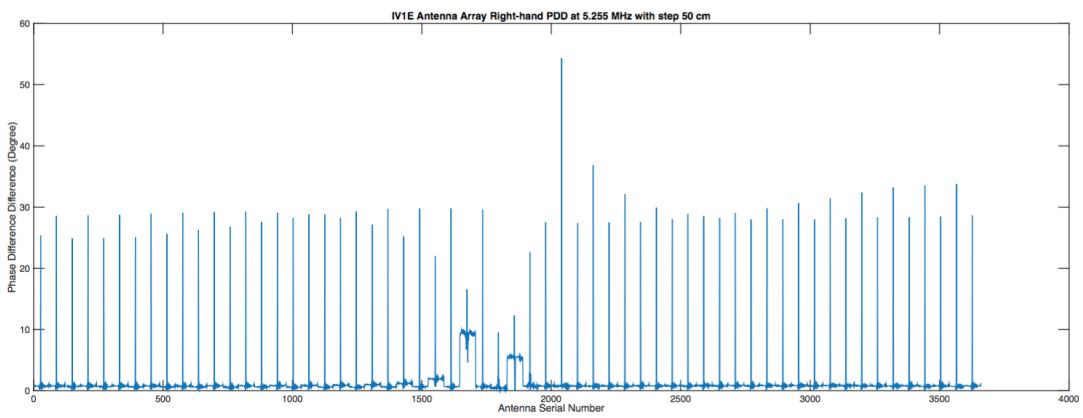


Figure 8.4 IV-1E right-hand PDD with step 50 cm modelling at 5.255 MHz

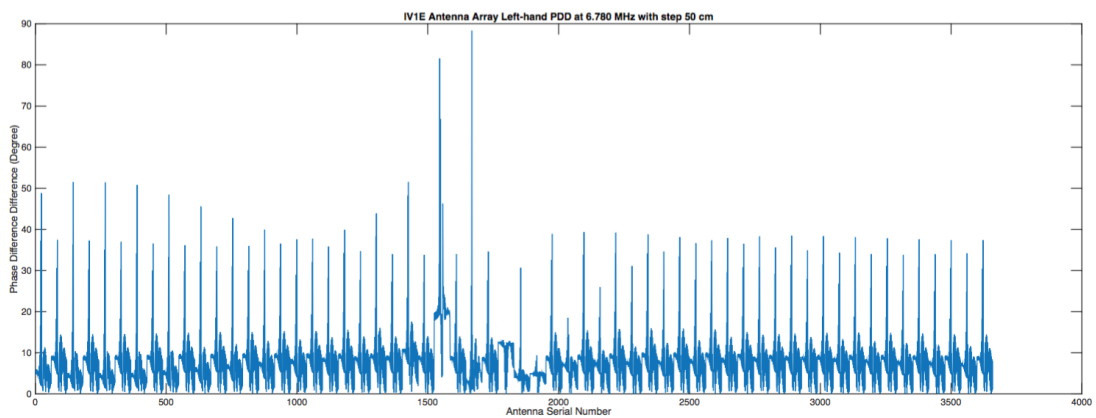


Figure 8.5 IV-1E left-hand PDD with step 50 cm modelling at 6.780 MHz

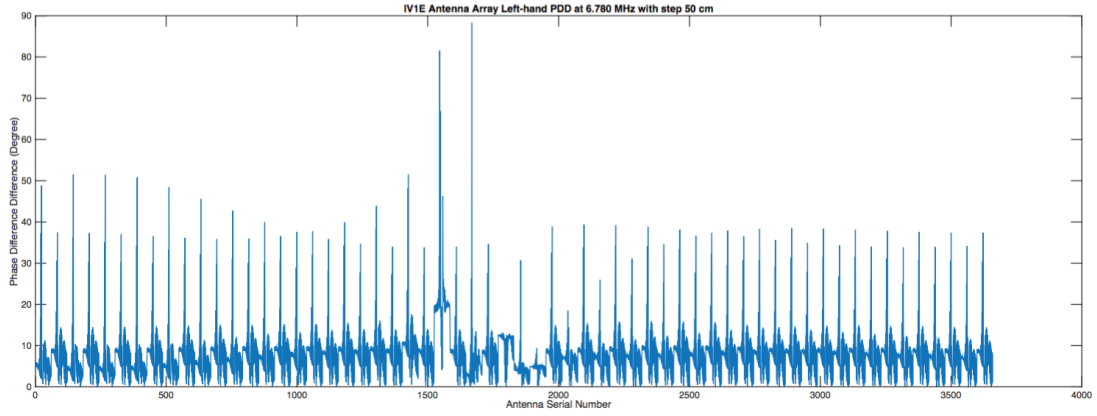


Figure 8.6 IV-1E right-hand PDD with step 50 cm modelling at 6.780 MHz

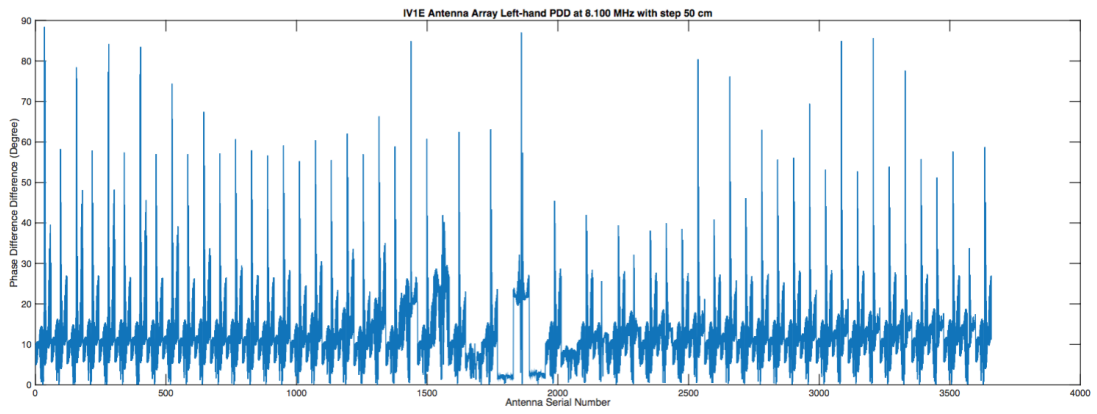


Figure 8.7 IV-1E left-hand PDD with step 50 cm modelling at 8.100 MHz

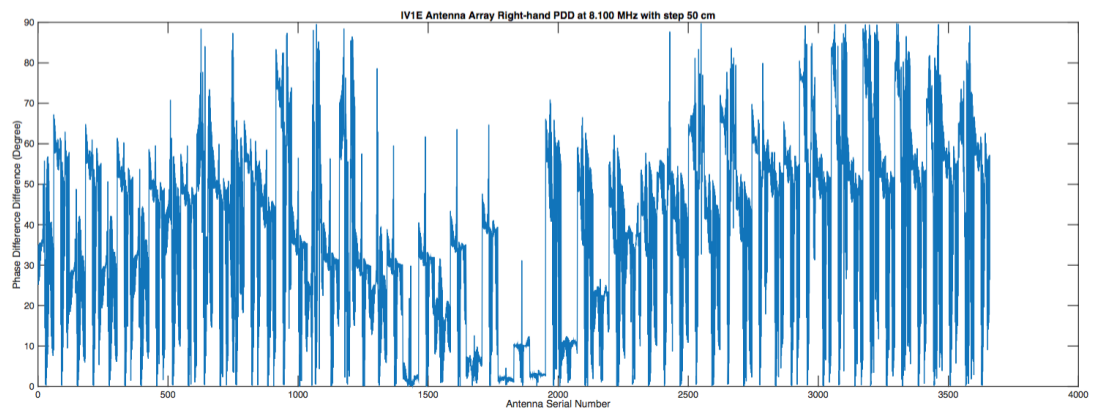


Figure 8.8 IV-1E right-hand PDD with step 50 cm modelling at 8.100 MHz

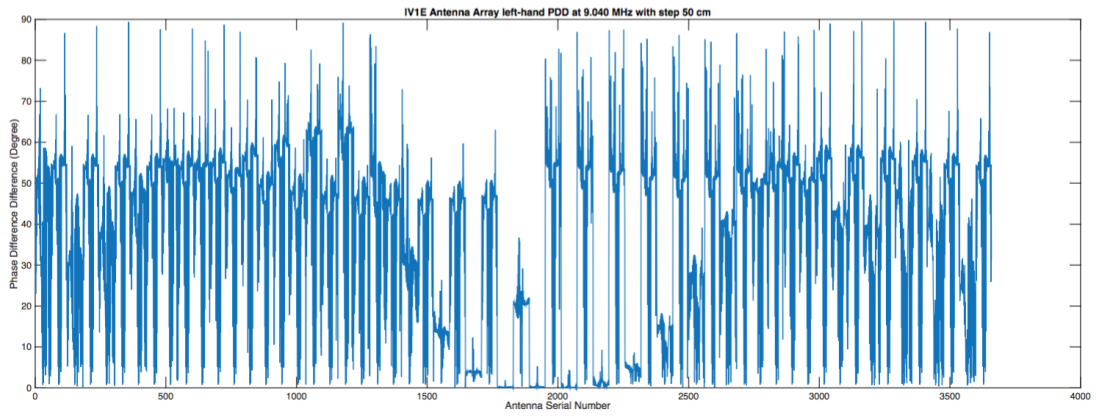


Figure 8.9 IV-1E left-hand PDD with step 50 cm modelling at 9.040 MHz

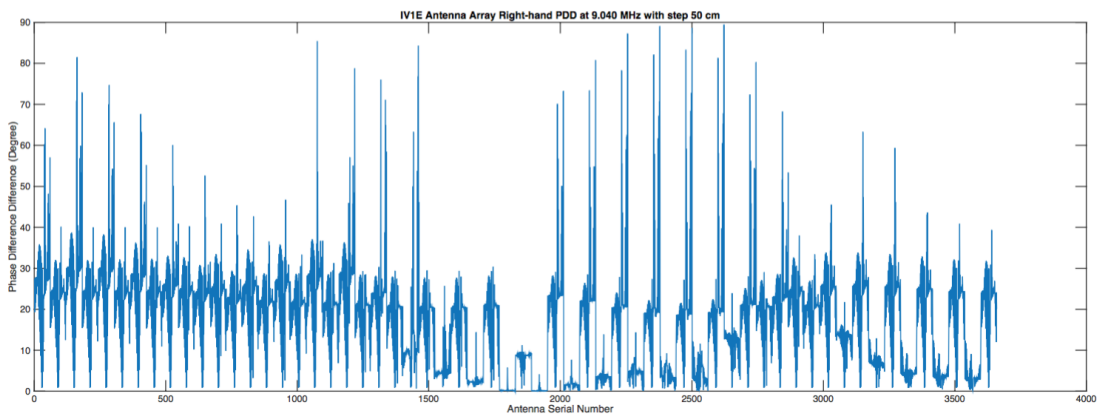


Figure 8.10 IV-1E right-hand PDD with step 50 cm modelling at 9.040 MHz

Table 8.1 and 8.2 summarized the recommended antenna array serial number and corresponding PDD for different polarization modes and modelling frequencies after program searched in these PDD maps. Some of maximum PDD were abandoned due to unreasonable antenna array geometry. For instance, the maximum left-hand PDD is 26.3° generated by the antenna array ‘1857’ at 5.255 MHz. However, for the antenna array ‘1857’, the vertical wire element on the antenna ORG-LAN overlays with support mast and connect with the other array elements. As a result, the antenna array ‘1857’ is abandoned. The secondly maximum left-hand PDD is 12.8°, which is generated by the antenna array ‘2040’ (see Table 8.1 and 8.2). The geometry of related antenna arrays are displayed from Figure 8.11 to 8.17.

Table 8.1 Recommended antenna array serial numbers for IV-1E (step 50 cm)

Frequency	Left hand (X)	Right hand (O)
5.255 MHz	2040	2040
6.780 MHz	1668	2160
8.100 MHz	35	3302
9.040 MHz	3285	2622

Table 8.2 Recommended antenna arrays PDD for IV-1E (step 50 cm)

Frequency	Left hand (X)	Right hand (O)
5.255 MHz	12.8°	54.4°
6.780 MHz	88.3°	61.2°
8.100 MHz	88.4°	89.8°
9.040 MHz	89.7°	89.5°

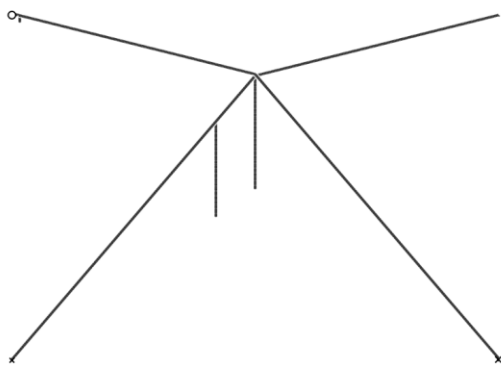


Figure 8.11 Antenna array '35'

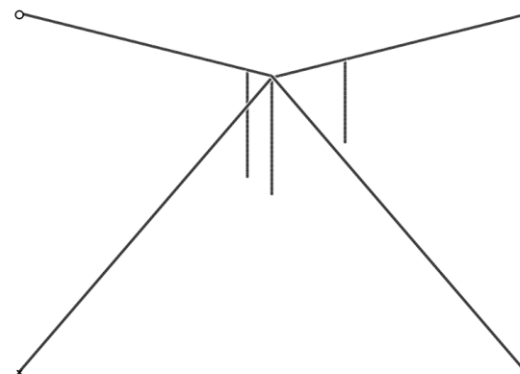


Figure 8.12 Antenna array '1668'

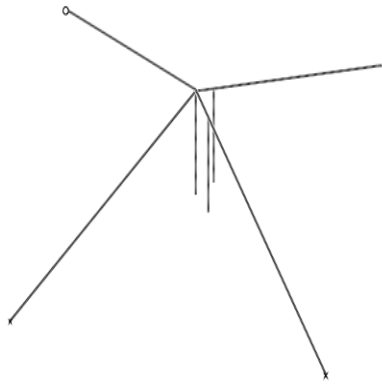


Figure 8.13 Antenna array '2040'

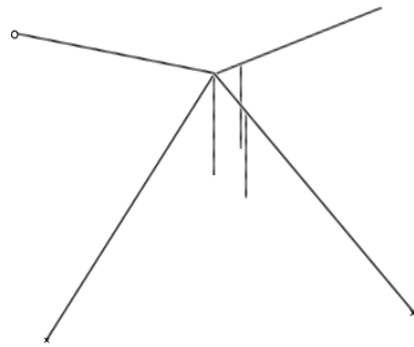


Figure 8.14 Antenna array '2160'

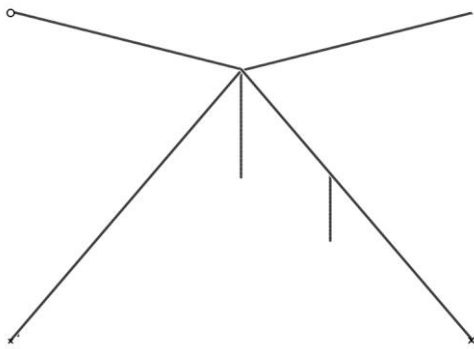


Figure 8.15 Antenna array '2622'

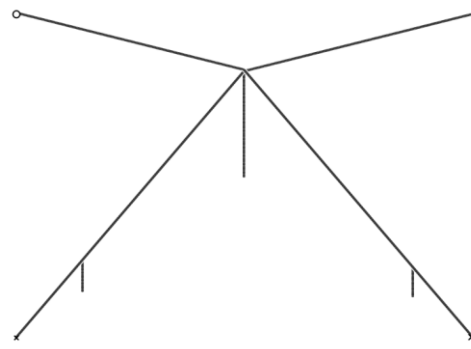


Figure 8.16 Antenna array '3285'

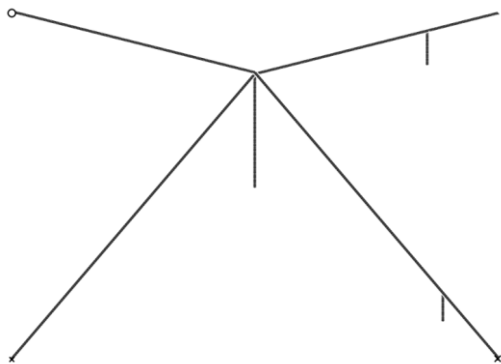


Figure 8.17 Antenna array '3302'

In order to investigate the relationship between PDD and adjustable vertical wire elements positions, 3D maps of PDD corresponding to coordinates are plotted. Figure 8.18 and 8.19 shows the left and right hand polarization 3D PDD maps modelling at 5.255 MHz with moving step 50 cm, respectively. For the left hand polarization PDD, it is worth to notice that when wire element of 'Cross' (in Y direction) moves to 'y= 1.5 m' or 'Lan' wire element (in X direction) moves to 'x=-1.5 m', the PDD can have a significantly increase. Furthermore, the maximum PDD (peak point in Figure 8.18) is 26.3° generated by antenna array '1857' which is abandoned due to its structure overlays with the mast.

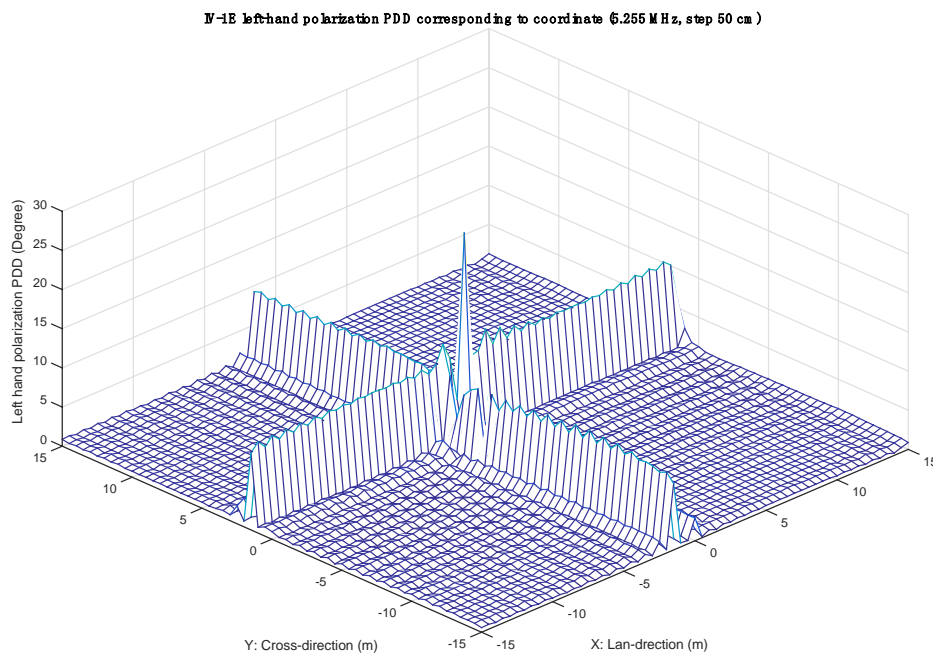


Figure 8.18 3D map of IV-1E left-hand polarization PDD corresponding to coordinate, modelling at 5.255 MHz with moving step 50 cm.

IV-1E right-hand polarization PDD corresponding to coordinate (5.255 MHz, step 50 cm)

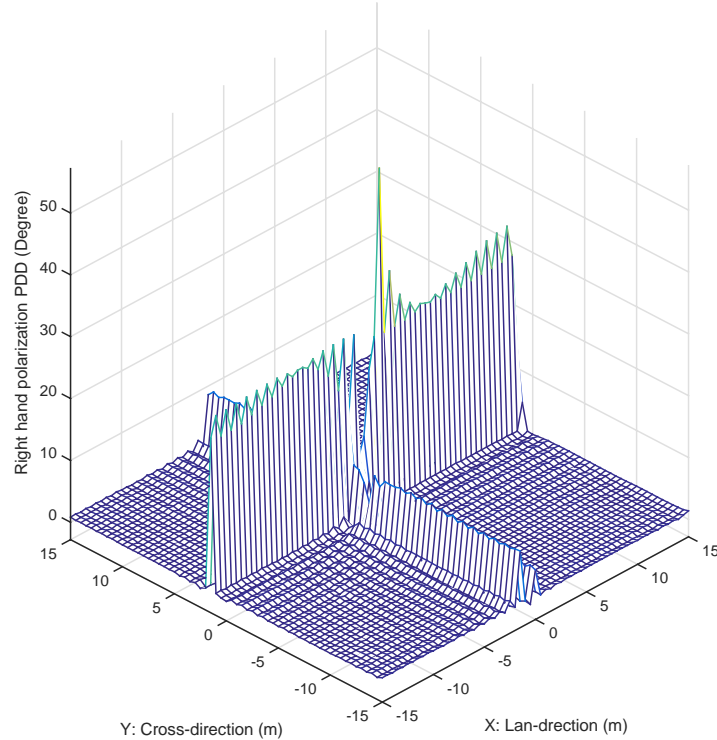


Figure 8.19 3D map of IV-1E right-hand polarization PDD corresponding to coordinate, modelling at 5.255 MHz with moving step 50 cm.

Meanwhile, when the 'Cross' wire element moves to 'y=1.5 m', the PDD can increase nearly 27° on average for the right hand polarization. And the PDD reaches to the maximum value 54° when 'Lan' wire element moves to 'x=1.5 m'. This geometry is corresponding to antenna serial number 2040. Figure 8.20 to 8.25 presents the 3D maps of IV-1E with moving step 50 cm for other modelling frequencies.

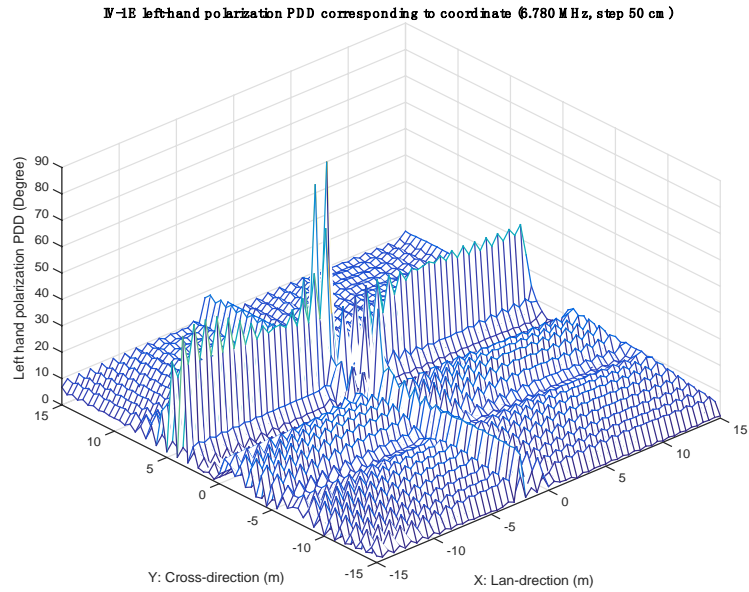


Figure 8.20 3D map of IV-1E left-hand polarization PDD corresponding to coordinate, modelling at 6.780 MHz with moving step 50 cm.

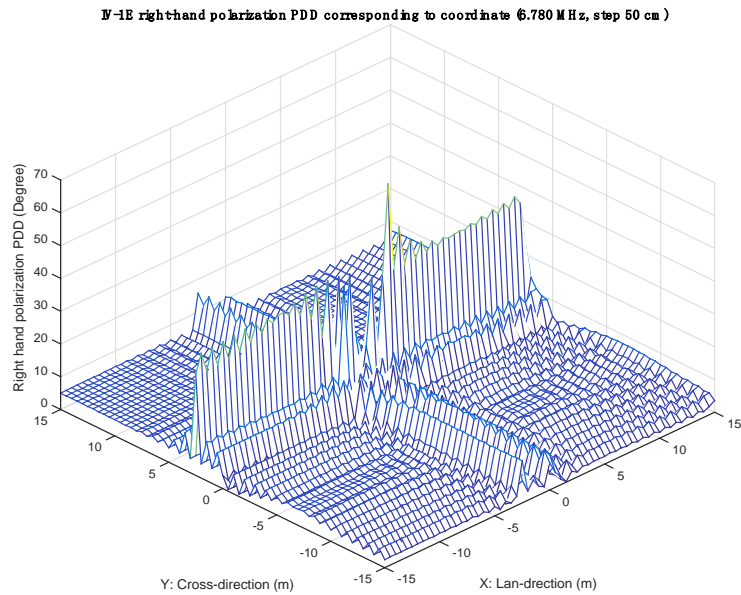


Figure 8.21 3D map of IV-1E right-hand polarization PDD corresponding to coordinate, modelling at 6.780 MHz with moving step 50 cm.

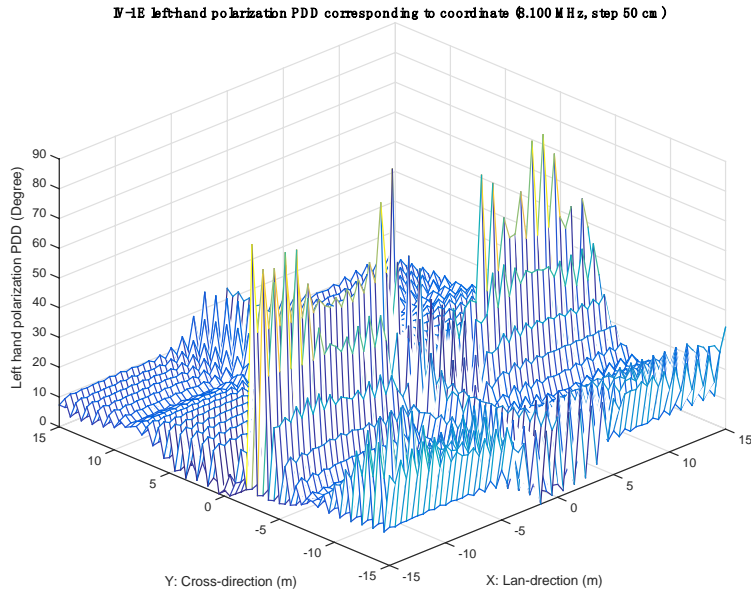


Figure 8.22 3D map of IV-1E left-hand polarization PDD corresponding to coordinate, modelling at 8.100 MHz with moving step 50 cm.

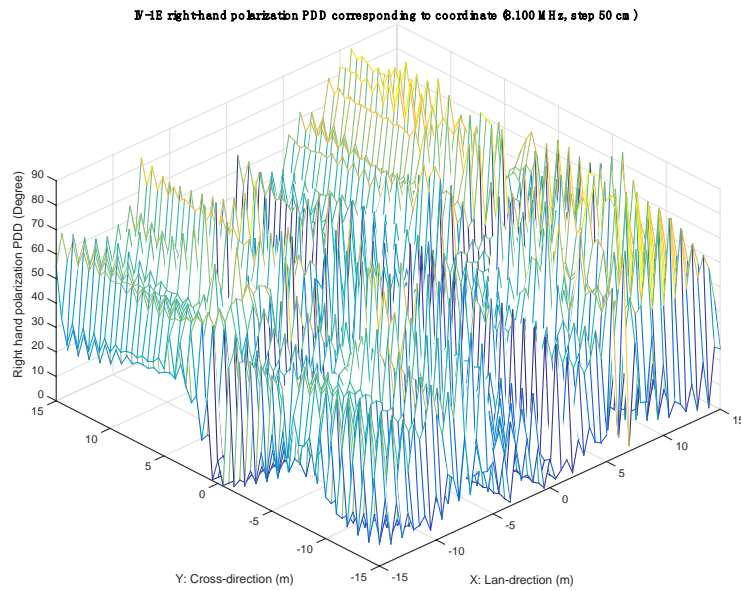


Figure 8.23 3D map of IV-1E right-hand polarization PDD corresponding to coordinate, modelling at 8.100 MHz with moving step 50 cm.

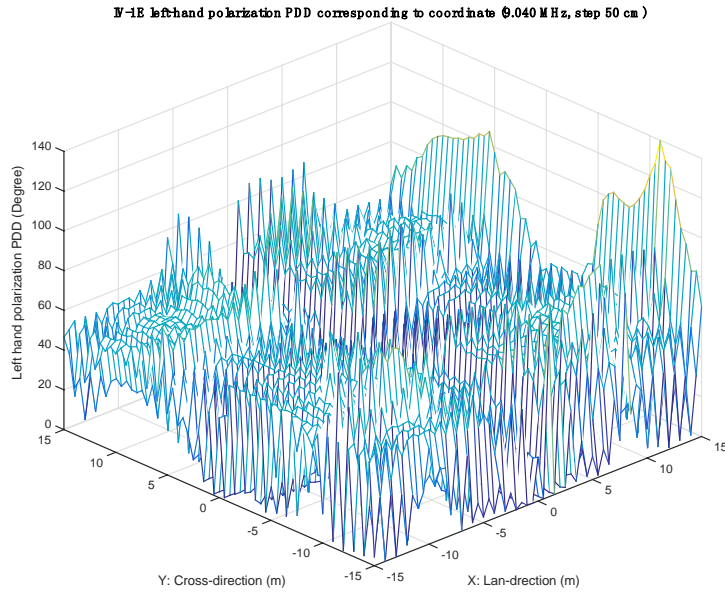


Figure 8.24 3D map of IV-1E left-hand polarization PDD corresponding to coordinate, modelling at 9.040 MHz with moving step 50 cm.

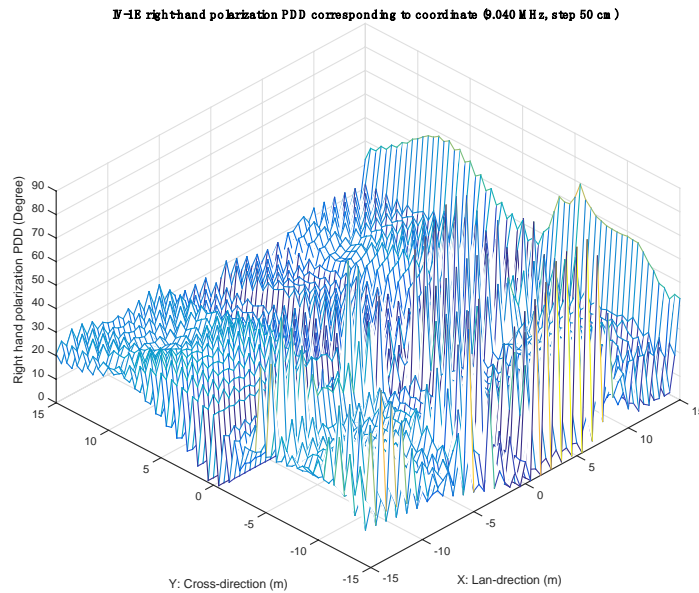


Figure 8.25 3D map of IV-1E right-hand polarization PDD corresponding to coordinate, modelling at 9.040 MHz with moving step 50 cm.

8.3.1.2 IV-1E with step 10 cm

In order to get more accurate modelling results, 10 cm is used for the moving step. The modelling calculation amount becomes 90901 since each side has about 300 steps. The left and right hand polarised PDD maps are displayed from Figure 8.26 to Figure 8.33 with different modelling frequencies.

For the antenna arrays modelled with 5.255 MHz, the nearest absolute value of PDD with 90° in Figure 8.26 is provided by the antenna array '35888' which can generate 89.9° PDD for the left-hand polarization. Figure 8.27 shows the right-hand PDD changing with antenna array serial number. The antenna array '5873' is recommended which can provide 61.1° for the right-hand polarization. The recommended antenna arrays serial number and corresponding PDD are summarised in Table 8.3 and 8.4 respectively. The geometry of related antenna arrays are presented from Figure 8.34 to Figure 8.41.

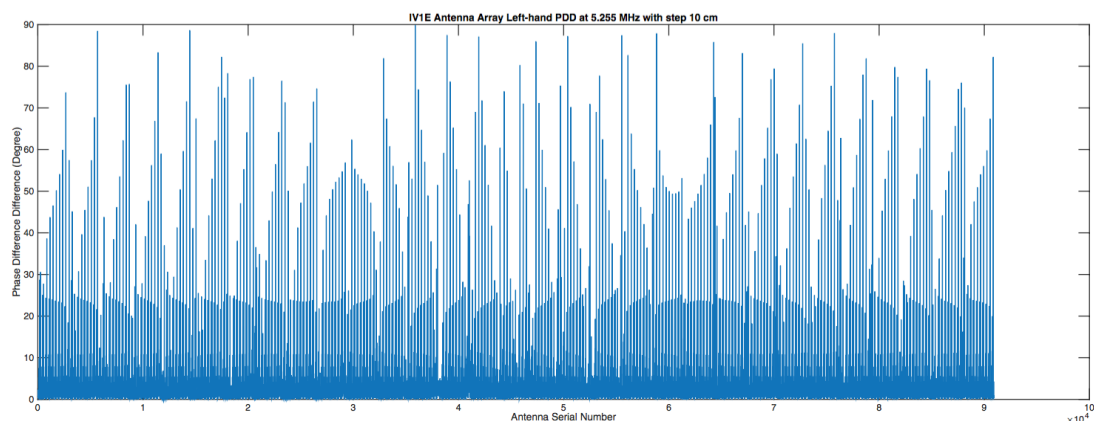


Figure 8.26 IV-1E left-hand PDD with step 10 cm modelling at 5.255 MHz

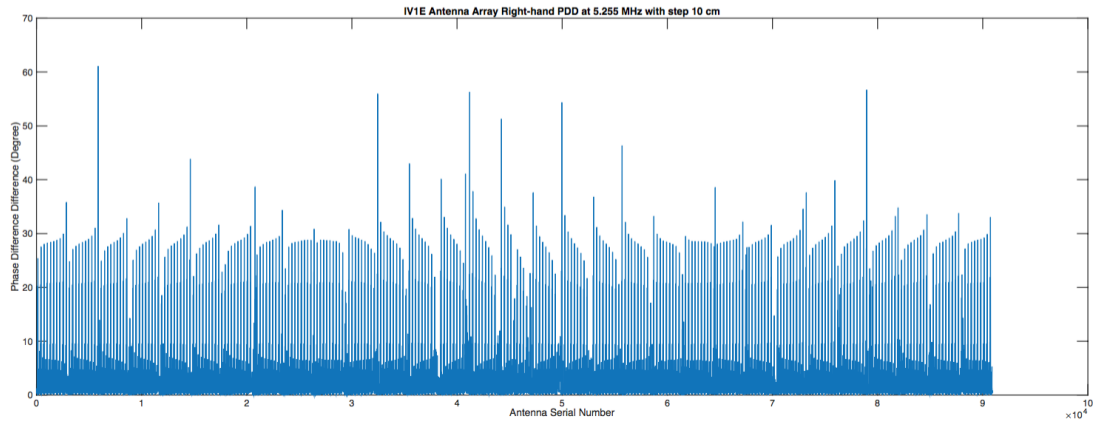


Figure 8.27 IV-1E right-hand PDD with step 10 cm modelling at 5.255 MHz

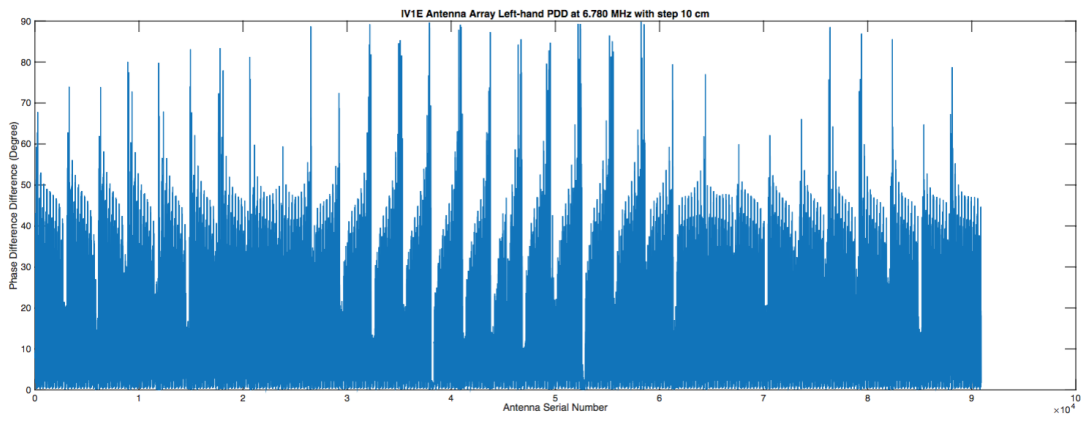


Figure 8.28 IV-1E left-hand PDD with step 10 cm modelling at 6.780 MHz

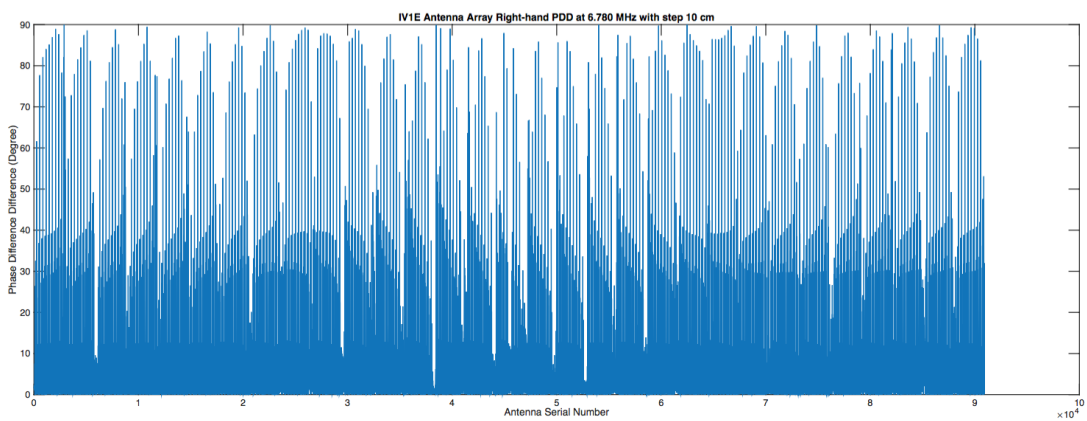


Figure 8.29 IV-1E right-hand PDD with step 10 cm modelling at 6.780 MHz

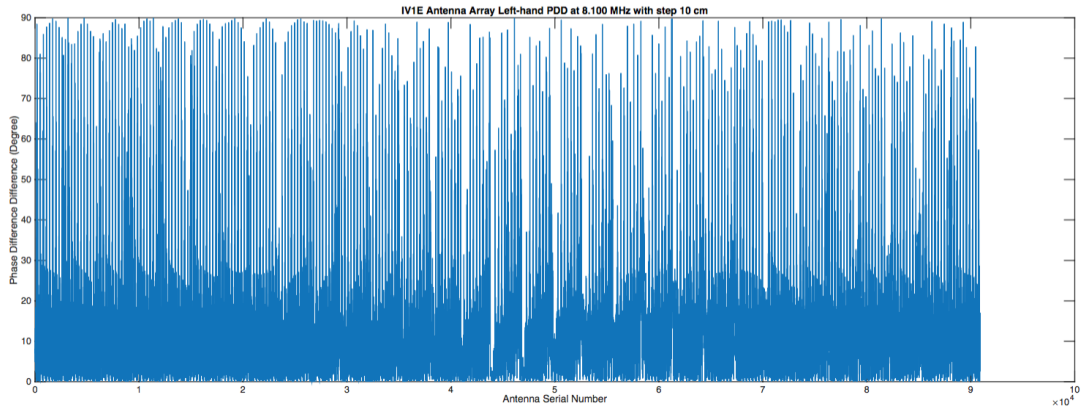


Figure 8.30 IV-1E left-hand PDD with step 10 cm modelling at 8.100 MHz

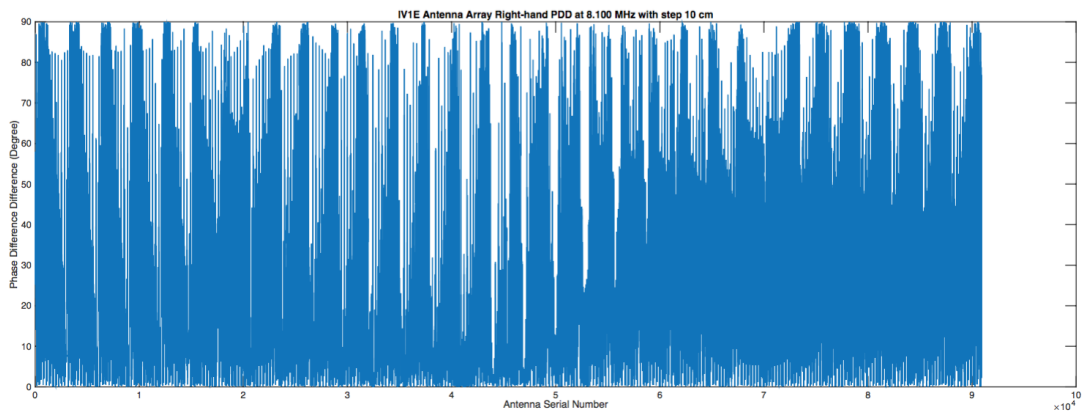


Figure 8.31 IV-1E right-hand PDD with step 10 cm modelling at 8.100 MHz

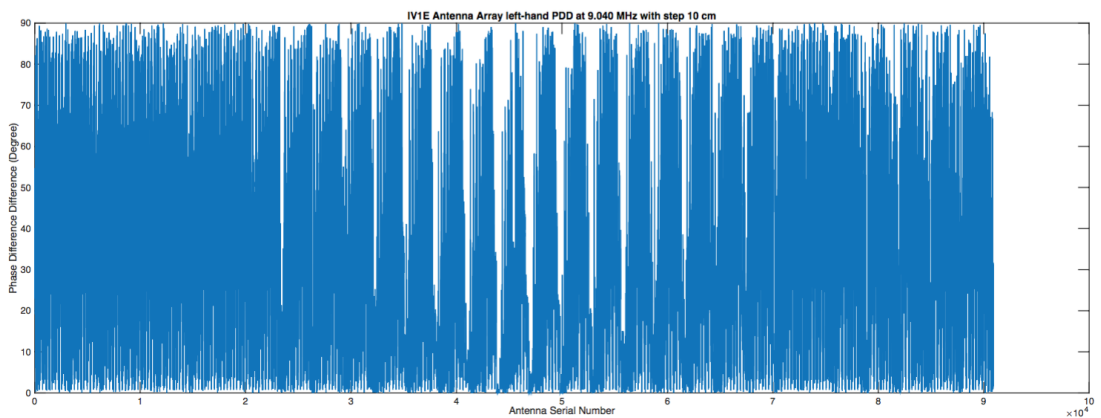


Figure 8.32 IV-1E left-hand PDD with step 10 cm modelling at 9.040 MHz

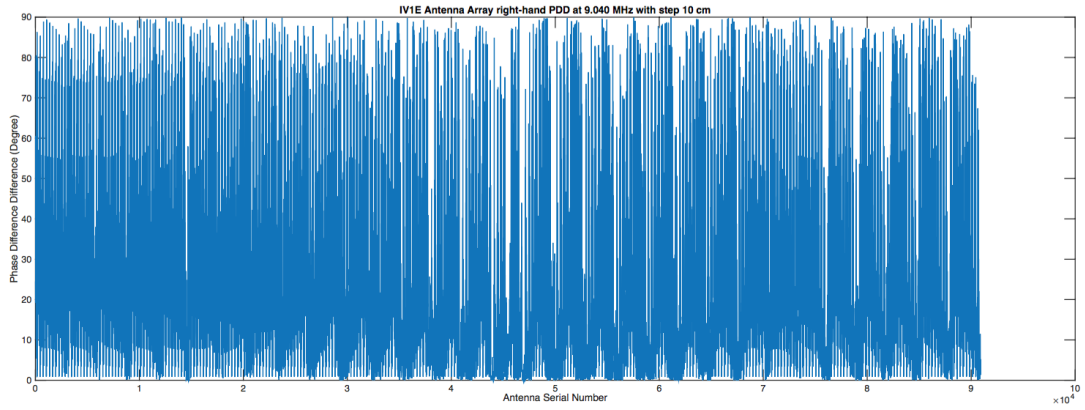


Figure 8.33 IV-1E right-hand PDD with step 10 cm modelling at 9.040 MHz

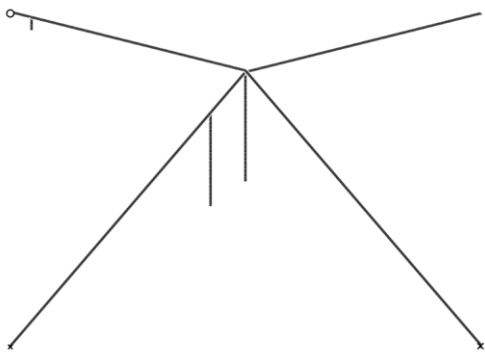


Figure 8.34 Antenna array '2891'

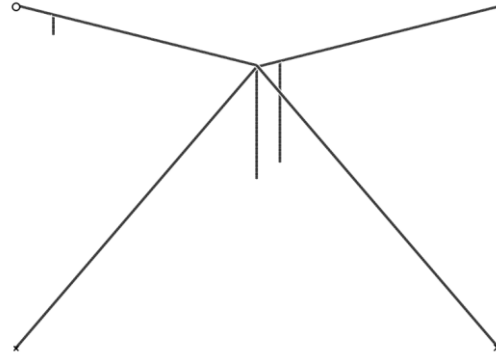


Figure 8.35 Antenna array '5873'

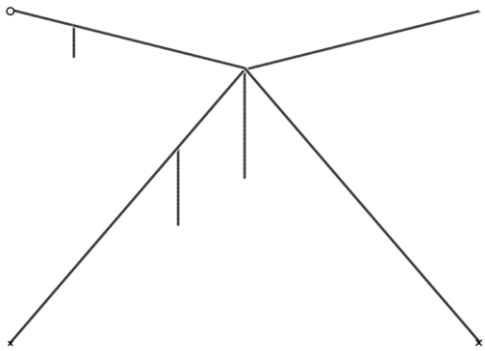


Figure 8.36 Antenna array '11368'

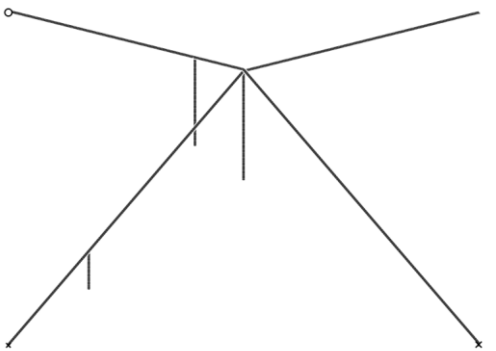


Figure 8.37 Antenna array '35888'

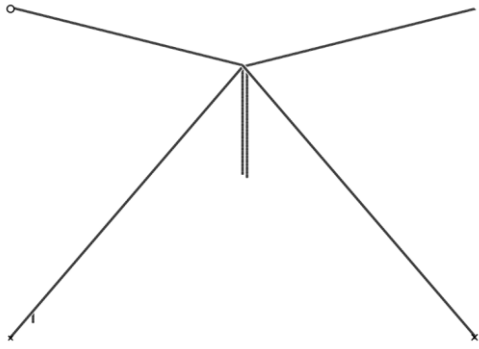


Figure 8.38 Antenna array '46496'

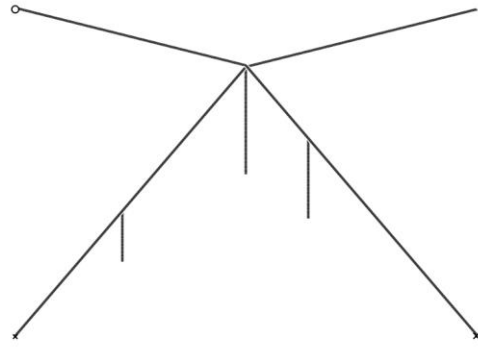


Figure 8.39 Antenna array '58217'

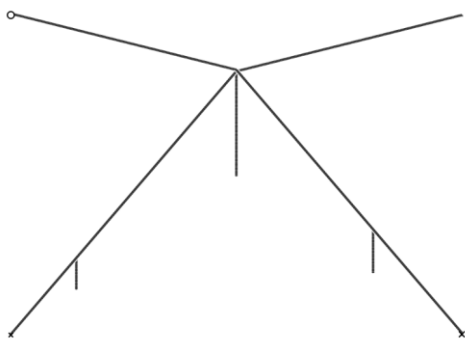


Figure 8.40 Antenna array '73948'

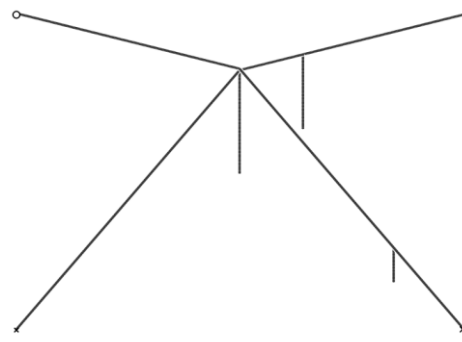


Figure 8.41 Antenna array '77720'

Table 8.3 Recommended antenna array serial numbers for IV-1E (step 10 cm)

Frequency	Left hand (X)	Right hand (O)
5.255 MHz	35888	5873
6.780 MHz	58217	2891
8.100 MHz	11368	77720
9.040 MHz	73948	46496

Table 8.4 Recommended antenna array PDD for IV-1E (step 10 cm)

Frequency	Left hand (X)	Right hand (O)
5.255 MHz	89.9°	61.1°
6.780 MHz	89.8°	90.0°
8.100 MHz	90.0°	90.0°
9.040 MHz	90.0°	90.0°

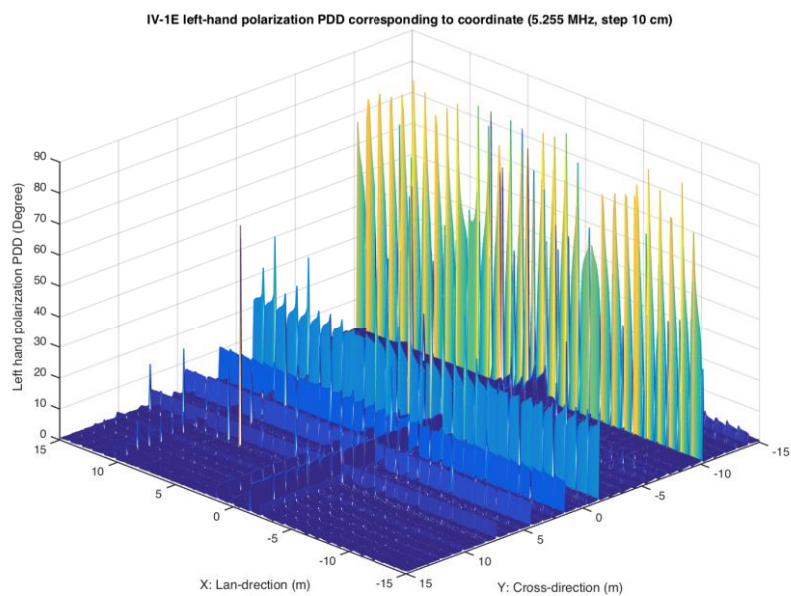


Figure 8.42 3D map of IV-1E left-hand polarization PDD corresponding to coordinate, modelling at 5.255 MHz with moving step 10 cm.

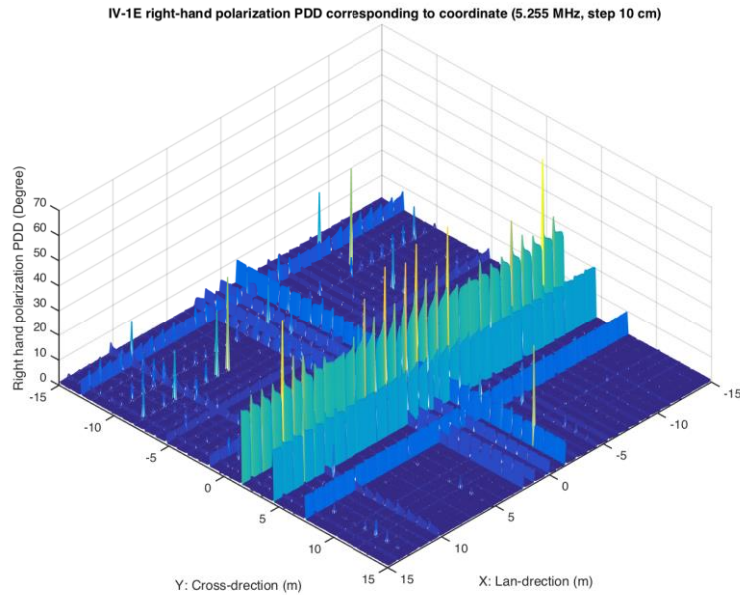


Figure 8.43 3D map of IV-1E right-hand polarization PDD corresponding to coordinate, modelling at 5.255 MHz with moving step 10 cm.

Figure 8.42 and 8.43 displays the left and right hand polarization PDD variation with the adjustable vertical wire elements positions in 3D space, respectively, modelling at 5.255 MHz with moving step 10 cm. When the ‘Cross’ wire element moves to ‘y=-10.2 m’, the left hand polarization PDD can increase significantly (see Figure 8.42). The maximum value of left hand polarization PDD (89.9°) appears when ‘Lan’ wire element move to ‘x=-3.2 m’ and ‘Cross’ wire element move to ‘y=-10.2 m’. For right hand polarization, the PDD can increase nearly 27° on average when ‘Cross’ wire element moves to ‘y=1.5 m’. The PDD reaches the maximum value (61.1°) when the elements move to ‘x=-13.1 m, y=1.5 m’. Figure 8.44 to 8.49 presents the 3D PDD maps for other modelling frequencies.

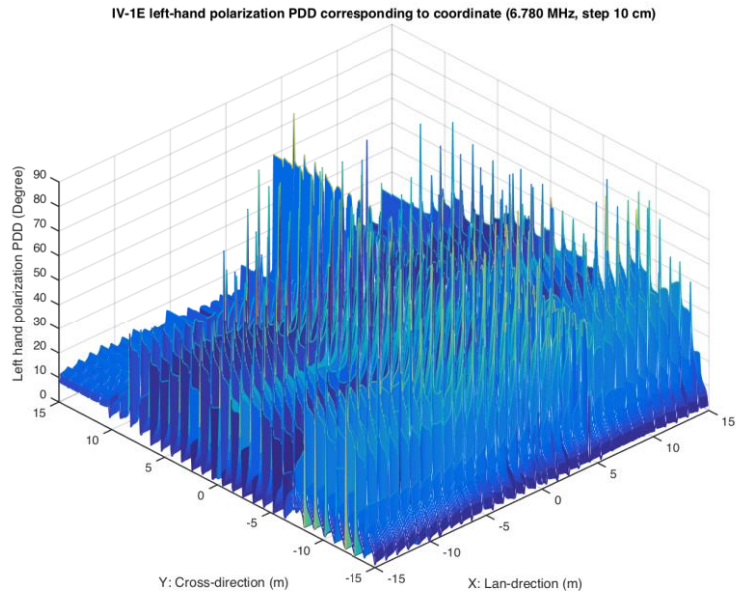


Figure 8.44 3D map of IV-1E left-hand polarization PDD corresponding to coordinate, modelling at 6.780 MHz with moving step 10 cm.

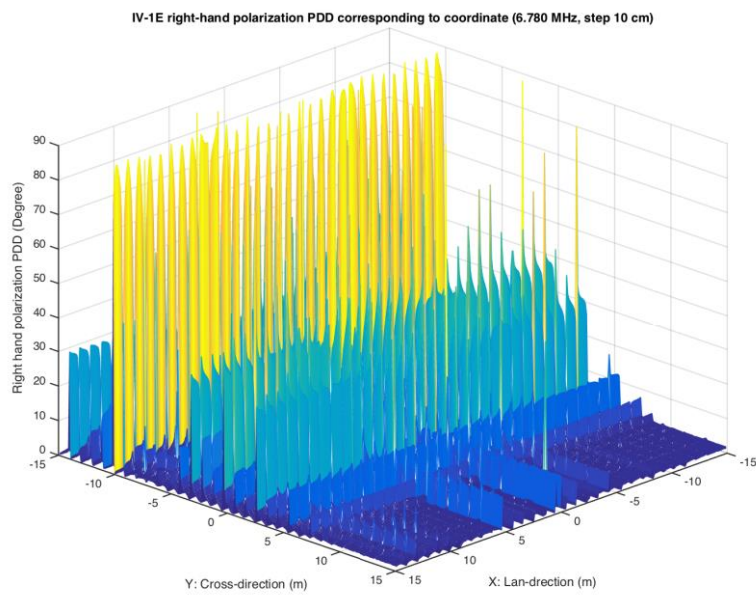


Figure 8.45 3D map of IV-1E right-hand polarization PDD corresponding to coordinate, modelling at 6.780 MHz with moving step 10 cm.

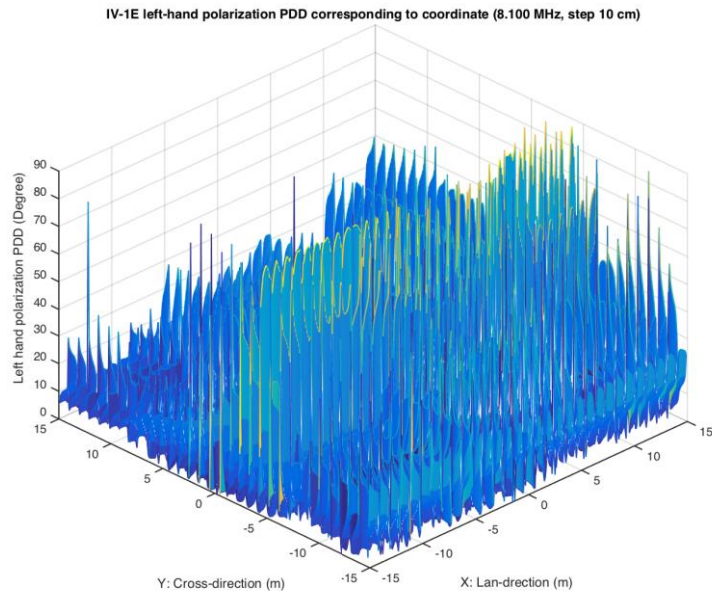


Figure 8.46 3D map of IV-1E left-hand polarization PDD corresponding to coordinate, modelling at 8.100 MHz with moving step 10 cm.

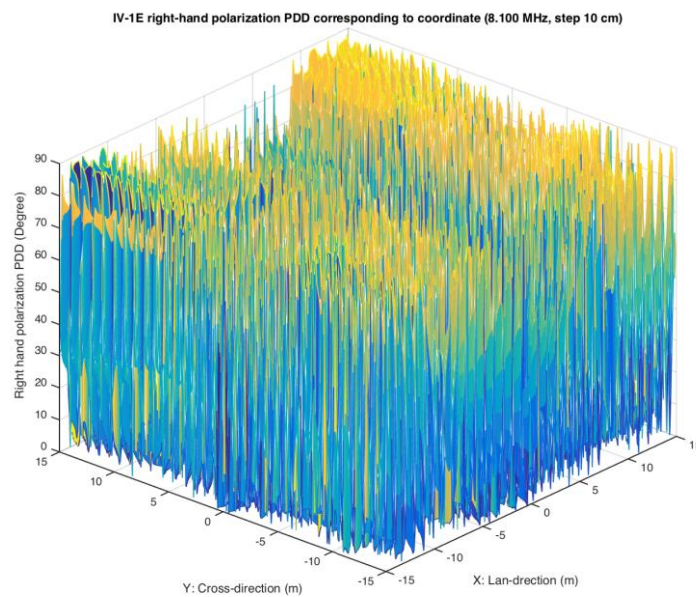


Figure 8.47 3D map of IV-1E right-hand polarization PDD corresponding to coordinate, modelling at 8.100 MHz with moving step 10 cm.

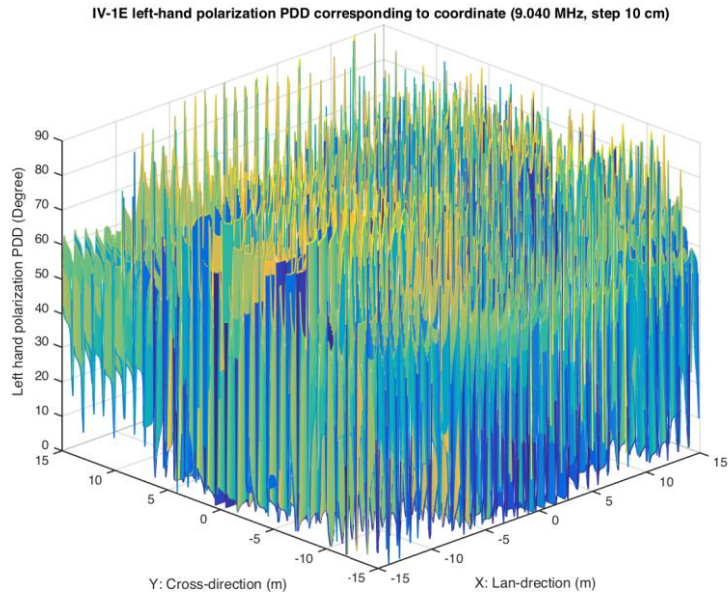


Figure 8.48 3D map of IV-1E left-hand polarization PDD corresponding to coordinate, modelling at 9.040 MHz with moving step 10 cm.

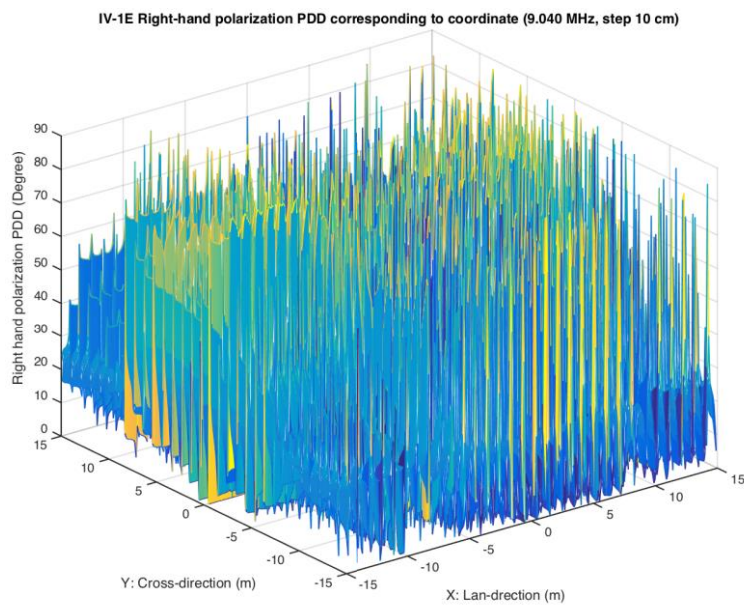


Figure 8.49 3D map of IV-1E right-hand polarization PDD corresponding to coordinate, modelling at 9.040 MHz with moving step 10 cm.

8.3.2 IV-2E

The mainly structure of antenna array IV-2E is the same as IV-1E, consists of a collocated crossed end-fed Vee antenna array. However, instead of using one moving wire-element to connect antennas with ground, IV-2E has two moving wire-elements on each antenna. The wire-element y_2 (located at $y = 14.5$ m) has the top moving priority. After y_2 moved to the end point ($y = -15.0$ m), the wire-element y_1 can move a step forward (start at $y = 15.0$ m). Then y_2 gets back to the point 0.5 m away from y_1 in the movement forward direction. For the wire-elements x_1 (located at $x = -15.0$ m) and x_2 (located at $x = -14.5$ m) on X-axis, x_2 can move a step forward when it meets the condition $y_1 = -14.5$ m and $y_2 = -15.0$ m. The movement of x_1 is depending on x_2 . Only x_2 moves to the end point in X-axis ($x = 15.0$ m), x_1 can move forward by a step. Then x_2 gets back to the point 0.5 m away from x_1 in the movement forward direction. The loop can be finished when it meet the end condition ($y_1 = -14.5$ m; $y_2 = -15.0$ m; $x_1 = 14.5$ m; $x_2 = 15.0$ m). There is approximately 3.23 millions of different antenna array geometry combination with movement step 0.5 m, considering the excitation on both antennas, the calculation amount can reach nearly 6.46 millions. If the movement step use 0.1 m, it will generate about $2.0250e+09$ different antenna arrays input files. Alice current calculation ability cannot meet such a huge calculation. The left and right hand PDD maps changing with antenna array serial number are displayed from Figure 8.50 to Figure 8.57.

For IV-2E modelling at 5.255 MHz, the array ‘661758’ become the best left-hand polarization array which can generate 80.43° phase difference difference. The array ‘2498756’ is selected as the right-hand polarization recommended antenna array that can provide 87.93° PDD. Table 8.5 and 8.6 summarised the recommended IV-2E antenna arrays serial number and PDD with different modelling frequencies respectively. The optimized geometry of antenna arrays are displayed from Figure 8.58 to 8.65.

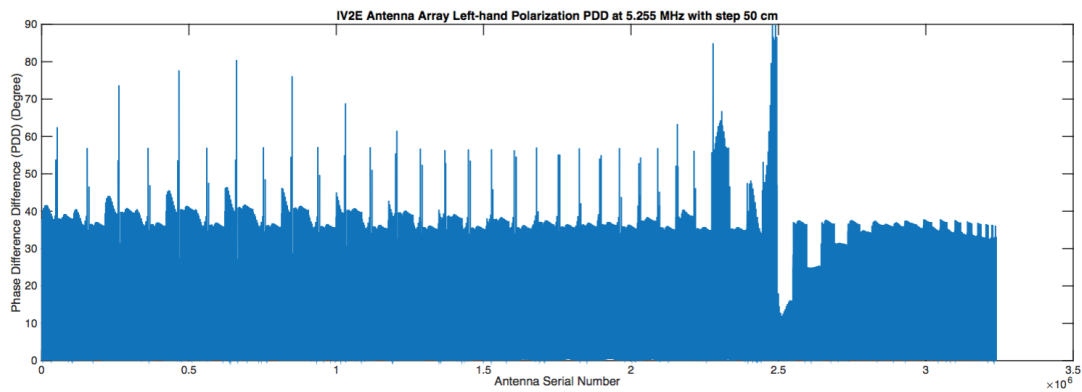


Figure 8.50 IV-2E left-hand PDD with step 50 cm modelling at 5.255 MHz

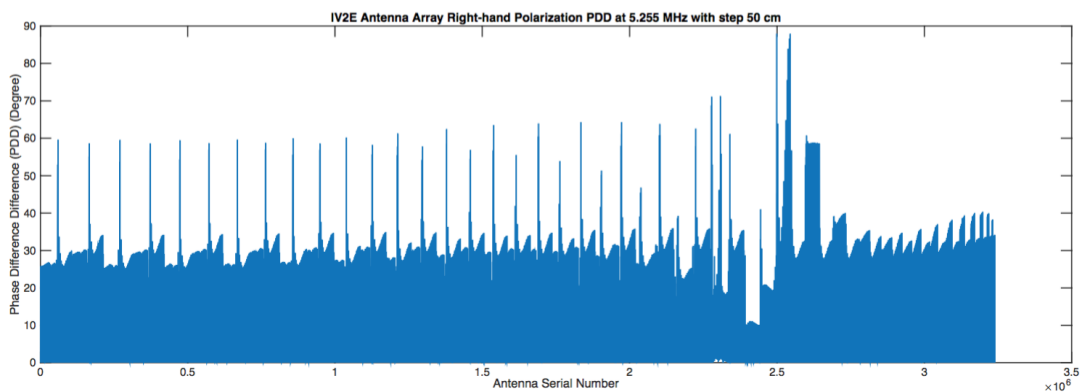


Figure 8.51 IV-2E right-hand PDD with step 50 cm modelling at 5.255 MHz

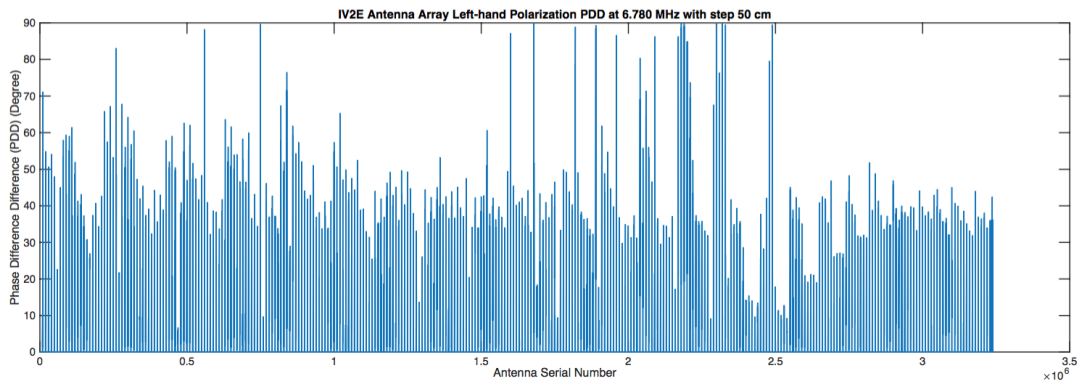


Figure 8.52 IV-2E left-hand PDD with step 50 cm modelling at 6.780 MHz

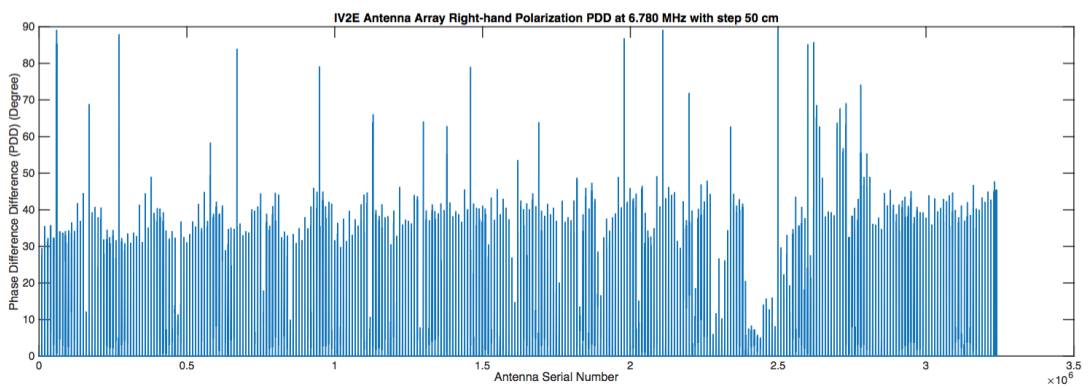


Figure 8.53 IV-2E right-hand PDD with step 50 cm modelling at 6.780 MHz

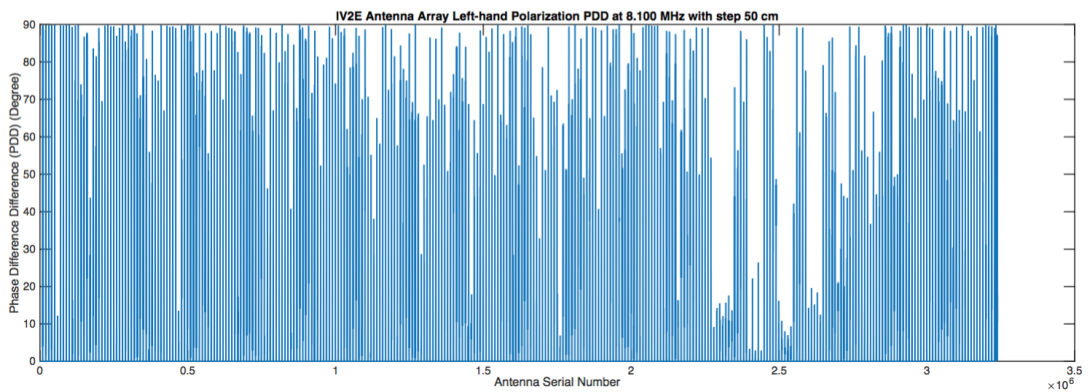


Figure 8.54 IV-2E left-hand PDD with step 50 cm modelling at 8.100 MHz

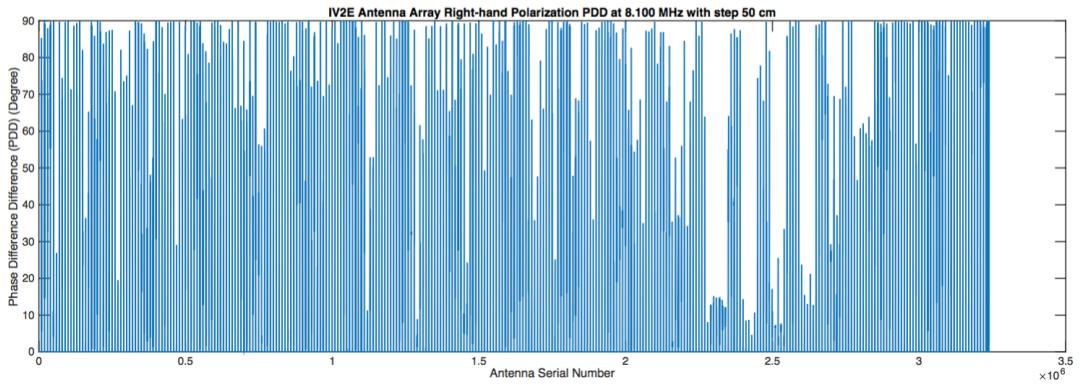


Figure 8.55 IV-2E right-hand PDD with step 50 cm modelling at 8.100 MHz

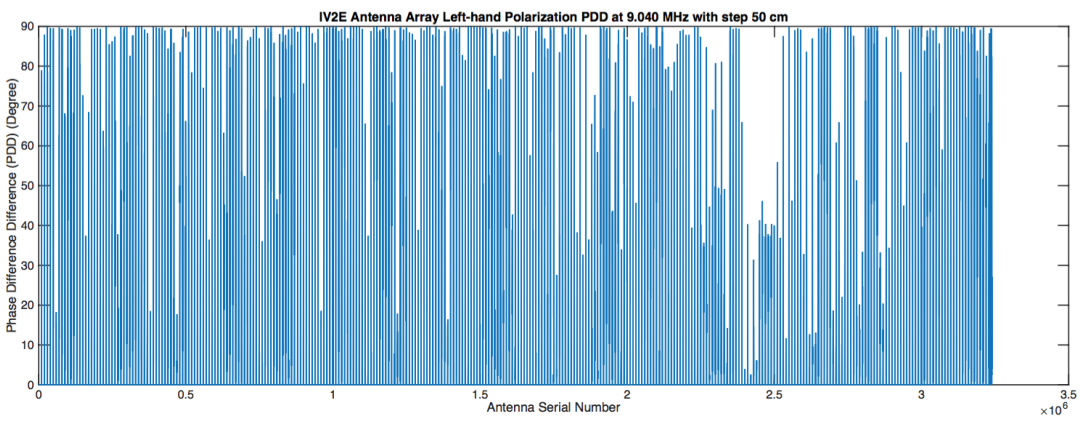


Figure 8.56 IV-2E left-hand PDD with step 50 cm modelling at 9.040 MHz

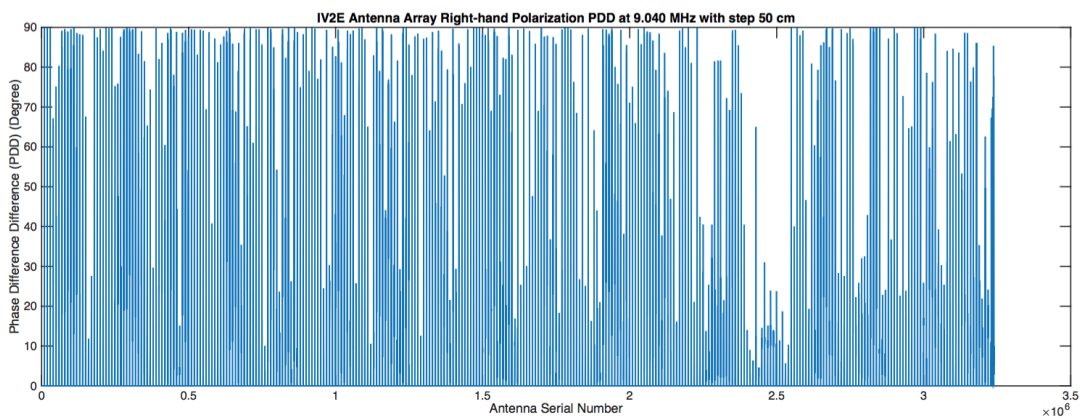


Figure 8.57 IV-2E right-hand PDD with step 50 cm modelling at 9.040 MHz

Table 8.5 Recommended antenna array serial numbers for IV-2E (step 50 cm)

Frequency	Left hand (X)	Right hand (O)
5.255 MHz	661758	2498756
6.780 MHz	2179780	2499114
8.100 MHz	879301	1069501
9.040 MHz	3159137	109679

Table 8.6 Recommended antenna array PDD for IV-2E (step 50 cm)

Frequency	Left hand (X)	Right hand (O)
5.255 MHz	80.43°	87.93°
6.780 MHz	89.96°	89.56°
8.100 MHz	89.99°	90.00°
9.040 MHz	89.99°	89.99°

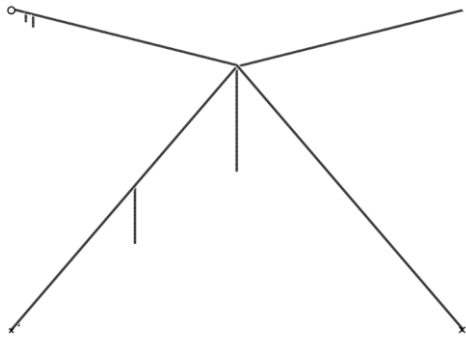


Figure 8.58 IV-2E '109679'

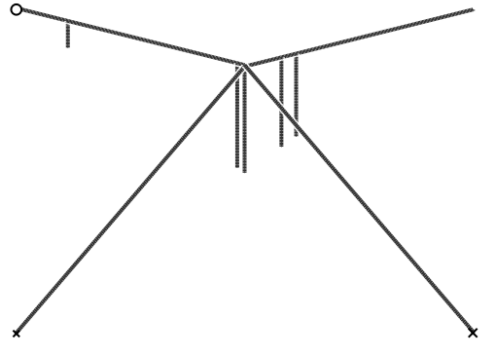


Figure 8.59 IV-2E '661758'

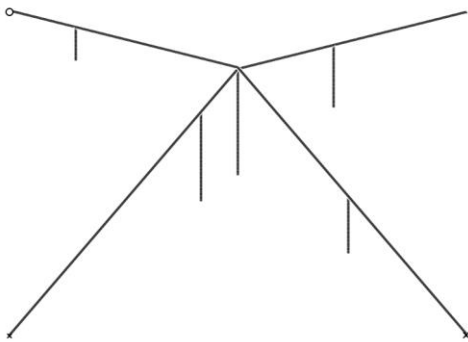


Figure 8.60 IV-2E '879301'

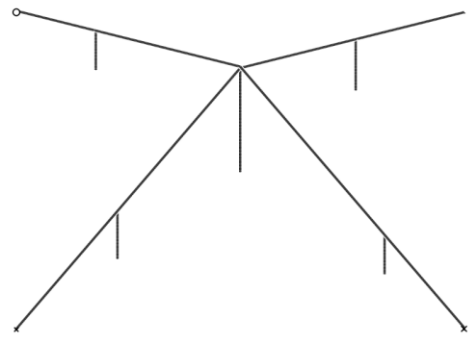


Figure 8.61 IV-2E '1069501'

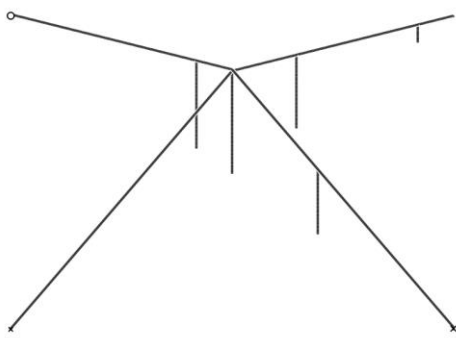


Figure 8.62 IV-2E '2179780'

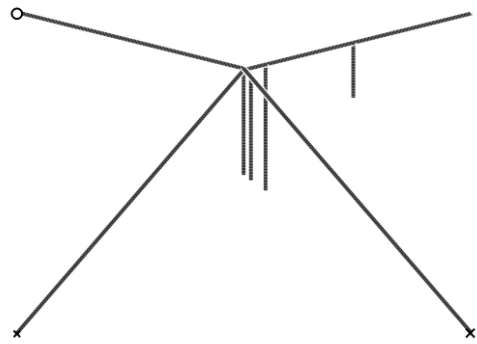


Figure 8.63 IV-2E '2498756'

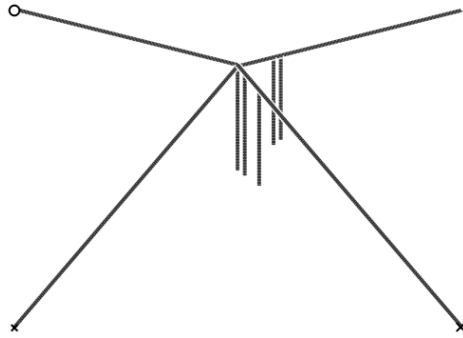


Figure 8.64 IV-2E '2499114'

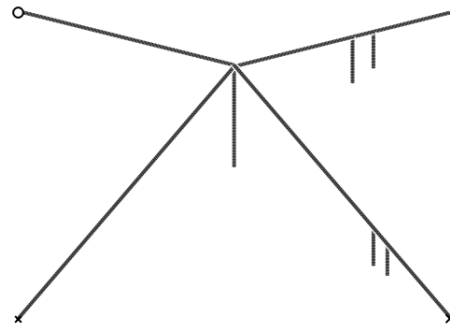


Figure 8.65 IV-2E '3159137'

8.4 HPC antenna array optimization analysis

As shown in Section 8.3, antenna array PDD can be altered by moving the position of the vertical wire element on the array or adding more vertical wire elements. Greater phase difference difference can be achieved by moving the vertical wire element to some particular positions on the antenna array, which means that the lower correlation level of the antenna array elements can be obtained at these positions. Furthermore, the change of phase difference differences for left and right hand polarization are not synchronous. It's worth to notice that, the greater PDD can be obtained easier with higher modelling frequency. This can be found in 3D maps of IV-1E PDD with moving step 10 cm (see Figure 4.42 to Figure 4.49).

With the smaller moving step, the PDD can be obtained more accuracy; meanwhile, the calculation quantity can be increased rapidly. For instance, calculation quantity for IV-2E antenna array with moving step 50 cm is about 6.46 million. This

number goes up to approximately 4050 million after the moving step changing to 10 cm. Currently, Alice can finish processing these 6.46 million NEC input files in about 12 to 16 hours. To deal with 4050 million different NEC GW cards, it may take more than 10000 hours according to current processing speed.

The optimized antenna arrays can be built according to the corresponding GW card. For instance, the geometry detail of antenna array IV-2E '879301' (see Figure 8.60) is presented in its GW card (see Figure 8.66). As showed in the figure, the command lines from 'GW 1' to 'GW 9' described the 3D coordinates for the original crossed end-fed Vee antenna array. The coordinates of added four vertical wire elements were described using command lines from 'GW 10' to 'GW 13'.

```

CM ***879301_IV_2E_Lan_6780_Step50cm
CM Inverted-V
CE -----
GW 1 3 -15.5000 0.000000 0.000000 -15.5000 0.000000 0.200000 8.14E-04
GW 2 171 -15.5000 0.000000 0.200000 0.000000 0.000000 7.300000 8.14E-04
GW 3 171 0.000000 0.000000 7.300000 15.50000 0.000000 0.200000 8.14E-04
GW 4 3 15.50000 0.000000 0.200000 15.50000 0.000000 0.000000 8.14E-04
GW 5 3 0.000000 -15.5000 0.000000 0.000000 -15.5000 0.100000 8.14E-04
GW 6 171 0.000000 -15.5000 0.100000 0.000000 0.000000 7.200000 8.14E-04
GW 7 171 0.000000 0.000000 7.200000 0.000000 15.50000 0.100000 8.14E-04
GW 8 3 0.000000 15.50000 0.100000 0.000000 15.50000 0.000000 8.14E-04
GW 9 71 0.000000 0.000000 0.000000 0.000000 0.000000 7.100000 0.025000
GW 10 23 -11.0000 0.000000 0.000000 -11.0000 0.000000 2.261290 8.14E-04
GW 11 39 7.5000 0.000000 0.000000 7.5000 0.000000 3.864516 8.14E-04
GW 12 43 0.000000 6.5000 0.000000 0.000000 6.5000 4.222581 8.14E-04
GW 13 61 0.000000 -2.5000 0.000000 0.000000 -2.5000 6.054839 8.14E-04
GE 1
LD 4 4 2 2 300.0000 0.000000
LD 4 5 2 2 300.0000 0.000000
FR 0 1 0 0 6.780000 0.000000
GN 0 0 0 0 13.00000 0.005000
EX 0 1 2 1 1.000000 0.000000
XQ
RP 0 360 1 1000 -90.000 0.000 1.000 0.000 5.000E+03
XQ
EN

```

Figure 8.66 Antenna array IV-2E '879301' GW card

The PDD performance is highly sensitive to the geometry of antenna arrays. As 3D PDD maps showed in Section 8.3, only when the alterable vertical wire elements moved to particular positions, the great PDD value can be obtained. Compare antenna array IV-1E right-hand 3D PDD maps modelling at 6.780 MHz with moving step 50 cm (see Figure 8.21) and moving step 10 cm (see Figure 8.45), much more particular positions can be found with greater PDD values for moving step 10 cm modelling. The table 8.2 shows that the peak value of right-hand PDD is only 61.2° for 6.780 MHz with moving step 50 cm. However, this value increases to 90.0° when the modelling using moving step 10 cm (see Table 8.4)

The PDD performance is also sensitive to frequency based on end-fed Vee antenna array modelling: with higher modelling frequency, the probability to obtain greater PDD are significantly increased. For instance, Figure 8.42 shows the 3D left-hand polarization PDD map of IV-1E with moving step 10 cm, using modelling frequency 5.255 MHz. The greater PDD only can be obtained when 'Cross' element moves to 'y=-10.3 m'. However, with modelling frequency 9.040 MHz, much more geometries can produce great PDD (see Figure 8.48).

Currently, the HPC modellings are based on end-fed crossed Vee antenna array with added alterable vertical wire elements. As showed in Section 7.2.7, the Non-Planar Twisted (NPT) antenna array also has a good decorrelation performance between the array elements. Further HPC modellings can be conducted using NPT antenna array to investigate the relative space effects on the

correlation level between array elements and frequency sensibility to different antenna array geometries etc.

Furthermore, in order to reduce the calculating quantity, 'Monte Carlo' method can be employed instead of searching all the antenna arrays geometry. According to 'Monte Carlo' method, antenna array geometries can be produced randomly. Once the calculated PDD of the array meet the default value, the antenna array GW card can be extracted and the geometry of the array can be recovered according its card. For instance, the calculating quantity of IV-2E with step 10 cm is about 4050 million, more than 10000 hours will be cost if calculate all the antenna array geometries according to current processing speed. As a result, 'Monte Carlo' method using random theory to find the solution can potentially show a big advantage.

Chapter 9 Conclusions

The previous experimental measurement carried out by Gunashekar et al [2009] showed that several tens of metres were required for the successful implementation of MIMO spatial diversity in the HF band. Furthermore, they also showed that radiation pattern diversity can also be used to replace spatial diversity to get decorrelation between antenna array elements. As a result, collocated heterogeneous antenna array can be used to replace large spaced homogeneous array to achieve same level of data transmission rate. This can greatly reduce the space limitation in HF antenna array development and allow more applications in long distance communications in aviation and navigation etc.

In order to get better understanding about radiation pattern diversity, massive antenna modelling has been carried out in the last three years. The concept of phase difference difference (PDD) based on pattern diversity is proposed to measure the decorrelation level between antenna array elements in this thesis. The PDD employs coordinate transform from $(\vec{E}_\theta, \vec{E}_\phi)$ to (\vec{E}_l, \vec{E}_r) to get the left and right hand polarization E-field magnitude and phase information, which corresponds to ordinary and extra-ordinary mode in sky-wave propagation. Then it uses the variation of the phase differences generated by antenna array elements to measure the correlation level of the array. Greater phase difference difference can make the combination relationship between incident waves at receiving ends more different, which means that the output signals become more decorrelated. This principle is

also suitable for the transmitting antenna array. Several collocated transmitting antenna arrays have been designed according to this concept and tested via a 202 km radio link in the last two years. The experimental measurements showed that the correlation level of the newly designed antenna arrays were systematically lower than referenced antenna array.

In order to further develop the PDD potential of the collocated crossed end-fed Vee antenna array, high performance computing was applied in the modelling work. The simulation results showed that higher PDD could be obtained by moving the vertical wire elements to particular positions of the antenna array. Furthermore, by adding more vertical wire elements or twisting the current path on the antenna can also change the PDD of the antenna array. As a result, the decorrelation between collocated end-fed Vee antenna array elements can be achieved more specific.

Since high performance computing has been introduced to modelling work, more collocated antenna arrays with different geometries can be modelled in the future work, especially for the compact arrays. Previous experiments showed that 'X-Y-Z' and 'GSL' array had a good decorrelation level as the receiving antenna arrays. These arrays elements relative position or size can be further optimized using HPC technique to get more phase difference difference. Furthermore, the framework using HPC to processing NEC input files could be optimized to handle greater calculation quantity. The initial processing time of IV-2E array was about a week. After optimizing submission program and using C language to deal with NEC

output file directly in each node, the processing can now be finished in 16 hours. However, the processing speed still needs to be improved in order to deal with data quantity in billion levels. To achieve this, enhancement of the NEC engine processing speed could be a possible way. 'Monte Carlo' method can be employed in further modelling work. So far, there are two NEC versions for Linux platform: nec2c and necpp. Necpp is the evolution version of the nec2c, which can process the input file much quicker. However, due to the limitation of antenna geometry setting, nec2c is finally employed in Alice system instead of necpp. Since nec2c and necpp are open source software, improving the software code can be a possibly way to obtain faster processing speed.

Reference

- Adcock, F. (1919). Improvement in means for determining the direction of a distant source of electromagnetic radiation. British Patent, 130490.
- Aminaei, A., Wolt, M. K., Chen, L. N., Bronzwaer, T., Pourshaghghi, H. R., Bentum, M. J., and Falcke, H. (2014, March). Basic radio interferometry for future lunar missions. In *Aerospace Conference, 2014 IEEE* (pp. 1-19). IEEE.
- Andrews, M. R., and Mitra, P. P. (2001). Tripling the capacity of wireless communications using electromagnetic polarization. *Nature*, 409(6818), 316-318.
- Appleton, E. V. (1932). Wireless studies of the ionosphere. *Wireless Section, Proceedings of the Institution of Electrical Engineers*, 7(21), 257-265.
- Bertel, L., Parion, P., and Lemur, D. (1996). Model of narrowband signal used in ionospheric high frequency (3–30 MHz) channel. *Journees d'etudes SEE*, 96.
- Brandenburg, L. H., and Wyner, A. D. (1974). Capacity of the Gaussian channel with memory: The multivariate case. *Bell System Technical Journal*, 53(5), 745-778.

Burke, G. J., and Poggio, A. J. (1981). Numerical Electromagnetics Code (NEC)—Method of Moments; Part I: Program Description—Theory, Part II: Program Description—Code, Part III: User's Guide. Lawrence Livermore National Lab. Rep. UCID-18834 (January 1981).

Chiani, M., Win, M. Z., and Zanella, A. (2003). On the capacity of spatially correlated MIMO Rayleigh-fading channels. *IEEE Transactions on, Information Theory*, 49(10), 2363-2371.

Davies, K. (1990). Ionospheric radio. IET.

Erhel, Y., Bertel, L., and Marie, F. (1998). A method of direction finding operating on an array of collocated antennas. In *Antennas and Propagation Society International Symposium, 1998. (Vol. 1, pp. 207-210)*. IEEE.

Erhel, Y., D. Lemur, L. Bertel, and F. Marie (2004), HF radio direction finding operating on a heterogeneous array: Principles and experimental validation, *Radio Sci.*, 39, RS1003, doi:10.1029/2002RS002860.

Feeney, S. M., Salous, S., Warrington, E. M., Gunashekar, S. D., Abbasi, N., Bertel, L., and Oger, M. (2009). Compact antenna arrays for HF MIMO applications. *The Institution of Engineering and Technology 11th International Conference on Ionospheric radio Systems and Techniques, 2009.(IRST 2009)*. (pp. 1-5). IET.

- Foschini, G. J. (1996). Layered space-time architecture for wireless communication in a fading environment when using multi-element antennas. *Bell Labs Technical Journal*, 1(2), 41-59.
- Foschini, G. J., and Gans, M. J. (1998). On limits of wireless communications in a fading environment when using multiple antennas. *Wireless personal communications*, 6(3), 311-335.
- Foschini, G. J., Golden, G. D., Valenzuela, R. A., & Wolniansky, P. W. (1999). Simplified processing for high spectral efficiency wireless communication employing multi-element arrays. *Selected Areas in Communications, IEEE Journal on*, 17(11), 1841-1852.
- Griffith Jr, B. W. (2000). *Radio-electronic transmission fundamentals*. SciTech Publishing.
- Gunashekar, S. D., Warrington, E. M., Strangeways, H. J., Erhel, Y., Salous, S., Feeney, S. M., and Oger, M. (2009 a). Utilization of antenna arrays in HF systems. *Annals of geophysics.*, 52(3/4), 323-338.
- Gunashekar, S. D., Warrington, E. M., Salous, S., Feeney, S. M., Zhang, H., Abbasi, N., and Oger, M. (2008). Early results of experiments to investigate the feasibility of employing MIMO techniques in the HF band. In *Antennas and Propagation Conference, 2008. LAPC 2008. Loughborough* (pp. 161-164). IEEE.

- Gunashekar, S. D., Warrington, E. M., Salous, S., Feeney, S. M., Abbasi, N. M., Bertel, L., and Oger, M. (2009 b). Investigations into the feasibility of multiple input multiple output techniques within the HF band: Preliminary results. *Radio Science*, 44(1).
- Gunashekar, S. D., Warrington, E. M., Feeney, S. M., Salous, S., & Abbasi, N. M. (2010). MIMO communications within the HF band using compact antenna arrays. *Radio Science*, 45(6). doi:10.1029/2010RS004416, 2010.
- Harrington, R. F. (1987). The method of moments in electromagnetics. *Journal of Electromagnetic Waves and Applications*, 1(3), 181-200.
- Jakes, W. C., and Cox, D. C. (1994). *Microwave mobile communications*. Wiley-IEEE Press.
- Kaye, A., and George, D. (1970). Transmission of multiplexed PAM signals over multiple channel and diversity systems. *Communication Technology, IEEE Transactions on*, 18(5), 520-526.
- Kermoal, J. P., Schumacher, L., Pedersen, K. I., Mogensen, P. E., & Frederiksen, F. (2002). A stochastic MIMO radio channel model with experimental validation. *IEEE Journal on Selected Areas in Communications*, 20(6), 1211-1226.
- Levis, C., Johnson, J. T., and Teixeira, F. L. (2010). *Radiowave propagation: physics and applications*. John Wiley & Sons.

Lim, H. M., C. C. Constantinou, and T. N. Arvanitis (2007), On the ensemble average capacity of multiple input multiple output channels in outdoor line of sight multipath urban environments, *Radio Science*, 42, RS1006, doi: 10.1029/2005RS003406.

Liu, L., Zhao, B., Wan, W., Ning, B., Zhang, M. L., and He, M. (2009). Seasonal variations of the ionospheric electron densities retrieved from Constellation Observing System for Meteorology, Ionosphere, and Climate mission radio occultation measurements. *Journal of Geophysical Research: Space Physics* (1978–2012), 114(A2).

Loyka, S. L. (2001). Channel capacity of MIMO architecture using the exponential correlation matrix. *Communications Letters, IEEE*, 5(9), 369-371.

Marie, F., Y. Erhel, L. Bertel, and D. Lemur (2000), Design of a HF compact direction finding system based on collocated antennas, in *Proceedings of Eighth International Conference on HF Radio Systems and Techniques*, IEE Conf. Publ., 474, 127–131.

Neeser, F. D., & Massey, J. L. (1993). Proper complex random processes with applications to information theory. *IEEE Transactions on Information Theory*, 39(4), 1293-1302.

Oger, M., F. Marie, D. Lemur, G. Le Bouter, Y. Erhel, and L. Bertel (2006), A method to calibrate HF receiving antenna arrays, in *Processing of the*

10th International Conference on Ionospheric Radio Systems and Techniques (IRST 2006), Inst. of Eng. and Technol., London.

Radio Regulations (2004) – Art. 1 § 1.154, ITU

Raleigh, G. C., & Cioffi, J. M. (1998). Spatio-temporal coding for wireless communication. *IEEE Transactions on Communications*, 46(3), 357-366.

Shiu, D. S., Foschini, G. J., Gans, M. J., & Kahn, J. M. (2000). Fading correlation and its effect on the capacity of multielement antenna systems. *IEEE Transactions on Communications*, 48(3), 502-513.

Smith, J. L. (2008). *Basic NEC with Broadcast Applications*. Taylor & Francis.

Smith, N. (1939). The relation of radio sky-wave transmission to ionosphere measurements. *Proceedings of the IRE*, 27(5), 332-347.

Strangeways, H. J. (2006). Estimation of signal correlation at spaced antennas for multi-moded ionospherically reflected signals and its effect on the capacity of SIMO and MIMO HF links. *Ionospheric Radio Systems and Techniques, 2006. IRST 2006*, 306-310.

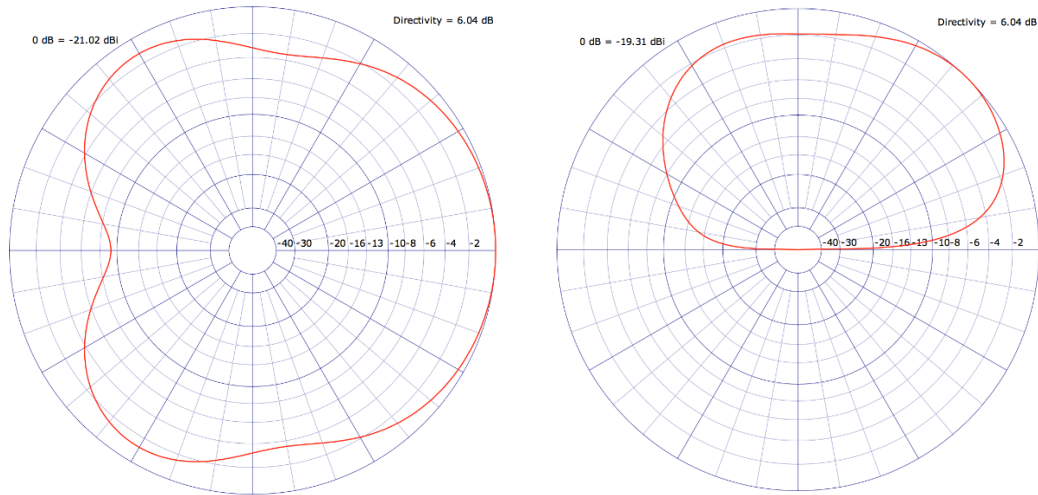
Telatar, E. (1999). Capacity of Multi-antenna Gaussian Channels. *European Transactions on Telecommunications*, 10(6), 585-595.

- Tarokh, V., Jafarkhani, H., and Calderbank, A. R. (1999). Space-time block codes from orthogonal designs. *IEEE Transactions on Information Theory*, 45(5), 1456-1467.
- Viswanath, P., Tse, D. N. C., and Anantharam, V. (2001). Asymptotically optimal water-filling in vector multiple-access channels. *IEEE Transactions on Information Theory*, 47(1), 241-267.
- Waldschmidt, C., Hagen, J. V., and Wiesbeck, W. (2002, June). Influence and modelling of mutual coupling in MIMO and diversity systems. In *Antennas and Propagation Society International Symposium, 2002*. (Vol. 3, p. 190). IEEE.
- Wallace, J. W., and M. A. Jensen (2002), Modelling the indoor MIMO wireless channel, *IEEE Transactions Antennas Propagation*, 50(5), 591–599.
- Warrington, E. M., Gunashekar, S. D., Salous, S., Feeney, S. M., Zhang, H., Abbasi, N., and Oger, M. (2008). Investigations into the Feasibility of MIMO Techniques Within the HF Band: Preliminary Results. In *12th International Ionospheric Effects Symposium*. Alexandria, USA.
- Winters, J. H. (1987). On the capacity of radio communication systems with diversity in a Rayleigh fading environment. *IEEE Journal on Selected Areas in Communications*, 5(5), 871-878.

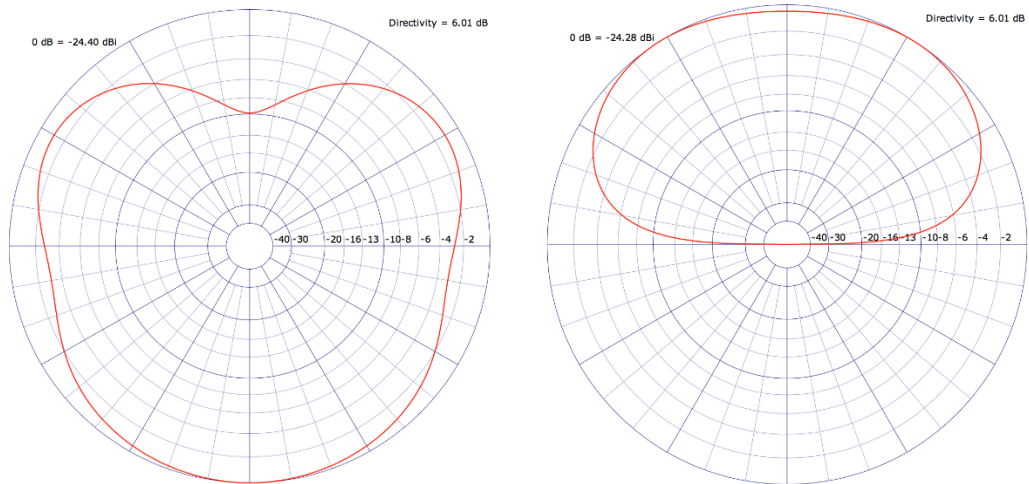
Xu, S., Zhang, H., Yang, H., and Wang, H. (2004). New considerations for high frequency communications. In Communications, 2004 and the 5th International Symposium on Multi-Dimensional Mobile Communications Proceedings. The 2004 Joint Conference of the 10th Asia-Pacific Conference on (Vol. 1, pp. 444-447). IEEE.

Zheng, L., and Tse, D. N. C. (2003). Diversity and multiplexing: a fundamental tradeoff in multiple-antenna channels. *IEEE Transactions on Information Theory*, 49(5), 1073-1096.

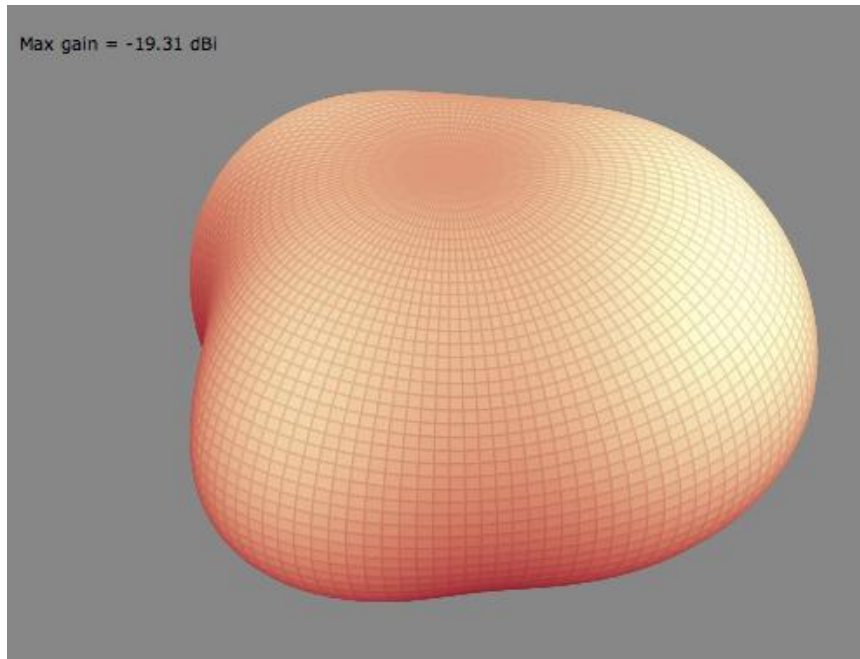
Appendix 1: T1 antenna array 2D and 3D radiation patterns



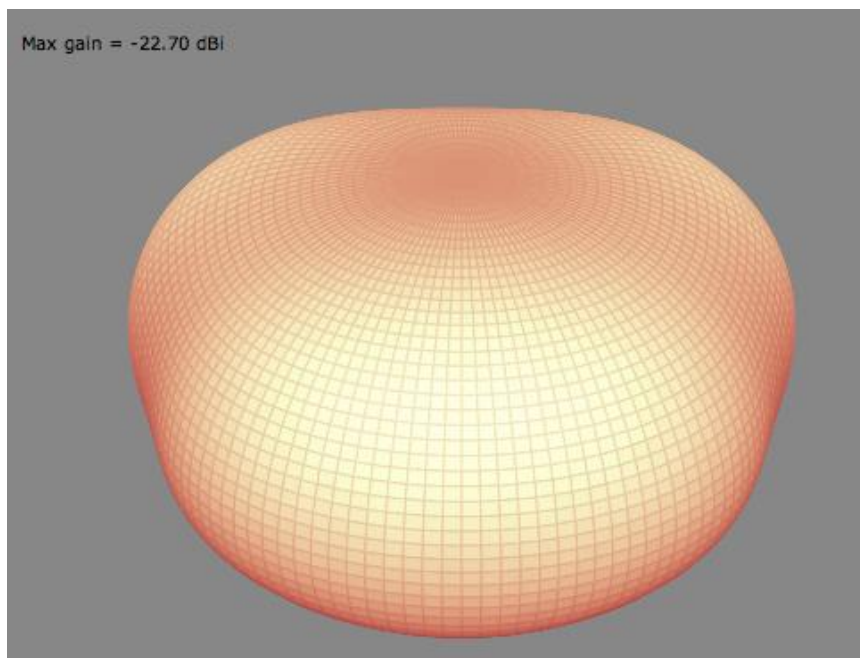
Radiation pattern produced by the array T1 element pointing to Lancaster (T1-Lan) at 6.780 MHz, Azimuth-plot (left) and Elevation-plot (right).



Radiation pattern produced by the array T1 array element perpendicular to Lancaster (T1-Cross) at 6.780 MHz, Azimuth-plot (left) and Elevation-plot (right)

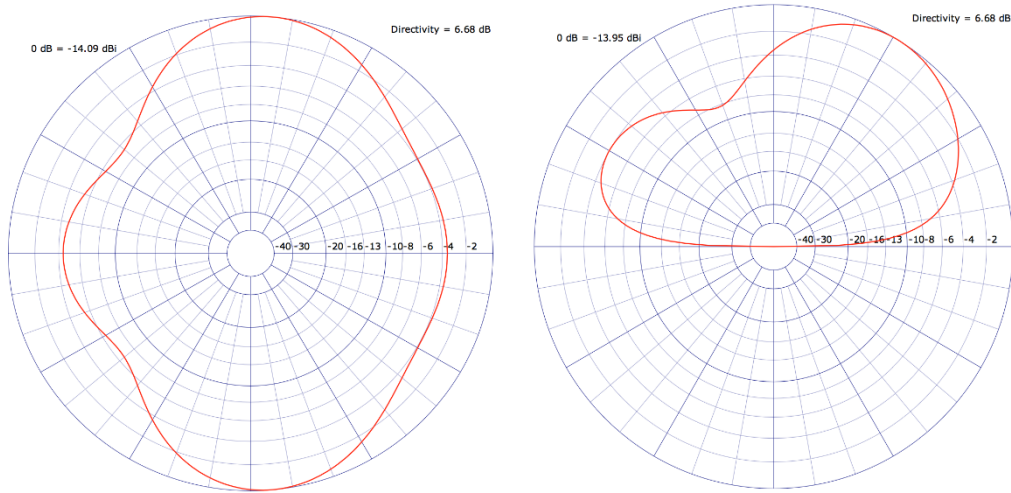


3D Radiation pattern produced by T1 array element pointing to Lancaster (T1-Lan) at 6.780 MHz

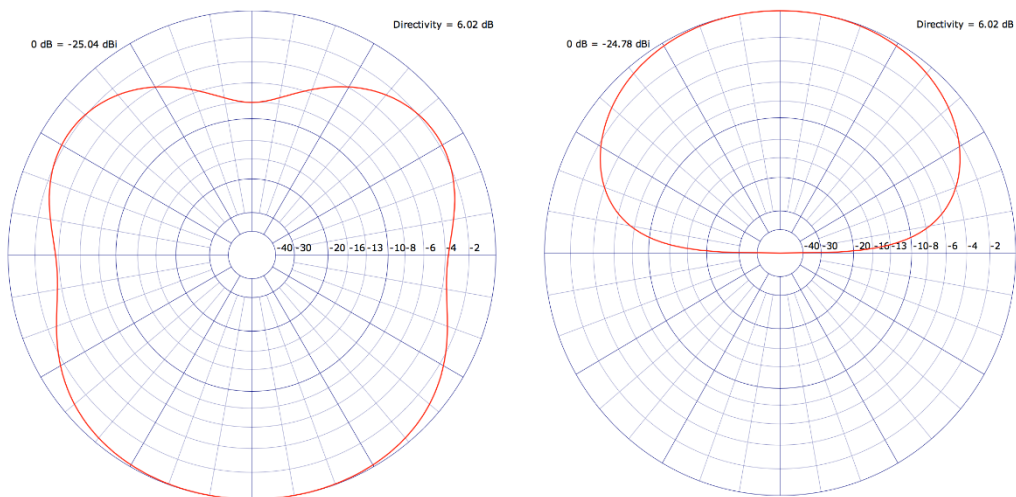


3D Radiation pattern produced by T1 array element perpendicular to Lancaster (T1-Cross) at 6.780 MHz

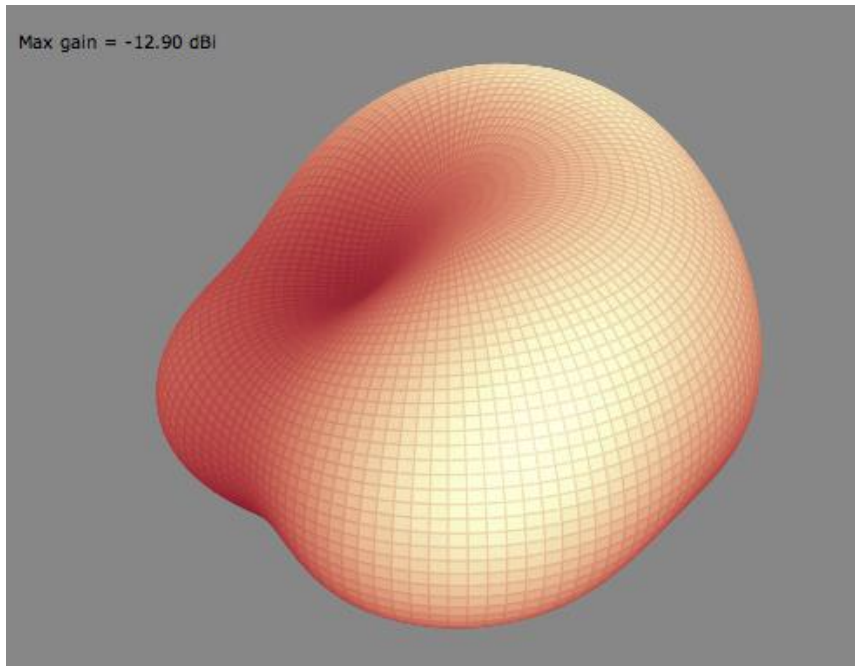
Appendix 2: T2 antenna array 2D and 3D radiation patterns



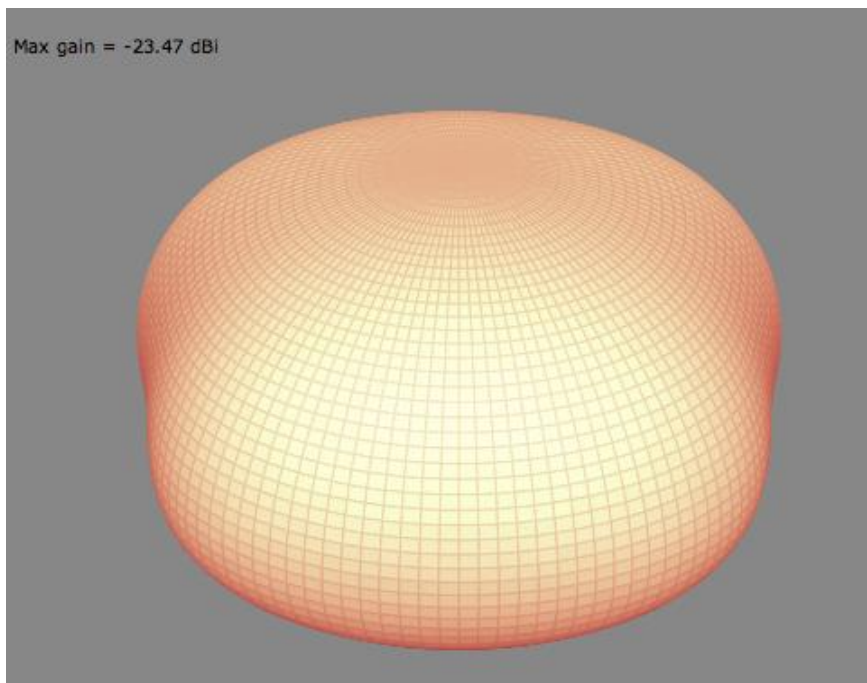
Radiation pattern produced by the array T2 element pointing to Lancaster (T2-Lan) at 6.780 MHz, Azimuth-plot (left) and Elevation-plot (right).



Radiation pattern produced by the array T2 array element perpendicular to Lancaster (T2-Cross) at 6.780 MHz, Azimuth-plot (left) and Elevation-plot (right).

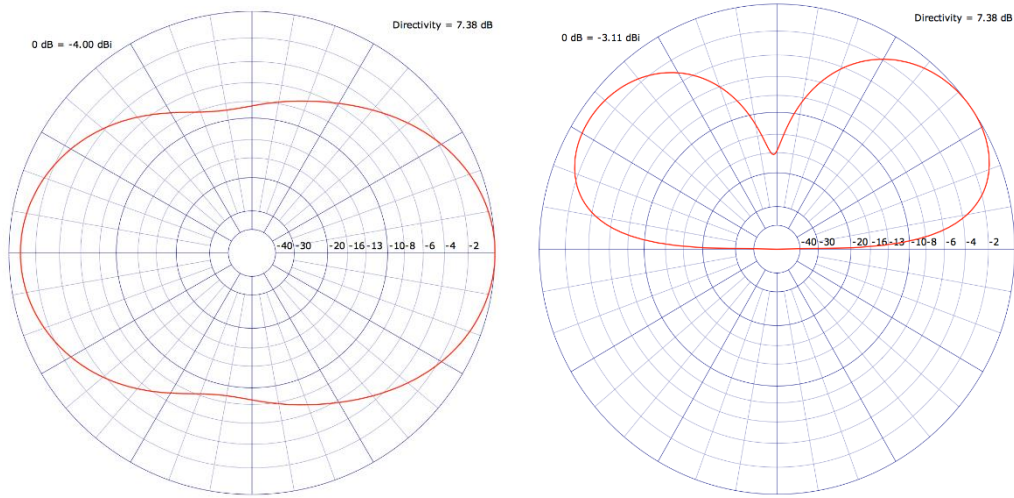


3D Radiation pattern produced by T2 array element pointing to Lancaster (T2-Lan) at 6.780 MHz

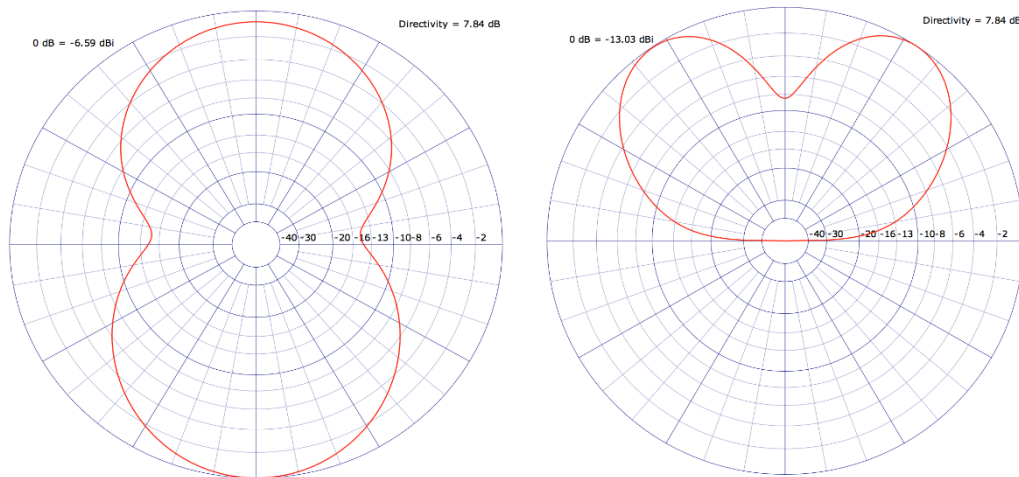


3D Radiation pattern produced by T2 array element perpendicular to Lancaster (T2-Cross) at 6.780 MHz

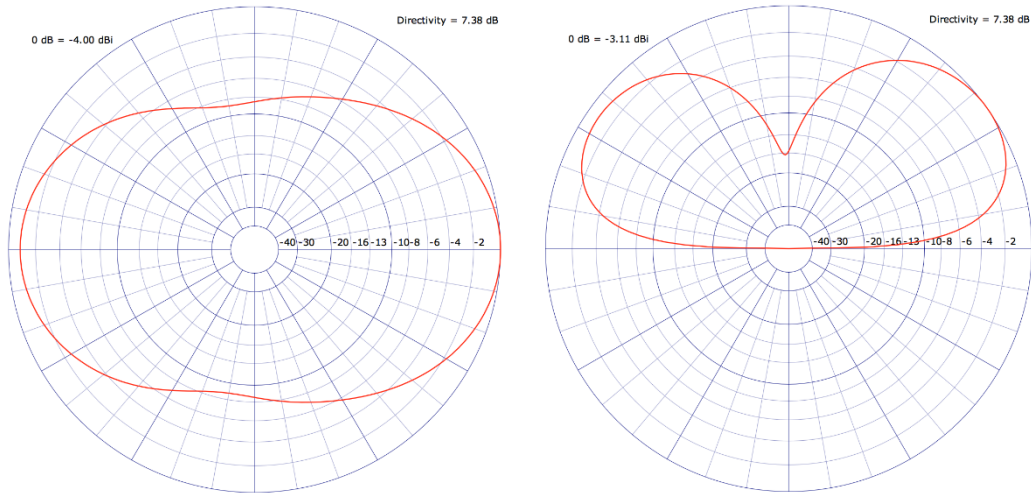
Appendix 3: Radiation patterns of ORG and Ex-ORG array (8.100 MHz)



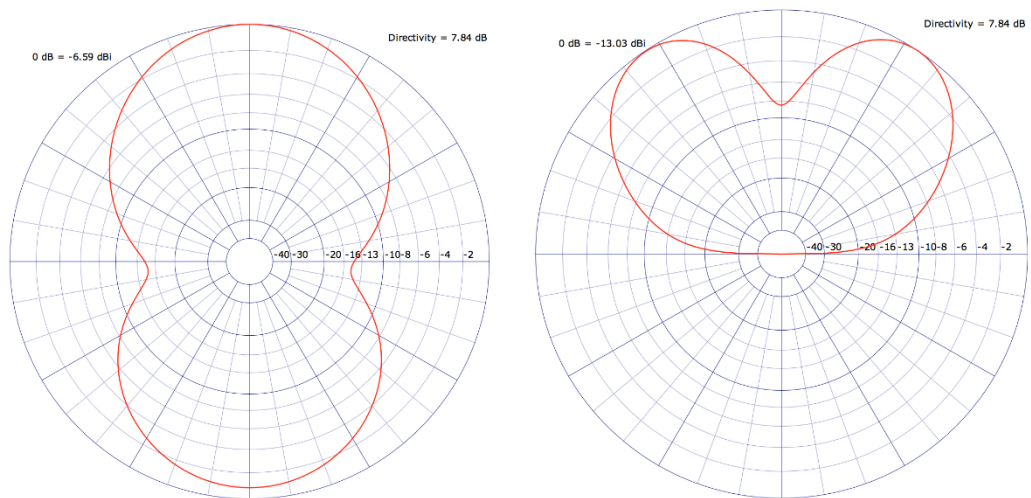
Radiation pattern produced by ORG array element pointing to Lancaster (ORG-Lan) at 8.100 MHz, Azimuth-plot (left) and Elevation-plot (right).



Radiation pattern produced by ORG array element perpendicular to Lancaster (ORG-Cross) at 8.100 MHz, Azimuth-plot (left) and Elevation-plot (right).

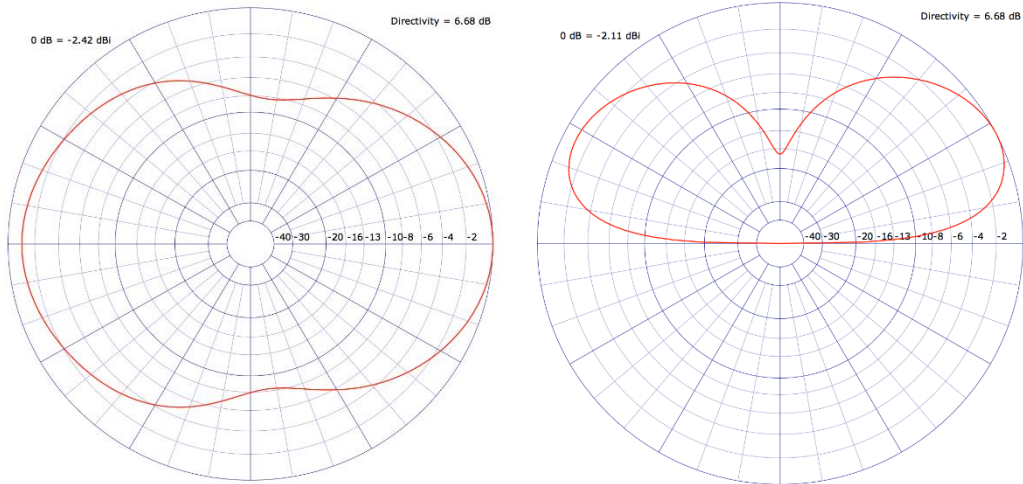


Radiation pattern produced by Ex-ORG array element pointing to Lancaster (ExORG-Lan) at 8.100 MHz, Azimuth-plot (left) and Elevation-plot (right).

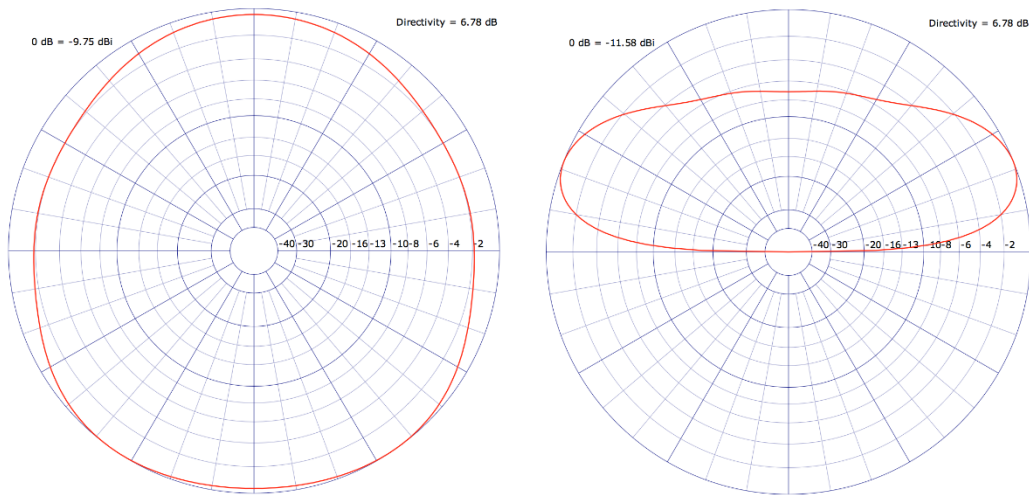


Radiation pattern produced by Ex-ORG array element perpendicular to Lancaster (ExORG-Cross) at 8.100 MHz, Azimuth-plot (left) and Elevation-plot (right).

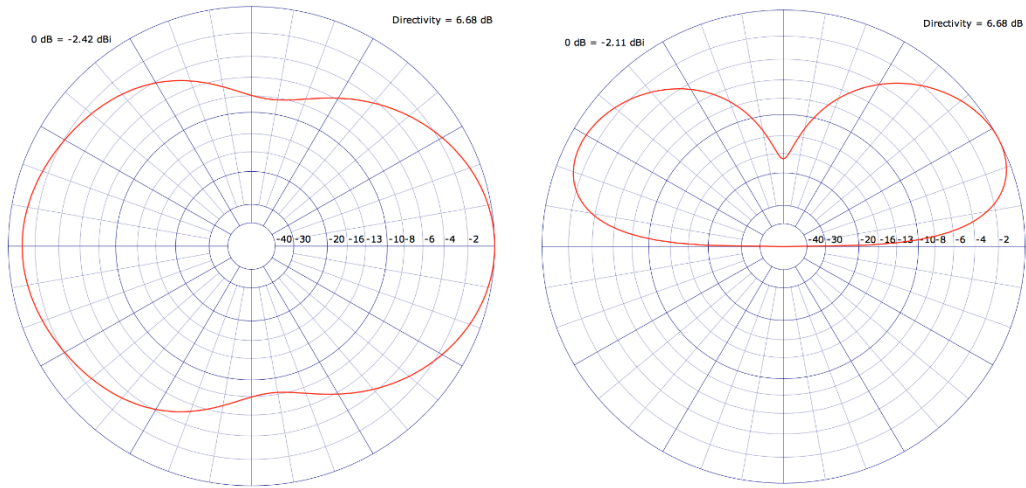
Appendix 4: Radiation patterns of T2 and Ex-T2 array (9.040 MHz)



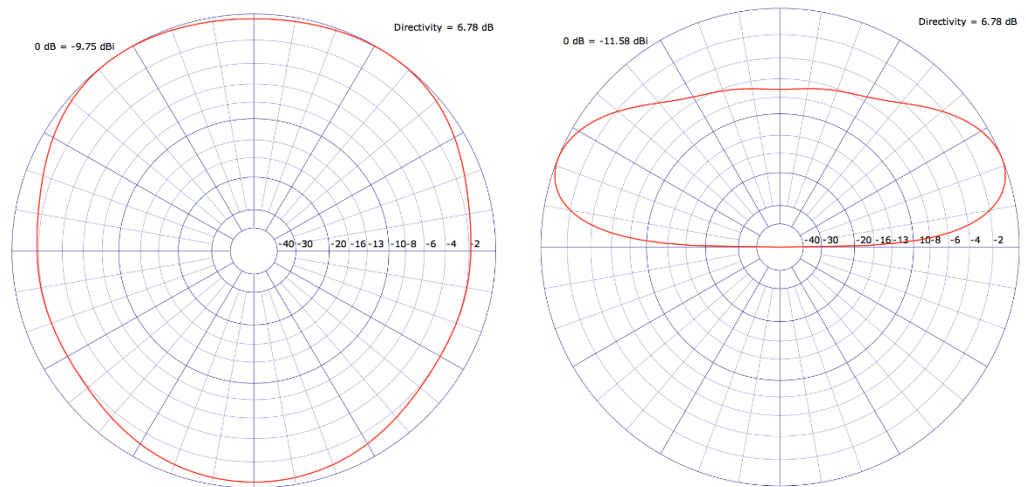
Radiation pattern produced by T2 array element pointing to Lancaster (T2-Lan) at 9.040 MHz, Azimuth-plot (left) and Elevation-plot (right).



Radiation pattern produced by T2 array element perpendicular to Lancaster (T2-Cross) at 9.040 MHz, Azimuth-plot (left) and Elevation-plot (right).



Radiation pattern produced by ExT2 array element pointing to Lancaster (ExT2-Lan) at 9.040 MHz, Azimuth-plot (left) and Elevation-plot (right).



Radiation pattern produced by ExT2 array element perpendicular to Lancaster (ExT2-Cross) at 9.040 MHz Azimuth-plot (left), Elevation-plot (right).